Doctoral Dissertation

Rationally Designed Fluorescent Probes for Visualizing Intracellular Mg^{2+} Dynamics

Yusuke Matsui

January 2018

Laboratory of Chemical Biology

Division of Advanced Science and Biotechnology

Graduate School of Engineering

Osaka University

Contents

List of Abbreviations

AM	Acetoxymethyl
APTRA	*o*-Aminophenol-*N*,*N*,*O*-triacetic acid
ATP	Adenosine triphosphate
ATeam	Adenosine 5'-triphosphate indicator based on epsilon subunit for analytical measurements
BAPTA	1,2-Bis-(2-aminophenoxy)ethane-*N*,*N*,*N'*,*N'*-tetraacetic acid
BF	Bright field
BM	Butyryloxymethyl
CHX	Cycloheximide
CNNM4	Ancient conserved domain protein/cyclin M4
COX8	Cytochrome *c* oxidase subunit VIII
d-PeT	Donor-excited photo-induced electron transfer
DCM	Dichloromethane
DCQ	2,8-Dicarboxyquinoline
DIEA	*N*,*N*-Diisopropylethylamine
DMEM	Dulbecco's modified Eagle medium
DMF	*N*,*N*-Dimethylformamide
DMSO	Dimethyl sulfoxide
DTT	Dithiothreitol
EEDQ	*N*-Ethoxycarbonyl-2-ethoxy-1,2-dihydroquinoline
ER	Endoplasmic reticulum
FBS	Fetal bovine serum
FRET	Fluorescence resonance energy transfer
GPC	Gel permeation chromatography
HBSS	Hanks' balanced salt solution
HEK	Human embryonic kidney
HEPES	4-(2-Hydroxyethyl)-1-piperazineethanesulfonic acid
HHBSS	HEPES-buffered Hanks' balanced salt solution
HOMO	Highest occupied molecular orbital
HPLC	High performance liquid chromatography
LUMO	Lowest unoccupied molecular orbital
MES	4-Morpholineethanesulfonate
MMgT	Membrane magnesium transporter
MagT1	Magnesium transporter 1

MgG	Magnesium Green
Mrs2	Mitochondrial RNA splicing 2
NLS	Nuclear localization signal
NMDG-Cl	*N*-methyl-$_D$-glucamine hydrochloride
NMR	Nuclear magnetic resonance
OG	Oregon green
PANX1	Pannexin 1
PM	Propionyloxymethyl
PRL	Phosphatases of regenerating liver
PeT	Photo-induced electron transfer
PyBOP	Benzotriazol-1-yl-oxytripyrrolidinophosphonium hexafluorophosphate
R-GECO	Red fluorescent genetically-encoded Ca^{2+} indicators for optical imaging
SD	Standard deviation
TEA	Triethylamine
TFA	Trifluoroacetic acid
TMR	Tetramethylrhodamine

General Introduction

Homeostasis and physiological roles of intracellular Mg^{2+}

Mg^{2+} is the most abundant divalent cation in cells. The overall intracellular Mg^{2+} concentration ranges between 17 and 20 mM.[1] However, since majority of Mg^{2+} binds to ATP, nucleotides, and phospholipids, intracellular free Mg^{2+} concentration ($[Mg^{2+}]_i$) is estimated to be between 0.5–1 mM, and it is tightly regulated by Mg^{2+} transporters and channels expressed on cell or organelle membranes, such as MMgT,[2] MagT1,[3] Mrs2,[4] and CNNM4 (Figure 1).[5] Mg^{2+} contributes to various physiological processes including the regulation of numerous enzyme activities, stabilization of nucleotides, and cell proliferation in living cells.[6–8] In addition, Mg^{2+} plays a role as a second messenger in T cells.[9] Abnormal Mg^{2+} homeostasis caused by dysfunction of Mg^{2+} channels/transporters induces several disorders such as tumor progression, immunodeficiency, and multiple sclerosis (Figure 1).[9-11] Thus, investigation of Mg^{2+} dynamics in the cytosol and organelles can contribute to the elucidation of novel biological processes and pathological mechanisms. However, despite Mg^{2+} being evidently important for regulating cellular functions, detailed intracellular Mg^{2+} dynamics remain unclear due to the lack of practical Mg^{2+} fluorescent probes.[12]

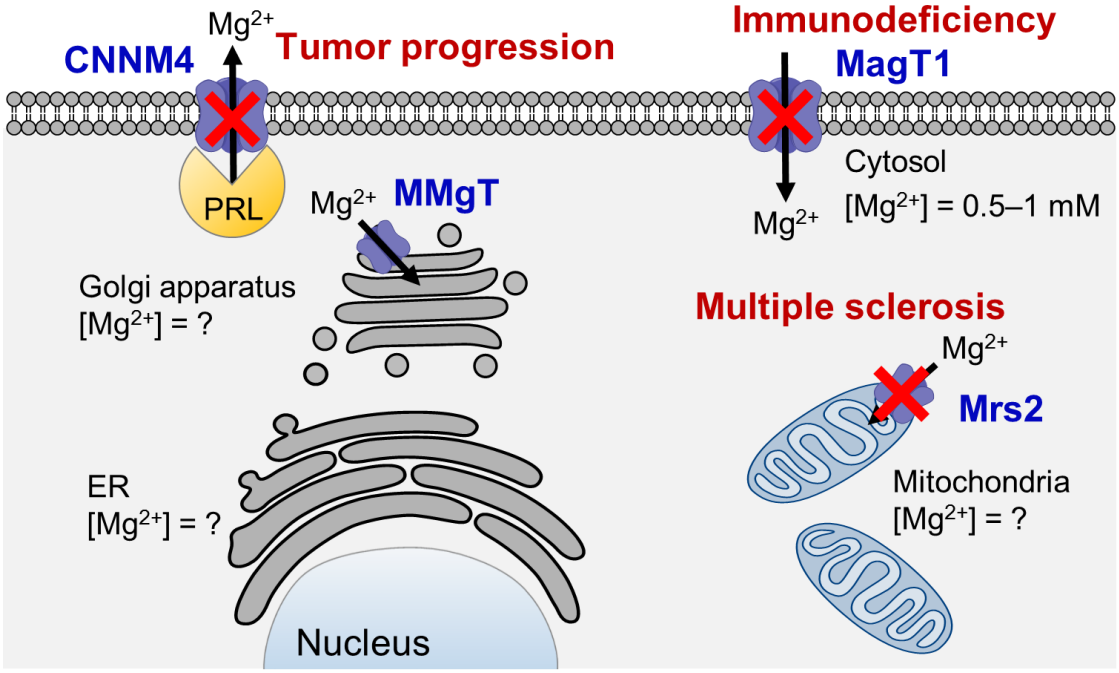

Figure 1. Mg^{2+}-channels/transporters and the associated diseases caused by its dysfunction.

Commercially available small molecule-based Mg^{2+} probes

Commercially available fluorescent Mg^{2+} probes, such as Magnesium Green, Mag-fluo-4 and Mag-fura-2, have often been used to visualize $[Mg^{2+}]_i$ changes (Figure 2).[5,9] In the structures of these probes, *o*-aminophenol-*N*,*N*,*O*-triacetic acid (APTRA) has been extensively adopted as a Mg^{2+} chelating moiety. APTRA was designed for binding to physiological free Mg^{2+} in cells (K_d (Mg^{2+}) = 1 mM (Magnesium Green), 4.7 mM (Mag-fluo-4) and 1.9 mM (Mag-fura-2)).[13] Magnesium Green and Mag-fluo-4 were designed so that the fluorescence intensity of its Mg^{2+}-unbound state is suppressed by photo-induced electron transfer (PeT),[14–16] and it emits strong fluorescence by binding to Mg^{2+} without shifts in excitation or emission wavelengths (Figure 3). On the other hand, the excitation maximum of Mag-fura-2 shifts 369 nm in Mg^{2+}-free medium to 330 nm at saturating Mg^{2+} concentration.[13] By calculating a ratio between the two fluorescence intensities at two different excitation wavelengths, Mga-fura-2 enables to quantify $[Mg^{2+}]_i$ without influence of unequal probe loading, photobleaching and leakage.

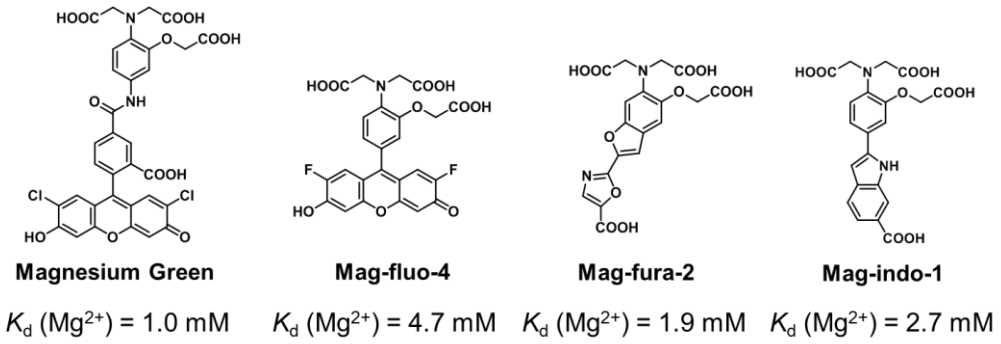

Figure 2. Chemical structures of commercially available Mg^{2+} probes.

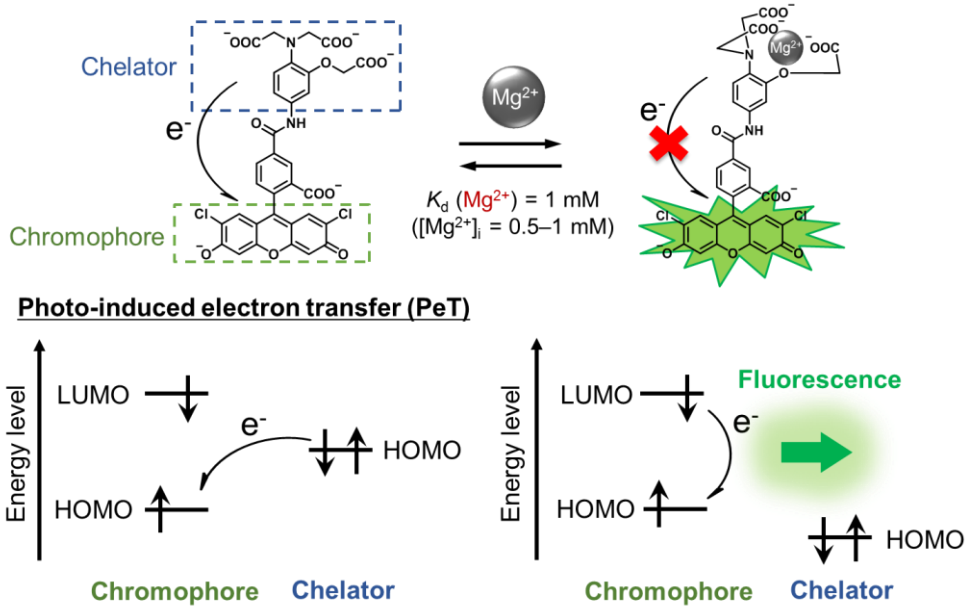

Figure 3. Mechanism of photo-induced electron transfer (PeT).

Limitations of small molecule-based Mg^{2+} probes

Although small molecule-based Mg^{2+} probes have been widely used for Mg^{2+} imaging, these Mg^{2+} probes are devoid of four important properties (Figure 4). Firstly, these probes tend to quickly diffuse over the entire cytoplasm. Secondly these probes leak out of the cells via anion transporters.[17,18] These unfavorable properties have made it impossible to image local Mg^{2+} concentration changes over long time periods, resulting in insufficient information regarding intracellular Mg^{2+} dynamics. Thirdly, APTRA-based Mg^{2+} probes show higher affinity toward Ca^{2+} (K_d (Ca^{2+}) = 6 μM (Magnesium Green), 22 μM (Mag-fluo-4) and 25 μM (Mag-fura-2)).[13] Since intracellular free Ca^{2+} concentration ($[Ca^{2+}]_i$) is approximately 100 nM in the resting state and increases 10- to 100-fold in response to various stimulation,[19] the moderate affinity of APTRA for Ca^{2+} limits the visualization of intracellular Mg^{2+} dynamics. In addition, these probes have often been utilized in Ca^{2+} imaging as low-affinity Ca^{2+} probes.[20,21] Therefore, APTRA-based Mg^{2+} probes are not ideal for the precise detection of $[Mg^{2+}]_i$ changes during physiological events associated with Ca^{2+} fluctuation. Furthermore, since some organelles such as mitochondria, endoplasmic reticulum (ER), and Golgi apparatus contain Ca^{2+} on the order of hundreds of μM,[22] it is impossible for these Mg^{2+} probes to exclusively detect Mg^{2+} concentration changes in the organelles listed. Several Mg^{2+} channels and transporters were recently identified on the membrane of these intracellular organelles.[1] These results strongly suggest that Mg^{2+} plays unknown yet important roles in these organelles. Finally, many fluorescent Mg^{2+} probes require the excitation with short wavelength under 500 nm.[12] This condition is likely to interfere with Mg^{2+} imaging due to phototoxicity to the cells and autofluorescence from natural intracellular molecules such as NADPH and flavins.[23] In particular, practical ratiometric Mg^{2+} probes that are excitable with visible light have not yet been developed.[12,24,25] Thus, these limitations have made it impossible to elucidate detailed intracellular Mg^{2+} dynamics with small molecule-based Mg^{2+} probes.

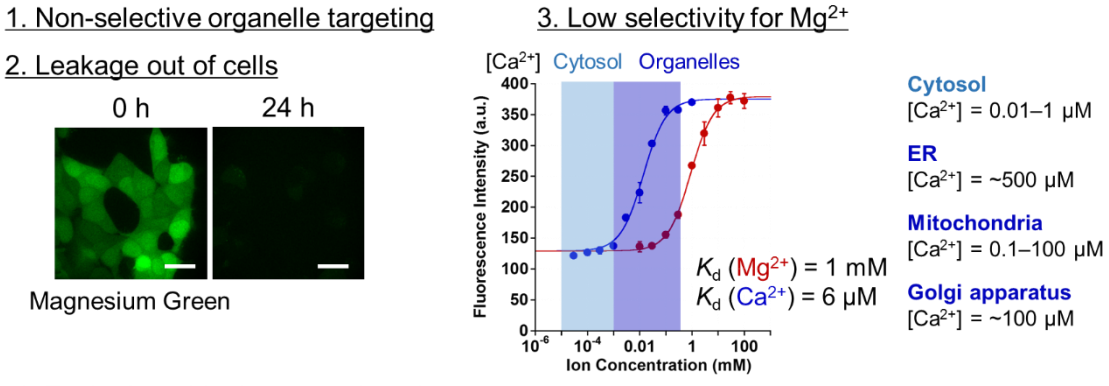

4. Excitation with short wavelength

	λ_{ex} (–Mg^{2+}) /nm	λ_{em} (–Mg^{2+}) /nm	λ_{ex} (+Mg^{2+}) /nm	λ_{em} (+Mg^{2+}) /nm
Magnesium Green	506	531	506	531
Mag-fluo-4	490	NA	493	517
Mag-fura-2	369	511	330	491
Mag-indo-1	349	480	330	417

Figure 4. Limitations of APTRA-based Mg^{2+} probes.

Genetically encoded fluorescent protein-based Mg^{2+} probes

Recently, genetically encoded fluorescent protein-based Mg^{2+} sensors, MagFRET[26] and MagIC,[27] have been reported (Figure 5). These probes were easily targeted to various intracellular compartments by adding the localization signal peptide, and are likely to be capable of long-term detection. However, the application of these probes is limited, probably due to their insensitivity in living cells[26] and/or the pH sensitivity under physiological conditions.[27] Therefore, ideal protein-based Mg^{2+} sensors have not yet been developed.

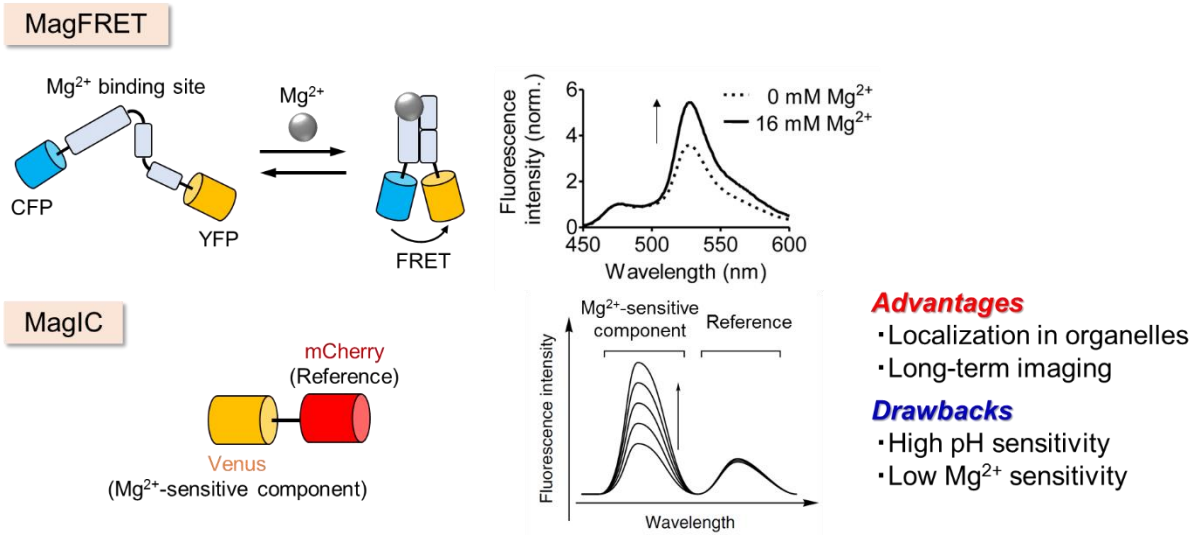

Figure 5. Genetically encoded fluorescent protein-based Mg^{2+} probes.

Outline of the research

Despite the importance of intracellular Mg^{2+} dynamics with respect to the field of biology and medicine, detailed mechanisms of $[Mg^{2+}]_i$ regulation are poorly understood due to the lack of convenient Mg^{2+} probes. To overcome the limitations of small molecule-based Mg^{2+} probes, the author designed and developed novel Mg^{2+} probes which enable subcellular targeting, long-term imaging, selective recognition of Mg^{2+}, and excitation with long wavelength over 500 nm.

In chapter 1, the author has developed a targetable fluorescent Mg^{2+} probe, MGH, which is covalently conjugated with HaloTag protein in various organelles, and demonstrated, for the first time, long-term live cell imaging of Mg^{2+}. The conjugation of MGH to HaloTag dramatically suppressed the extracellular leakage and retained the Mg^{2+} sensing ability of MGH for 24 h. To exploit this remarkable property, the Mg^{2+} probe was applied to the investigation of intracellular Mg^{2+} dynamics during apoptosis. Time-lapse imaging of Mg^{2+} dynamics in apoptotic cells revealed increase in the levels of $[Mg^{2+}]_i$ after apoptotic cell shrinkage. Furthermore, the author performed experiments to determine the cause of the increase in $[Mg^{2+}]_i$ levels by combining a genetically-encoded ATP sensor with the Mg^{2+} probe. The imaging analyses of $[Mg^{2+}]_i$ and ATP concentration strongly suggested that $[Mg^{2+}]_i$ increased as a result of the dissociation of Mg^{2+} from ATP with release of intracellular ATP through Pannexin 1 (PANX1) channels.

In chapter 2, the author identified a Mg^{2+}-selective chelator with a rigid tridentate structure, and developed the novel Mg^{2+}-selective fluorescent probes based on the identified chelator. These probes showed suitable affinity for Mg^{2+} to visualize changes in $[Mg^{2+}]_i$ and weak affinity for Ca^{2+}. Moreover, the rigid tridentate chelator distinguished free Mg^{2+} from Mg-ATP under physiological conditions. These advantageous properties enabled the prompt detection of changes in $[Mg^{2+}]_i$ without any fluorescence response to Ca^{2+} influx into living cells.

In chapter 3, the author developed a HaloTag-coupled Mg^{2+}-selective probe by combining labeling technology using protein-tag discussed in chapter 1 and the Mg^{2+} selective probe developed in chapter 2. This novel Mg^{2+} probe enabled selective detection of Mg^{2+} dynamics and localization in various organelles over a long time period.

In chapter 4, the author developed a red fluorescent turn-off Mg^{2+} probe with high Mg^{2+} selectivity. The quenching response to Mg^{2+} in combination with a green fluorescent turn-on Mg^{2+} probe enabled a ratiometric imaging of the changes in intracellular Mg^{2+} concentration. This ratiometric imaging system significantly enhanced the detection sensitivity of intracellular Mg^{2+} fluctuations in comparison with a conventional ratiometric Mg^{2+} sensing system.

List of conventional small molecule-based Mg^{2+} probes

Table 1. Optical properties of conventional Mg^{2+} probes

	$-Mg^{2+}$		$+Mg^{2+}$		K_d (Mg^{2+})	K_d (Ca^{2+})
	λ_{ex} /nm	λ_{em} /nm	λ_{ex} /nm	λ_{em} /nm	/mM	/μM
Magnesium Green[13]	506	531	506	531	1.0	6
Mag-fluo-4[13]	490	ND*	493	517	4.7	22
Mag-fura-2[13]	369	511	330	491	1.9	25
Mag-indo-1[13]	349	480	330	417	2.7	35
KMG-104[28]	502	523	502	523	2.1	7500
KMG-301[29]	565	589	565	589	4.5	ND*
KMG-104-AsH[30]	522	541	522	541	1.7	ND*
MagB2[31]	575	601	576	602	2.1	15
Mag-*mito*[32]	356	495	330	482	6.7	54
Mag-S-Tz[33]	404	595	358	565	3.1	41
DCHQ1[34]	363	505	363	505	0.044	ND*

*ND = not determined

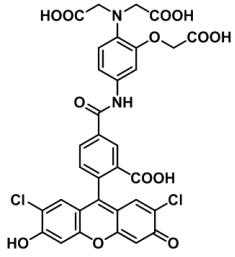

Magnesium Green

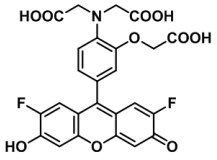

Mag-fluo-4

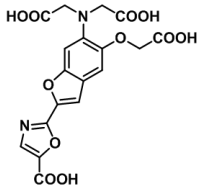

Mag-fura-2

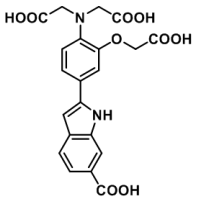

Mag-indo-1

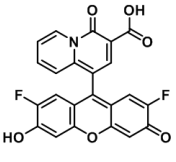

KMG-104

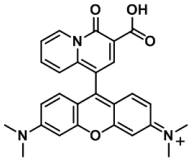

KMG-301

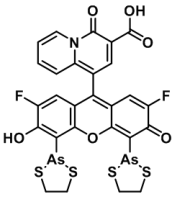

KMG-104-AsH

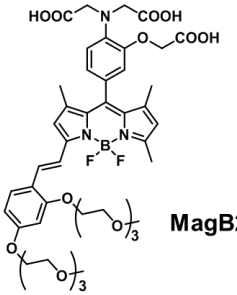

MagB2

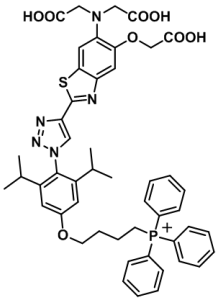

Mag-*mito*

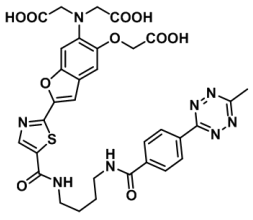

Mag-S-Tz

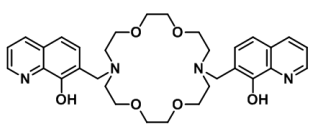

DCHQ1

References

1. A. M. Romani, *Arch. Biochem. Biophys*. **2011**, *512*, 1–23.
2. A. Goytain and G. A. Quamme, Am. J. Physiol. Cell. Physiol. **2008**, *294*, C495–502.
3. P. J. Kausalya, S. Amasheh, D. Gunzel, H. Wurps, D. Muller, M. Fromm, W. Hunziker, *J. Clin. Invest*. **2006**, *116*, 878–891.
4. M. A. Khan, A. D. Conigrave, *Br. J. Pharmacol*. **2010**, *159*, 1039–1050.
5. D. Yamazaki, Y. Funato, J. Miura, S. Sato, S. Toyosawa, K. Furutani, Y. Kurachi, Y. Omori, T. Furukawa, T. Tsuda, S. Kuwabata, S. Mizukami, K. Kikuchi and H. Miki, *PLoS Genet*. **2013**, *9*, e1003983.
6. A. Hartwig, *Mutat. Res*. **2001**, *475*, 113–121.
7. F. I. Wolf and V. Trapani, *Clinical Science* **2008**, *114*, 27–35.
8. A. M. Romani and A. Scarpa, *Arch. Biochem. Biophys*. **1992**, *298*, 1–12.
9. F.-Y. Li, B. Chaigne-Delalande, C. Kanellopoulou, J. C. Davis, H. F. Matthews, D. C. Douek, J. I. Cohen, G. Uzel, H. C. Su and M. J. Lenardo, *Nature* **2011**, *475*, 471–476.
10. J. H. F. de Baaij, J. G. J. Hoenderop and R. J. M. Bindels, *Physiol. Rev*. **2015**, *95*, 1–46.
11. Y. Funato, D. Yamazaki, S. Mizukami, L. Du, K. Kikuchi and H. Miki, *J. Clin. Invest*. **2014**, *124*, 5398–5410.
12. V. Trapani, G. Farruggia, C. Marraccini, S. Iotti, A. Cittadini and F. I. Wolf, *Analyst* **2010**, *135*, 1855–1866.
13. R. P. Haugland, Handbook of Fluorescent Probes and Research Products. 9th ed., Molecular Probes Inc., Eugene, Oregon, **2002**.
14. T. Ueno, Y. Urano, K. Setsukinai, H. Takakusa, H. Kojima, K. Kikuchi, K. Ohkubo, S. Fukuzumi and T. Nagano, *J. Am. Chem. Soc*. **2004**, *126*, 14079–14085.
15. T. Miura, Y. Urano, K. Tanaka, T. Nagano, K. Ohkubo and S. Fukuzumi, *J. Am. Chem. Soc.* **2003**, *125*, 8666–8671.
16. H. Kobayashi, M. Ogawa, R. Alford, P. L. Choyke and Y. Urano, *Chem. Rev*. **2010**, *110*, 2620–2640.
17. F. Di Virgilio, T. H. Steinberg, J. A. Swanson and S. C. Silverstein, *J. Immunol*. **1988**, *140*, 915–920.
18. M. Mitsui, A. Abe, M. Tajimi and H. Karaki, *Jpn. J. Pharmacol*. **1993**, *61*, 165–170.
19. D. E. Clapham, *Cell* **2007**, *131*, 1047–1058.
20. Y. Toiyo, A. Tanimura and Y. Matsumoto, *Biochem. Bioph. Res. Commun.* **1997**, *240*, 189–195.
21. G. R. Monteith, *Immunol. Cell Biol.* **2000**, *78*, 403–407.
22. J. Suzuki, K. Kanemaru and M. Iino, *Biophys. J*. **2016**, *111*, 1119–1131.

23. M. Monici, *Biotechnol. Annu. Rev*. **2005**, *11*, 227–256.
24. M. S. Afzal, J. P. Pitteloud and D. Buccella, *Chem. Commun*. **2014**, *50*, 11358–11361.
25. T. Shoda, K. Kikuchi, H. Kojima, Y. Urano, H. Komatsu, K. Suzuki and T. Nagano, *Analyst* **2003**, *128*, 719–723.
26. L. H. Lindenburg, J. L. Vinkenborg, J. Oortwijn, S. J. Aper and M. Merkx, *PLoS One* **2013**, *8*, e82009.
27. V. P. Koldenkova, T. Matsuda and T. Nagai, *J. Biomed. Opt*. **2015**, *20*, 101203.
28. H. Komatsu, N. Iwasawa, D. Citterio, Y. Suzuki, T. Kubota, K. Tokuno, Y. Kitamura, K. Oka and K. Suzuki, *J. Am. Chem. Soc*. **2004**, *126*, 16353–16360.
29. Y. Shindo, T. Fujii, H. Komatsu, D. Citterio, K. Hotta, K. Suzuki and K. Oka, *PLoS One* **2011**, *6*, e23684.
30. T. Fujii, Y. Shindo, K. Hotta, D. Citterio, S. Nishiyama, K. Suzuki and K. Oka, *J. Am. Chem. Soc*. **2014**, *136*, 2374–2381.
31. Q. Lin, J. J. Gruskos and D. Buccella, *Org. Biomol. Chem*. **2016**, *14*, 11381–11388.
32. G. Zhang, J. J. Gruskos, M. S. Afzal and D. Buccella, *Chem. Sci*. **2015**, *6*, 6841–6846.
33. J. J. Gruskos, G. Zhang and D. Buccella, *J. Am. Chem. Soc.* **2016**, *138*, 14639–14649.
34. G. Farruggia, S. Iotti, L. Prodi, M. Montalti, N. Zaccheroni, P. B. Savage, V. Trapani, P. Sale and F. I. Wolf, *J. Am. Chem. Soc*. **2006**, *128*, 344–350.

Chapter 1

Visualization of Long-term Mg^{2+} Dynamics in Apoptotic Cells with a Novel Targetable Fluorescent Probe

Chem. Sci. **2017**, *8*, 8255–8264.

Introduction

One phenomenon for which Mg^{2+} dynamics are unrevealed is apoptosis. Apoptosis is a programmed cell death process lasting for several hours to eliminate damaged cells. While Ca^{2+} plays very important roles to regulate the apoptotic process,[1] change in $[Mg^{2+}]_i$ has also been observed in apoptotic cells such as hepatocytes treated with glycodeoxycholate[2] and B lymphocytes treated with Fas ligand.[3] However, the intracellular Mg^{2+} dynamics during apoptosis have not been continuously visualized due to the leakage and quick diffusion of small-molecule based Mg^{2+} probes in cells.

To improve the temporal and spatial resolutions of Mg^{2+} imaging, small molecule-based Mg^{2+} probes with improved fluorescence properties and intracellular behaviors have been energetically developed. A chemical Mg^{2+} sensor functionalized with a lipophilic cationic alkylphosphonium group, Mag-*mito*, showed targetability to the mitochondria.[4] Mag-*mito* detected changes in free Mg^{2+} concentration in mitochondria by calculating the ratio of fluorescence signals obtained with two different excitation wavelengths. Mag-*mito* successfully detected an increase of free Mg^{2+} in mitochondria in the early stages of staurosporine-induced apoptosis. However, this probe diffused from the mitochondria to the cytosol after 40 min of the compound treatment because of the depolarization of the mitochondrial membrane during apoptosis.[4] It is likely that such noncovalent targetable probes diffuse away from the target site during long-term experiments. Furthermore, for monitoring Mg^{2+} concentration in various other organelles, novel fluorescent probes with different targeting moieties must be developed.

Therefore, a versatile method is to use a protein labeling system, which is a pair of a genetically encoded tag and its specific ligand. So far, several targetable fluorescent sensors have been developed on the basis of protein labeling systems such as SNAP-tag and HaloTag.[5–13] However, genetically encoded tag-based targeting of Mg^{2+} probes has rarely been reported. One example is KMG-104-AsH,[14] which was developed on the basis of highly selective Mg^{2+} sensors, KMG series.[15–17] KMG-104-AsH can be anchored to a tetracysteine peptide tag (TC-tag), which is genetically expressed in specific organelles,

enabling the detection of local Mg^{2+} concentration changes. However, long-term imaging of more than 4 h has not been carried out probably owing to the cellular toxicity of an additive (ethanedithiol) which is necessary to reduce nonspecific binding.[18] For the above mentioned reasons, novel targetable fluorescent probes for long-term monitoring of local Mg^{2+} dynamics in living cells have been pursued.

To address these issues, we developed a tag protein-conjugatable Mg^{2+} probe that can be localized in specific organelles for imaging local Mg^{2+} dynamics in living cells. By covalent anchoring of the Mg^{2+} probe to a tag protein expressed in various cellular compartments, intracellular diffusion and extracellular leakage of the Mg^{2+} probe were suppressed. This property enabled not only localization of the Mg^{2+} probe, but also long-term imaging of intracellular Mg^{2+} dynamics. This approach provided the first long-term imaging of $[Mg^{2+}]_i$ during apoptosis.

Design and synthesis of Mg^{2+} probe with HaloTag ligand

In order to visualize local Mg^{2+} dynamics in living cells for a long time, we designed and synthesized a new Mg^{2+} sensor, MGH, which covalently labels HaloTag (Figure 1-1). HaloTag is a modified haloalkane dehalogenase derived from *Rhodococcus*, and it quickly forms a covalent bond with specific ligands that include a chloroalkyl group.[19] HaloTag can be expressed as a fusion protein with a localization signal peptide in mammalian cells. Thus, MGH, which involves a HaloTag ligand, was expected to be localized in specific target organelles, since similar strategies have previously been exploited to localize various small-molecule metal ion sensors in specific organelles.[10–12]

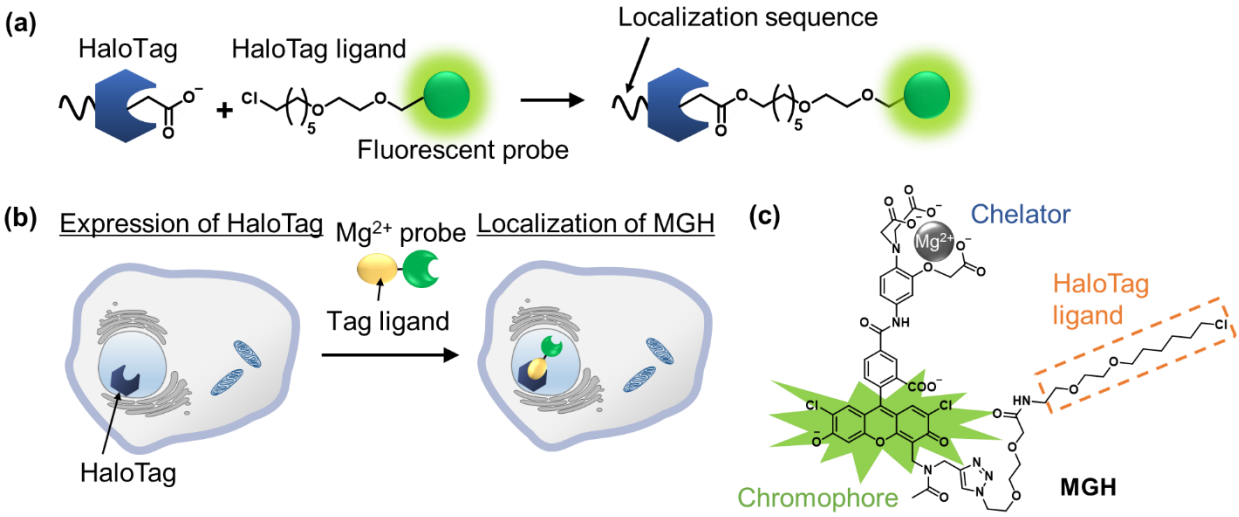

Figure 1-1. (a) Labeling of HaloTag with a HaloTag fluorescent ligand. (b) Localization of MGH in a specific organelle. (c) Overview of MGH, an Mg^{2+} probe modified with a HaloTag ligand.

Here, Magnesium Green was adopted for Mg^{2+} sensing due to its suitable dissociation constant for Mg^{2+} (K_d = 1 mM) to detect $[Mg^{2+}]_i$ changes.[20] The probe was designed so that the fluorescence intensity of its Mg^{2+}-unbound state is suppressed by photo-induced electron transfer (PeT),[21–23] and it emits strong fluorescence by binding to Mg^{2+}.

MGH is composed of three building blocks for synthesis: the Mg^{2+} chelator part, the fluorophore part, and the HaloTag ligand part. These components were individually synthesized, and were then conjugated to facilitate the synthetic process and optimization of each part. The Mg^{2+} chelator part (compound **4**) was synthesized from *o*-aminophenol by S_N2 reaction with chloroacetic acid, Fischer esterification, nitration, and alkaline hydrolysis (Scheme 1-1).[24] For improving the cell membrane permeability, compound **4** was then derivatized to tris-acetoxymethyl (AM) ester, which is quickly deprotected by endogenous intracellular esterases.[25] In the fluorophore part, an alkynyl moiety of compound **10** was introduced at the 4-position of the xanthene ring of 5-carboxyfluorescein by the Mannich reaction (Scheme 1-2).[26] Then, the secondary amine as well as the phenolic hydroxy groups, was modified with an acetyl group to avoid PeT from the free amino group to the fluorophore. Compound **15** was afforded by the amide condensation reaction of chelator moiety (compound **6**) and chromophore (compound **11**), and then it was conjugated with the HaloTag ligand (compound **14**) (Scheme 1-3) by Cu(I)-catalyzed azide-alkyne cycloaddition to produce MGH(AM) (Scheme 1-4). MGH(AM) was used for live cell imaging due to its sufficient cell membrane permeability. For the various in vitro spectral measurements, the deprotected probe MGH was synthesized by the alkaline hydrolysis of MGH(AM).

Scheme 1-1

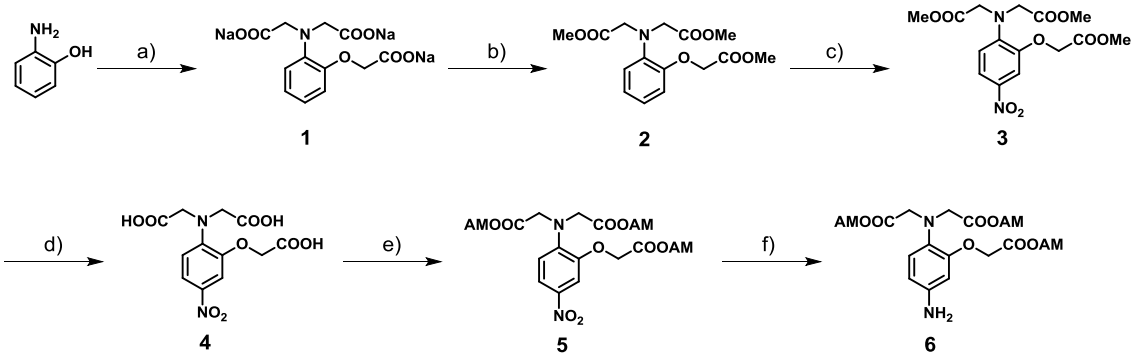

a) $ClCH_2COOH$, 2 M NaOH aq., 100 °C; b) H_2SO_4, MeOH, reflux, 31% (2 steps); c) HNO_3, AcOH, 0 °C, 77%; d) 2 M NaOH aq., MeOH/H_2O (3:1), quant.; e) bromomethyl acetate, TEA, DMF, r.t., 43% (2 steps); f) Pd/C, H_2, MeOH, r.t., quant.

Scheme 1-2

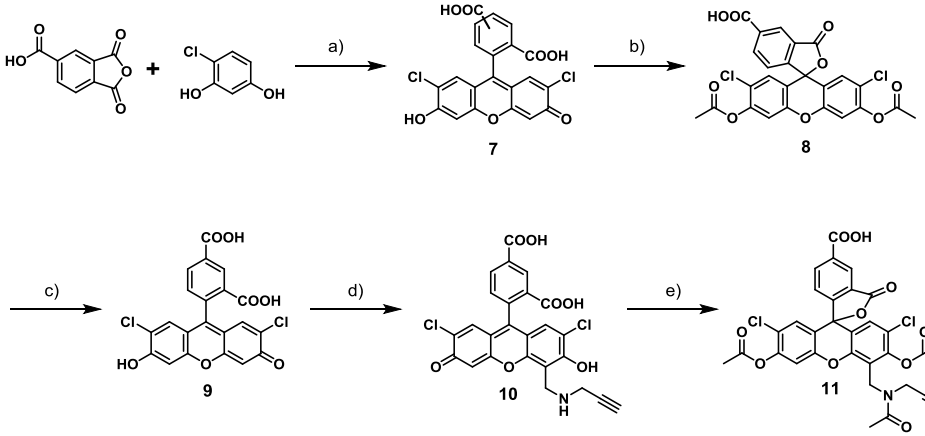

a) $MeSO_3H$, 90 °C; b) acetic anhydride, pyridine, reflux, 49% (2 steps); c) 2 M NaOH aq., $MeOH/H_2O$ (3:1), r.t., quant.; d) propargylamine, formaldehyde, CH_3CN/H_2O (1:1), 80 °C; e) acetic anhydride, pyridine, reflux, 30% (2 steps).

Scheme 1-3

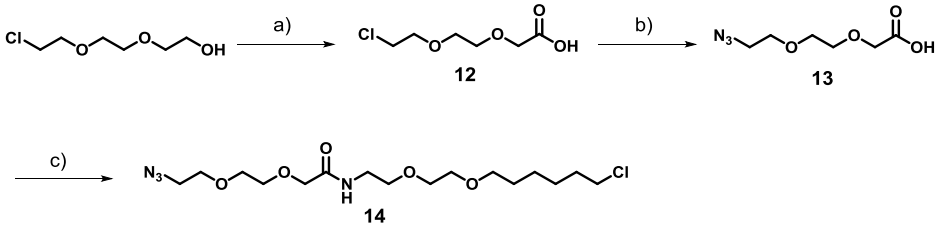

a) Cr_3O, 1.5 M H_2SO_4, acetone, 0 °C→r.t., 42%; b) NaN_3, H_2O, 80 °C, 68%; c) HaloTag Amine (O2) ligand, PyBOP, TEA, DMF, r.t., 32%.

Scheme 1-4

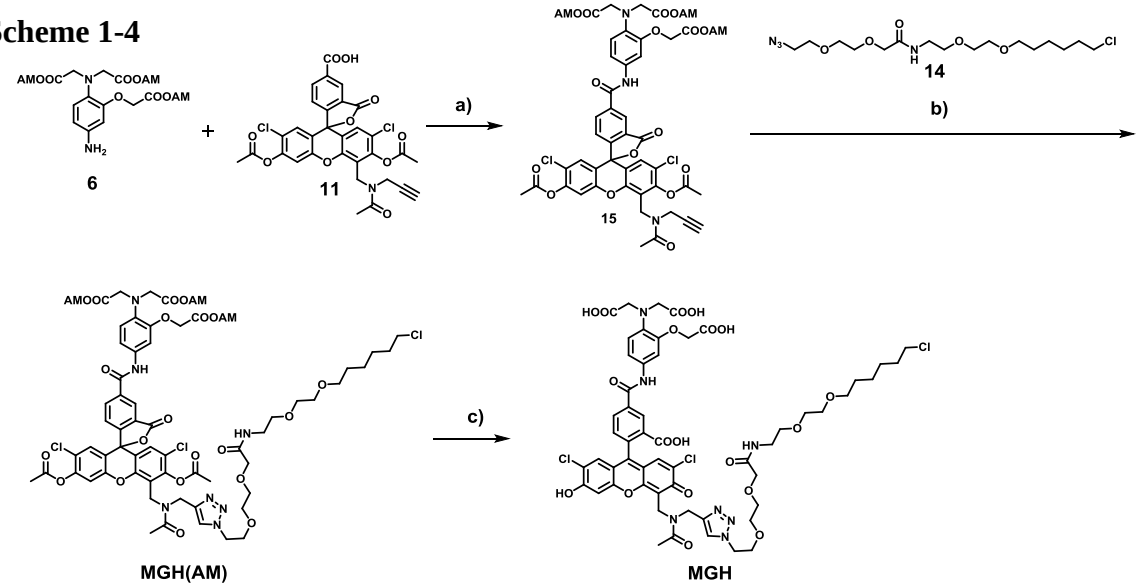

a) EEDQ, DCM, r.t., 29%; b) $CuSO_4$, sodium ascorbate, DMF/H_2O (4:1), r.t., 33%; c) 2 M NaOH aq., $MeOH/H_2O$ (3:1), r.t., quant.

Spectroscopic properties of MGH and HaloTag-MGH

The absorption and emission spectra of MGH were measured in 100 mM HEPES buffer (pH 7.4) containing 115 mM KCl and 20 mM NaCl. Although the absorption spectra of MGH did not change significantly with 100 mM Mg^{2+} (Figure 1-2a), the fluorescence intensity of MGH considerably increased as the Mg^{2+} concentration was increased (Φ_{free} = 0.19, Φ_{bound} = 0.56, Figure 1-2b and Table 1-1). From the fluorescence intensity change, the dissociation constant of MGH for Mg^{2+} was calculated to be 1.3 mM (Figure 1-2c), which is a suitable value for imaging $[Mg^{2+}]_i$ changes. The metal ion selectivity of MGH, shown in Figure 1-2d, was similar to that of other APTRA-based fluorescent probes.[27] For live-cell Mg^{2+} imaging, the ability of the probe to discriminate changes in intracellular Ca^{2+} concentration ($[Ca^{2+}]_i$) is quite important. MGH bound to Ca^{2+} more strongly (K_d (Ca^{2+}) = 12 μM) than to Mg^{2+} (Figure 1-2c), although this had already been predicted at the stage of the probe design. Since $[Ca^{2+}]_i$ is roughly 100 nM and rises 10- to 100-fold during various cellular events,[28] simultaneous monitoring of $[Ca^{2+}]_i$ with a Ca^{2+}-specific probe is necessary to correctly evaluate intracellular Mg^{2+} dynamics with MGH. In addition, the pH sensitivity of live-cell imaging probes is another important factor for practical use. Concerning the pH effect, MGH scarcely showed a fluorescence intensity change in a physiological pH range (pH 7–8) (Figure 1-2e). These spectroscopic properties of MGH mostly corresponded with Magnesium Green, indicating that attachment of HaloTag ligand scarcely affected the metal ion-detecting properties of the Mg^{2+} sensor (Figure 1-3 and Table 1-1).

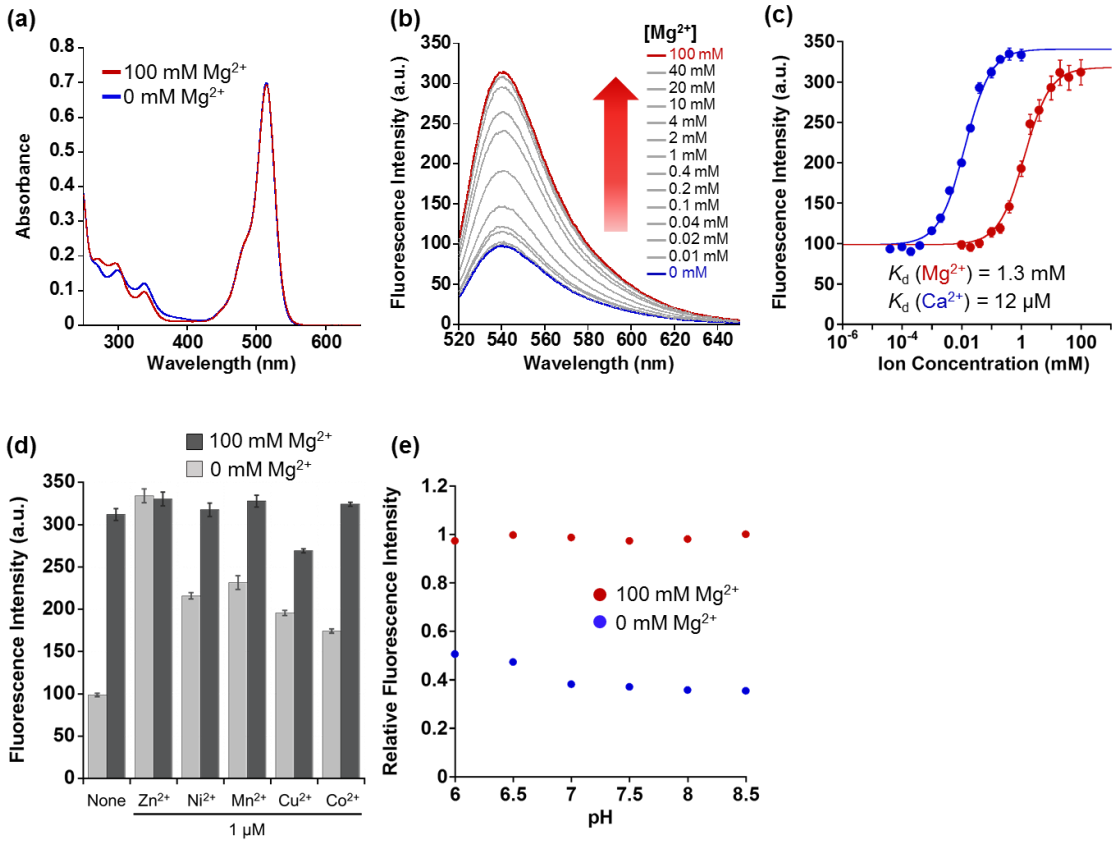

Figure 1-2. (a) Absorption spectra of 10 μM MGH in the presence or absence of 100 mM Mg^{2+} (100 mM HEPES buffer, 115 mM KCl, 20 mM NaCl, pH 7.4, 37 °C). (b) Emission spectra of 1 μM MGH in the presence of Mg^{2+} (100 mM HEPES, 115 mM KCl, 20 mM NaCl, pH 7.4, 37 °C). [Mg^{2+}] = 0, 0.01, 0.02, 0.04, 0.1, 0.2, 0.4, 1, 2, 4, 10, 20, 40, 100 mM. λ_{ex} = 515 nm. (c) Mg^{2+}- and Ca^{2+}-titration curves of MGH emission at 538 nm (λ_{ex} = 515 nm). [Ca^{2+}] = 0, 0.04, 0.1, 0.2, 0.4, 1, 2, 4, 10, 20, 40, 100, 200, 400, 1000 μM. The error bars denote SD (n = 3). (d) Metal ion selectivity for 1 μM MGH in the presence and absence of 100 mM Mg^{2+} (100 mM HEPES buffer, 115 mM KCl, 20 mM NaCl, pH 7.4, 37 °C). Zn^{2+}, Ni^{2+}, Mn^{2+}, Cu^{2+} or Co^{2+} were added to a final concentration of 1 μM. (e) Effect of the pH on the fluorescence intensity of MGH in the pH range of 6.0–6.5 (in 100 mM MES buffer, 115 mM KCl, 20 mM NaCl) and 7.0–8.5 (in 100 mM HEPES buffer, 115 mM KCl, 20 mM NaCl), with or without 100 mM Mg^{2+}. The error bars denote SD (n = 3).

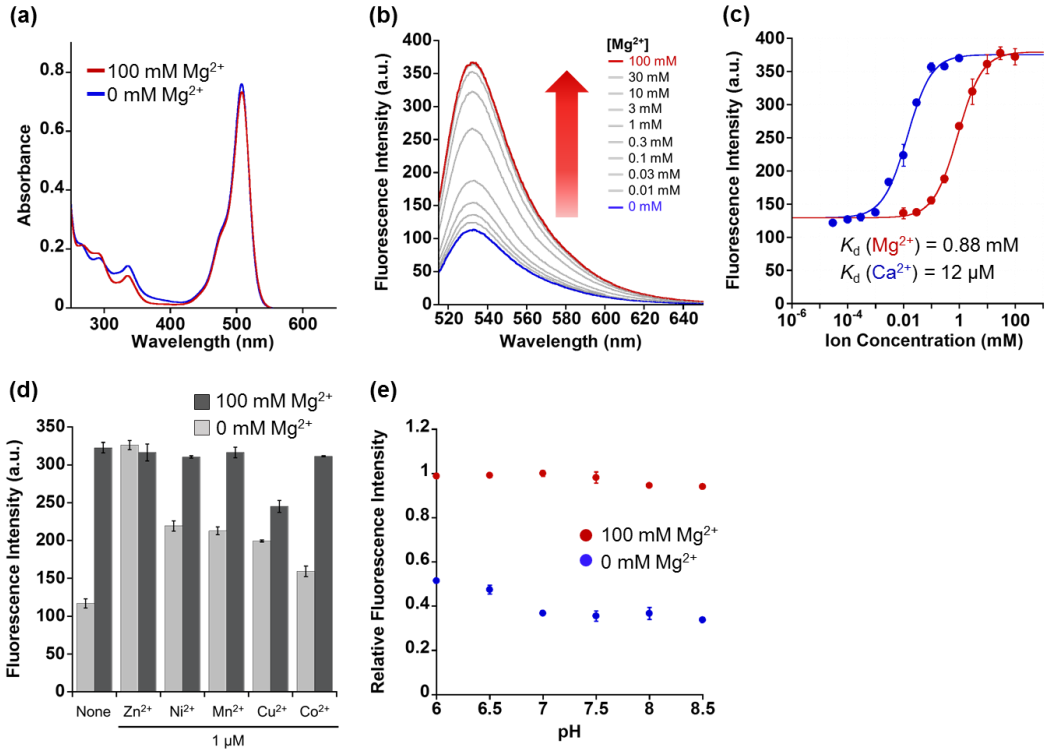

Figure 1-3. (a) Absorption spectra of 10 μM Magnesium Green in the presence or absence of 100 mM Mg^{2+} (100 mM HEPES buffer, 115 mM KCl, 20 mM NaCl, pH 7.4, 37 °C). (b) Emission spectra of 1 μM Magnesium Green in the presence of Mg^{2+} (100 mM HEPES, 115 mM KCl, 20 mM NaCl, pH 7.4, 37 °C). [Mg^{2+}] = 0, 0.01, 0.03, 0.1, 0.3, 1, 3, 10, 30, 100 mM. λ_{ex} = 509 nm. (c) Mg^{2+}- and Ca^{2+}-titration curves of Magnesium Green emission at 534 nm (λ_{ex} = 509 nm). [Ca^{2+}] = 0, 0.03, 0.1, 0.3, 1, 3, 10, 30, 100, 300, 1000 μM. (d) Metal ion selectivity for 1 μM Magnesium Green in the presence and absence of 100 mM Mg^{2+} (100 mM HEPES buffer, 115 mM KCl, 20 mM NaCl, pH 7.4, 37 °C). Zn^{2+}, Ni^{2+}, Mn^{2+}, Cu^{2+} or Co^{2+} were added to a final concentration of 1 μM. (e) Effect of the pH on the fluorescence intensity of Magnesium Green in the pH range of 6.0–6.5 (in 100 mM MES buffer, 115 mM KCl, 20 mM NaCl) and 7.0–8.5 (in 100 mM HEPES buffer, 115 mM KCl, 20 mM NaCl), with or without 100 mM Mg^{2+}. The error bars denote SD (n = 3).

Table 1-1. Spectroscopic and coordination properties of MGH, HaloTag-MGH and Magnesium Green[a]

	λ_{abs}/nm	λ_{em}/nm	ε/cm^{-1} M^{-1}	Φ_{free} [b] (Φ_{bound})	K_d (Mg^{2+})/mM	K_d (Ca^{2+})/μM
MGH	515	538	77,000	0.19 (0.56)	1.3	12
HaloTag-MGH	517	540	78,000	0.21 (0.61)	0.67	7.5
Magnesium Green	509	534	77,000	0.20 (0.56)	0.88	12

[a] Measured at 37 ºC in 100 mM HEPES buffer, 115 mM KCl, 20 mM NaCl, pH 7.4.

[b] Relative fluorescence quantum yield determined by using fluorescein (Φ = 0.85 in 0.1 M NaOH aq.) as a standard. Φ_{free} and Φ_{bound} denote the relative fluorescent quantum yield in the absence and presence of 100 mM Mg^{2+}, respectively.

It is likely that spectroscopic properties of fluorescent probes are affected by environmental changes such as binding on the protein surface. Hence, the author measured spectroscopic properties of MGH after incubation with purified HaloTag protein for 1 h at 37 °C. SDS-PAGE analysis showed almost all MGH covalently bound to HaloTag (Figure 1-4). Overall, the fluorescence properties of HaloTag-MGH were similar to those of MGH and Magnesium Green (Figure 1-5 and Table 1-1). The author infers that, in response to Mg^{2+}, almost the same dynamic range of HaloTag-MGH as that of free MGH was derived from the hydrophilic spacer between the Mg^{2+} sensor part and the HaloTag ligand part, and the hydrophilic spacer prevented the interaction between the chromophore and the protein surface of the HaloTag.[12] Although the K_d values of HaloTag-MGH for Mg^{2+} and Ca^{2+} were enhanced by approximately 2-fold, the affinity of HaloTag-MGH to Mg^{2+} was still appropriate for visualizing intracellular Mg^{2+} dynamics.

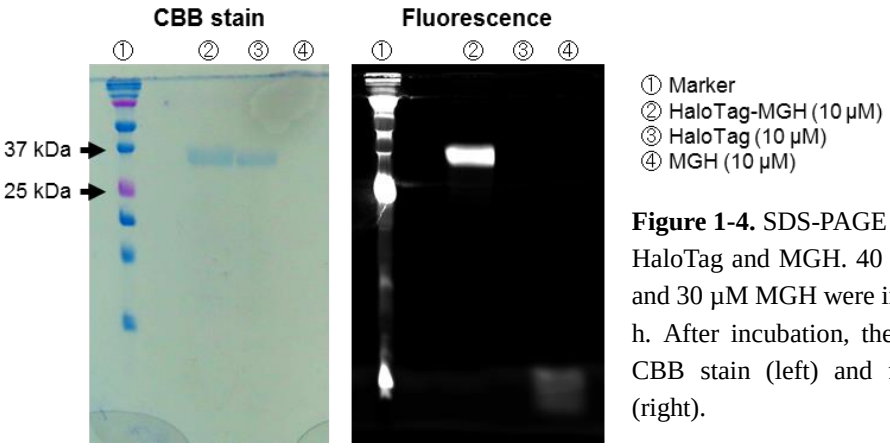

Figure 1-4. SDS-PAGE analysis of complex of HaloTag and MGH. 40 μM HaloTag (33 kDa) and 30 μM MGH were incubated at 37 °C for 1 h. After incubation, the gel was analyzed by CBB stain (left) and fluorescence detection (right).

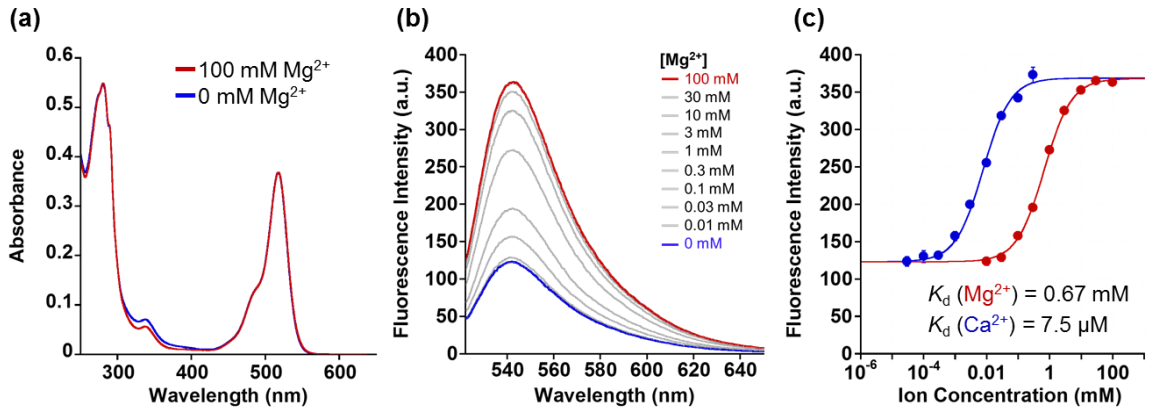

Figure 1-5. (a) Absorption spectra of 5 μM HaloTag-MGH in the presence or absence of 100 mM Mg^{2+} (100 mM HEPES buffer, 115 mM KCl, 20 mM NaCl, pH 7.4, 37 °C). (b) Emission spectra of 1 μM HaloTag-MGH complex in the presence of Mg^{2+} (100 mM HEPES, 115 mM KCl, 20 mM NaCl, pH 7.4, 37 °C). [Mg^{2+}] = 0, 0.01, 0.03, 0.1, 0.3, 1, 3, 10, 30, 100 mM. λ_{ex} = 517 nm. (c) Mg^{2+}- and Ca^{2+}-titration curves of HaloTag-MGH emission at 540 nm (λ_{ex} = 517 nm). [Ca^{2+}] = 0, 0.03, 0.1, 0.3, 1, 3, 10, 30, 100, 300, 1000 μM. The error bars denote SD (n = 3).

Subcellular targeting of MGH and long-term imaging of Mg^{2+} in living cells

Here, the author attempted to confirm the subcellular targeting of MGH to a variety of organelles. HEK293T cells were transfected with a plasmid encoding Halo-NLS, Lyn_{11}-Halo, or HaloTag. NLS is a nuclear localization signal peptide[29] and Lyn_{11} is a Lyn *N*-terminal sequence (GCIKSKGKDSA), which is used to target proteins to the inner leaflet of cell membrane.[30,31] The transfected and non-transfected cells were incubated with 3 μM MGH(AM) for 1 h at 37 °C and were observed using a confocal spinning disk fluorescence microscope. In the case of non-transfected cells, weak fluorescence was observed from the entire cells (Figure 1-6a). On the other hand, in transfected cells, strong fluorescence was observed from the target domains, such as nuclei, cell membrane inner leaflet, or intracellular region without nonspecific fluorescence signals (Figure 1-6a).

Subsequently, MGH(AM) was added to HEK293T cells expressing HaloTag in the endoplasmic reticulum (ER) or the mitochondrial matrix. Since these organelles are covered by lipid bilayer membrane, it was unclear whether fluorescent probes modified with AM esters could penetrate the second lipid bilayer membrane prior to the enzymatic hydrolysis of the AM esters by intracellular esterases. For expressing HaloTag in ER, ER signal peptide and retention signal sequences (SEKDEL) were fused with HaloTag (Halo-ER). For mitochondrial matrix targeting, HaloTag was fused with the first 36 amino acids of subunit VIII of cytochrome c oxidase (COX8) in tandem to enhance the specificity of mitochondrial localization (2xCOX8-Halo).[32] When the cells expressing Halo-ER or 2xCOX8-Halo were incubated with MGH(AM) for 1 h, the fluorescence of MGH was observed from the ER and mitochondria, respectively. The intended targeting of MGH to the ER and mitochondria was confirmed by the colocalization with the fluorescent signals of ER-Tracker Red and MitoTracker DeepRed, respectively (Figure 1-6b). The results indicate that MGH(AM) diffused very quickly in living cells and accumulated inside of organelles surrounded by lipid bilayers, such as ER and the mitochondrial matrix, before enzymatic hydrolysis of the AM esters. However, it is likely that MGH mainly detects Ca^{2+} in the ER because the ER contains high concentrations of Ca^{2+} (hundreds of μM). Therefore, Mg^{2+}-selective probes are necessary for the correct evaluation of changes in Mg^{2+} concentrations in the ER.

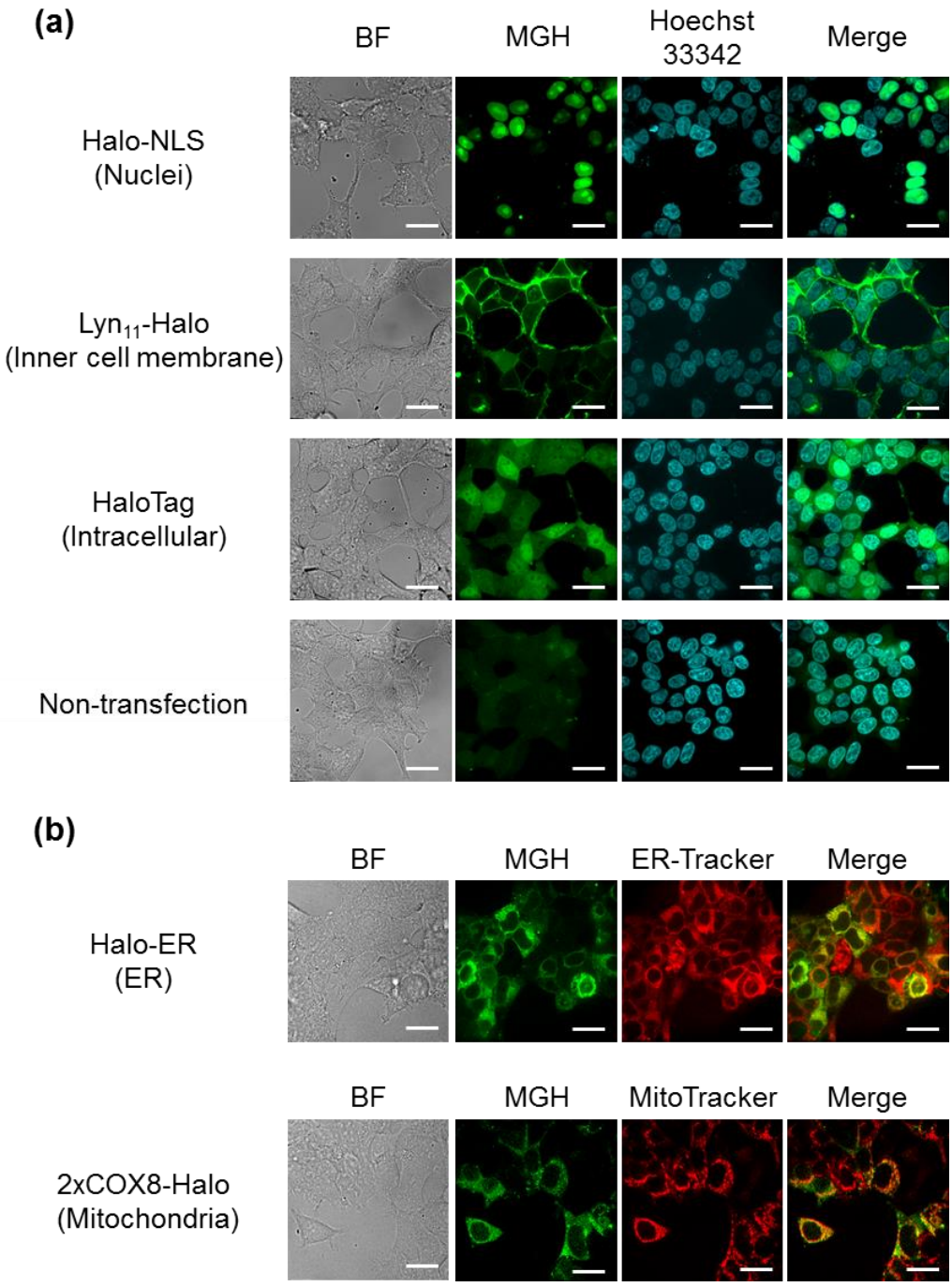

Figure 1-6. Subcellular localization of MGH in living cells. (a) Confocal fluorescence microscopic images of MGH localization in HEK293T cells transfected with a plasmid encoding Halo-NLS (nuclei), Lyn_{11}-Halo (inner leaflet of cell membrane) or HaloTag (intracellular region). Labeling reactions of fusion protein of Halo-NLS, Lyn_{11}-Halo or HaloTag in HEK293T cells with 3 μM MGH(AM) and staining with 200 ng/mL Hoechst 33342 were performed for 1 h at 37 °C. (b) Confocal fluorescence microscopic images of MGH localization in ER or mitochondria matrix, which are surrounded by lipid bilayer membrane. HEK293T cells transiently expressing Halo-ER or 2xCOX8-Halo were incubated with 3 μM MGH(AM) and either 200 nM ER-Tracker Red or 200 nM MitoTracker DeepRed for 1 h at 37 °C. Scale bar: 20 μm.

Next, long-term Mg^{2+} imaging in living cells was attempted by using the nucleus-localized MGH. Commercially available small-molecule Mg^{2+} probes, such as Magnesium Green, are not suitable for long-term imaging owing to the extracellular leakage by anion transporters.[33,34] The author also confirmed that the fluorescence of Magnesium Green gradually decreased in a time-dependent manner, and completely disappeared after 24 h (Figures 1-7b and c). In contrast, the fluorescence of nucleus-localized MGH was continuously detected for 24 h (Figures 1-7a and c). The fluorescent signals of Hoechst 33342, which is a membrane-permeable cationic dye, gradually decreased, probably because of diffusion of the dye (Figures 1-7a and c). These results indicated that MGH enables imaging of Mg^{2+} dynamics for more than 1 day.

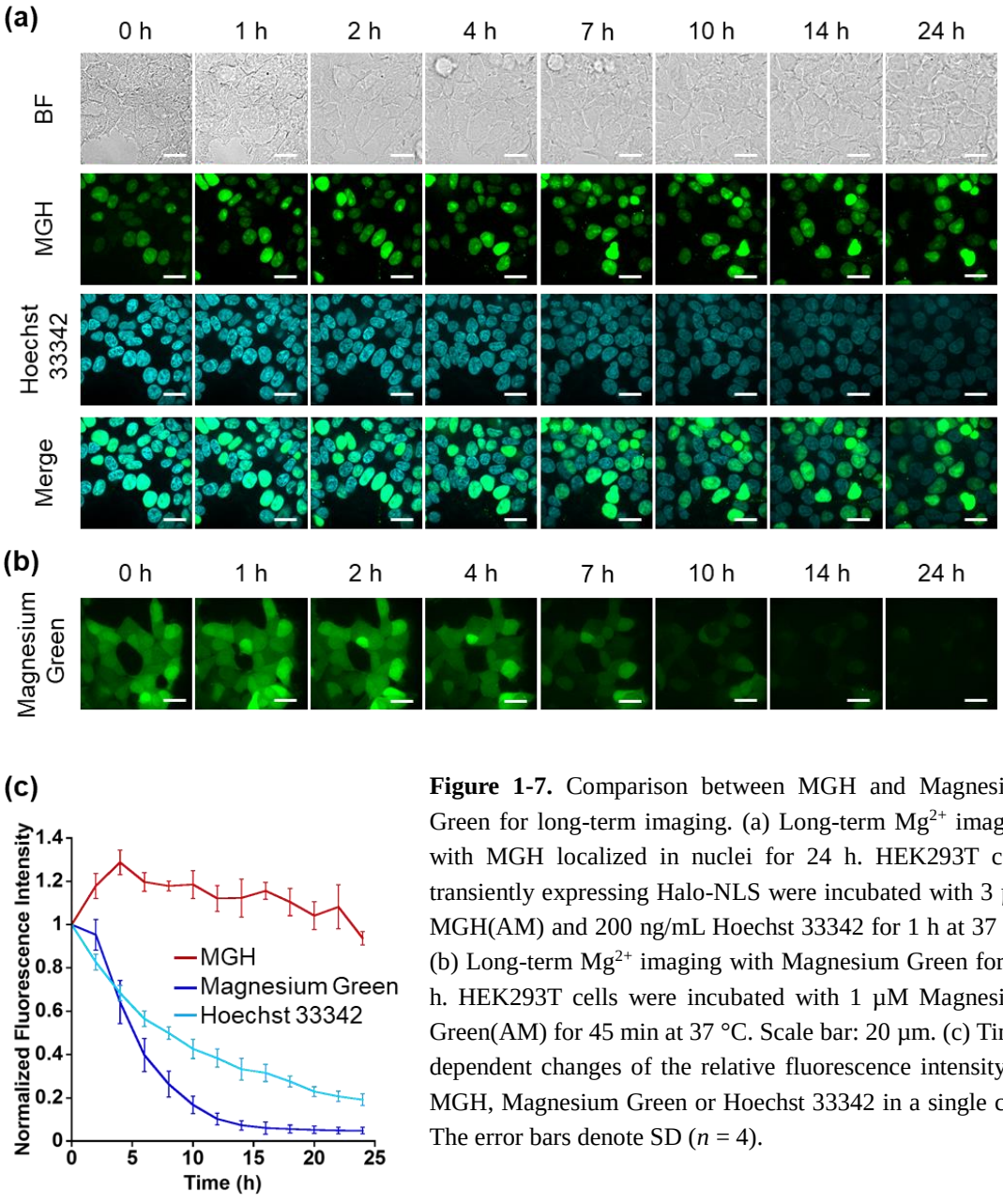

Figure 1-7. Comparison between MGH and Magnesium Green for long-term imaging. (a) Long-term Mg^{2+} imaging with MGH localized in nuclei for 24 h. HEK293T cells transiently expressing Halo-NLS were incubated with 3 μM MGH(AM) and 200 ng/mL Hoechst 33342 for 1 h at 37 °C. (b) Long-term Mg^{2+} imaging with Magnesium Green for 24 h. HEK293T cells were incubated with 1 μM Magnesium Green(AM) for 45 min at 37 °C. Scale bar: 20 μm. (c) Time-dependent changes of the relative fluorescence intensity of MGH, Magnesium Green or Hoechst 33342 in a single cell. The error bars denote SD (n = 4).

Detection of Mg^{2+} extrusion through CNNM4

To examine the response of nucleus-localized MGH to Mg^{2+}, the author performed a Mg^{2+} extrusion experiment using a Mg^{2+} transporter, ancient conserved domain protein/cyclin M4 (CNNM4). CNNM4 is strongly expressed in the intestinal epithelium and can extrude Mg^{2+} by stimulating Na^{+}/Mg^{2+} exchange.[35] CNNM4-FLAG and Halo-NLS were co-expressed in HEK293 cells, in which the transient expression of CNNM4 was confirmed by western blot analysis (Figure 1-8c), and the cells were incubated with MGH(AM) in 40 mM Mg^{2+} buffer. After 1 h, the extracellular solution was exchanged with Mg^{2+}-free buffer to artificially promote Mg^{2+} extrusion via CNNM4, and time-lapse fluorescence microscopic images were captured. The fluorescence intensity of nucleus-localized MGH as well as Magnesium Green immediately decreased after Mg^{2+} depletion from the extracellular buffer (Figures 1-8a and b). The fluorescence of MGH and Magnesium Green in the control cells not overexpressing CNNM4 remained constant after addition of Mg^{2+}-free buffer. Thus, it was confirmed that MGH maintained the quick fluorescence response to $[Mg^{2+}]_i$ change. Since MGH showed promise for long-term imaging, the durability of the response to Mg^{2+} was investigated. The Mg^{2+} extrusion experiment was conducted after 24 h of MGH(AM) loading to the transfected HEK293 cells. As a result, the fluorescence of MGH was quickly decreased after exchanging a buffer containing 40 mM Mg^{2+} with Mg^{2+}-free buffer (Figure 1-8d and e). This result showed that MGH retained the Mg^{2+} responsivity for 24 h in living cells.

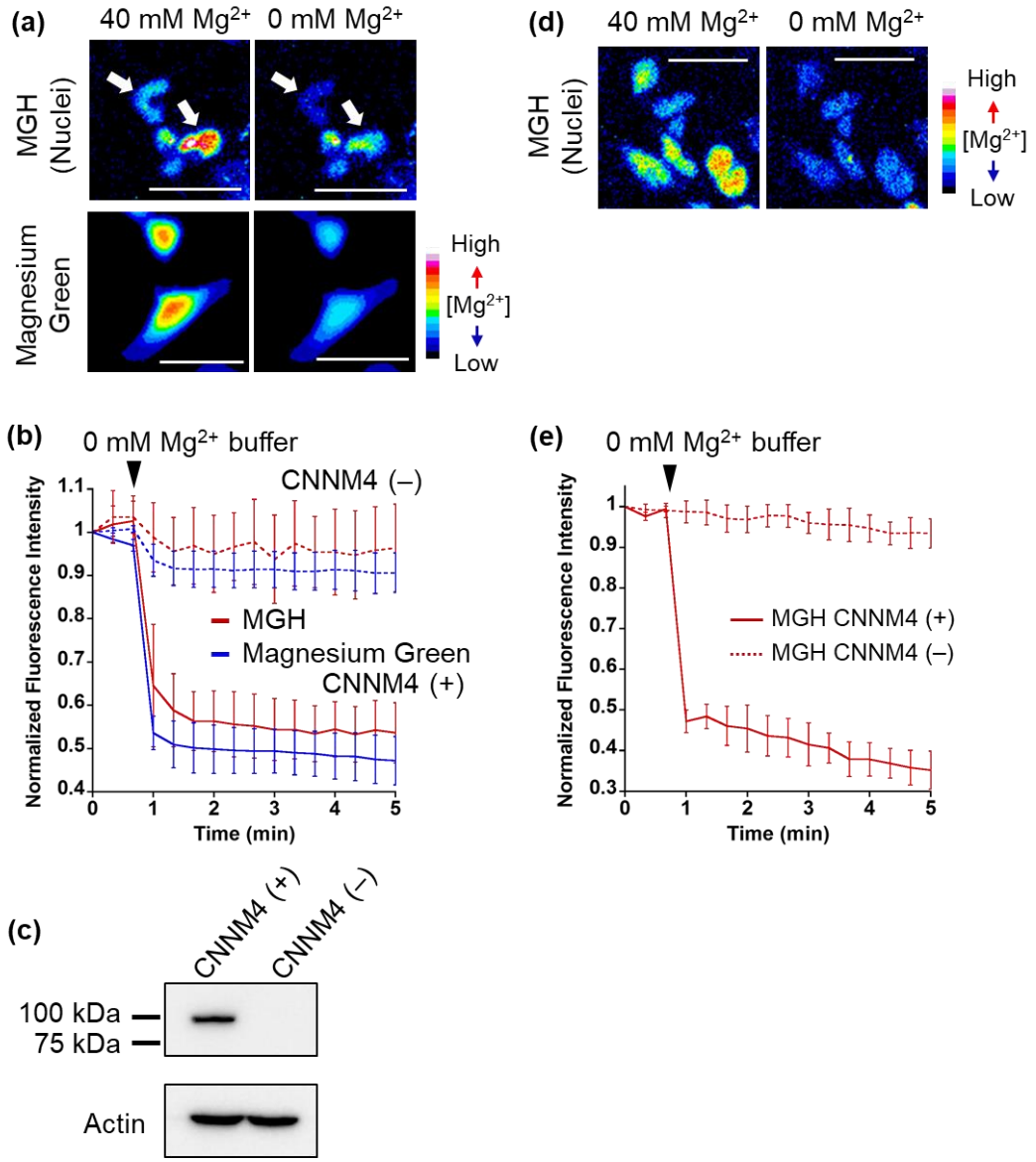

Figure 1-8. Visualization of Mg^{2+} extrusion via Mg^{2+} transporter, CNNM4, with MGH. (a) Epifluorescence microscopic images of Mg^{2+} extrusion with MGH or Magnesium Green. HEK293 cells transfected with CNNM4-FLAG and Halo-NLS were incubated with Mg^{2+}-loading buffer (78.1 mM NaCl, 5.4 mM KCl, 1.8 mM $CaCl_2$, 40 mM $MgCl_2$, 5.5 mM glucose, 5.5 mM HEPES-KOH, pH 7.4), including 5 µM MGH(AM) or 2 µM Magnesium Green(AM), for 1 h at 37 °C. These cells were subjected to Mg^{2+} depletion 1 min after the imaging started. Scale bar: 40 µm. (b) The normalized fluorescence intensity of MGH or Magnesium Green in HEK293 cells subjected to Mg^{2+} depletion. The error bars denote SD (MGH: n = 6, Magnesium Green: n = 10). (c) Western blot analysis of CNNM4-FLAG (87 kDa) transiently expressed in HEK293 cells with anti-FLAG (top) or anti-actin (bottom) antibodies. (d) Epifluorescence microscopic images of Mg^{2+} extrusion after 24 h of MGH(AM) loading. HEK293 cells were firstly transfected with Halo-NLS. After 24 h, 5 µM MGH(AM) was loaded, then the cells were transfected with CNNM4-FLAG. These cells were subjected to Mg^{2+} depletion 1 min after imaging starting. Scale bar: 20 µm. (e) The normalized fluorescence intensity of MGH in HEK293 cells subjected to Mg^{2+} depletion after 24 h of the probe loading. The error bars denote SD (n = 5).

Long-term monitoring of intracellular Mg^{2+} dynamics during apoptosis

Taking advantage of the applicability to long-term imaging, MGH was applied to investigate intracellular Mg^{2+} dynamics during apoptosis induced by anti-Fas antibody and cycloheximide (CHX). So far, anti-Fas antibody-mediated $[Mg^{2+}]_i$ increase in apoptotic B cells was fragmentally detected for 16 h with a ratiometric Mg^{2+} probe, Mag-indo-1, by flow cytometric analysis.[3] However, this method did not provide detailed information regarding the timing of Mg^{2+} mobilization along with the apoptotic process. On the other hand, use of MGH simultaneously enables real-time monitoring of $[Mg^{2+}]_i$ and changes in cellular morphology over a long time period. However, MGH exhibits an increase in fluorescence intensity without a shift in wavelength. This means that the fluorescence intensity depends not only on Mg^{2+} concentration but also on other factors such as probe concentration and light intensity. Particularly, probe concentration must be changed during apoptosis, because apoptotic cells show shrinking. Therefore, to exclude the influence of such factors, an internal standard was adopted for calibration. As the internal standard, a red fluorescent HaloTag ligand, Halo-TMR, was used to label HaloTag, and the fluorescence intensity ratio of MGH and Halo-TMR was calculated.

HeLa cells transiently expressing HaloTag in the cytoplasm were labeled with MGH(AM) for 30 min and subsequently Halo-TMR for 15 min. Then, the time-lapse imaging experiment was started, and anti-Fas antibody and CHX were added after 30 min. Alexa Fluor™ 350 annexin V conjugate, which binds phosphatidylserine-binding protein, was also treated to identify apoptotic cells. As a result, the fluorescence signal ratio of MGH and Halo-TMR increased after the apoptotic cell shrinkage, and then plateaued (Figure 1-9a). Quantitative analysis showed that $[Mg^{2+}]_i$ increased from approximately 1 to 1.8 mM during apoptosis (Figure 1-9b).

The author also checked the validity of our ratiometric imaging method with Halo-TMR as the internal standard. During long-term microscopic imaging experiments, fluorescent probes are likely to cause photobleaching. Since the photostability of fluorescent probes is dependent on the dye skeletons, the author measured the photostability of MGH and Halo-TMR using a fluorometer under continuous irradiation at 490 and 550 nm, respectively (Figure 1-9c). The fluorescence intensity of MGH decreased slightly during long-term irradiation as compared with that of Halo-TMR. Indeed, this result indicated that the fluorescence ratio of MGH/Halo-TMR may change without changes in $[Mg^{2+}]_i$ during long-term imaging experiments. Actually, long-term microscopic imaging data demonstrated that the fluorescence ratio of MGH/Halo-TMR in HaloTag-expressing HeLa cells without addition of apoptosis inducers continued to decrease slightly for several hours (Figure 1-9a), and this small ratio change could be

interpreted as the photobleaching of MGH. However, in apoptotic cells, the ratio tended to increase. Thus, the author concluded that the fluorescence ratio change in the apoptotic cells properly reflected the changes in $[Mg^{2+}]_i$. Moreover, in another control experiment, the photostability of Halo-TMR during apoptosis was examined by calculating the ratio of Halo-OG to Halo-TMR (Figure 1-9d). The fluorescence ratio of the two dyes remained constant during apoptosis. All these results supported the adequacy of our ratiometric system.

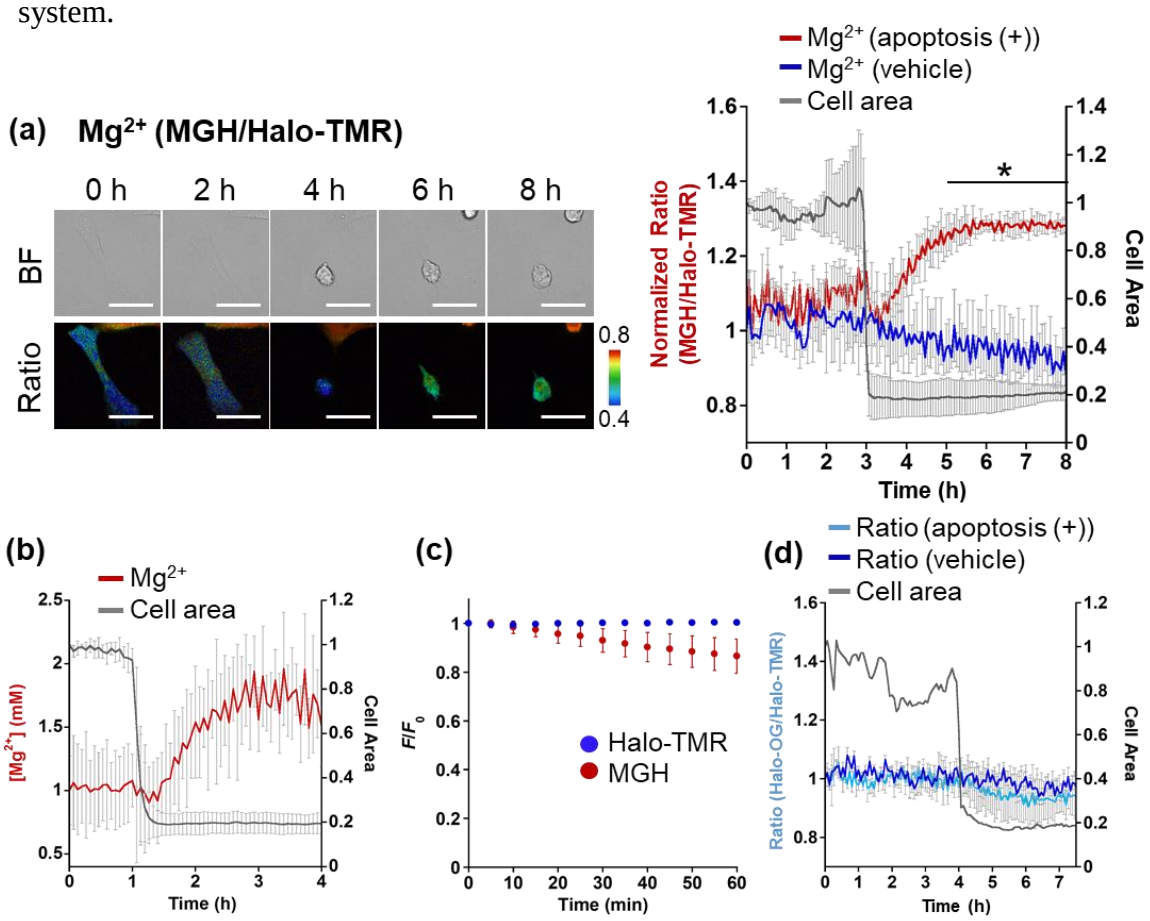

Figure 1-9. (a) Confocal fluorescence imaging of Mg^{2+} dynamics with progression of apoptosis in HeLa cells. HeLa cells were transfected with a plasmid encoding HaloTag. Fluorescence of 3 μM MGH(AM) was normalized with 50 nM Halo-TMR to exclude the influence of changes in probe concentration during apoptosis. Apoptosis inducers: anti-Fas antibody (250 ng/mL) and cycloheximide (10 μg/mL). Scale bar: 40 μm. Statistical analyses were performed with Student's *t*-test. $^*P < 0.05$. The error bars denote SD (n = 3). (b) Quantitative analysis of $[Mg^{2+}]_i$ changes during apoptosis. HaloTag-expressing HeLa cells labelled with MGH(AM) and Halo-TMR were subjected to apoptosis imaging $[Mg^{2+}]_i$ during apoptosis was quantitatively analyzed by in situ calibration. Details are given in the Experimental section. The error bars denote SD (n = 4). (c) Photostabilities of MGH and Halo-TMR during continuous irradiation (4.8 mW/cm^2). Changes in the fluorescence intensity (F) were normalized by the initial fluorescence intensity (F_0). The error bars denote SD (n = 3). (d) Fluorescence ratio changes in Halo-OG/Halo-TMR with progression of apoptosis in HeLa cells. HeLa cells expressing HaloTag were loaded with 100 nM Halo-OG and 100 nM Halo-TMR for 30 min at 37 °C. Apoptosis inducers: anti-Fas antibody (250 ng/mL) and cycloheximide (10 μg/mL). The error bars denote SD (n = 3).

As shown in Table 1-1, APTRA-based Mg^{2+} probes respond to high concentrations of Ca^{2+}. It is suggested that Ca^{2+} release from ER through the IP_3 receptor to the cytosol is one of key apoptotic processes.[36] Therefore, discrimination of the concentration changes of Ca^{2+} and Mg^{2+} is necessary. The change in $[Ca^{2+}]_i$ during apoptosis was visualized with a genetically encoded Ca^{2+}-specific fluorescent probe, R-GECO, which shows a Ca^{2+}-dependent increase in red fluorescence (K_d (Ca^{2+}) = 480 nM).[37] R-GECO barely showed a fluorescence response to Mg^{2+} introduced by the ionophore 4-bromo-A23187, in contrast to the increase in the fluorescence intensity of MGH, demonstrating sufficient specificity for Ca^{2+} (Figure 1-10). R-GECO and HaloTag were transiently expressed in HeLa cells, and the transfected cells were stained with a green fluorescent Halo-OG to accurately evaluate Ca^{2+} dynamics by monitoring the fluorescence ratio of R-GECO/Halo-OG. A sharp spike was observed immediately after the addition of apoptosis inducers, which was followed by a slight increase during apoptosis (Figure 1-11a). This large spike was not observed by monitoring the MGH/Halo-TMR ratio, indicating that MGH has a sufficiently low affinity for Ca^{2+} in the physiological range of cytosolic $[Ca^{2+}]_i$ during apoptosis (Figure 1-11b). Thus, the fluorescence response of MGH after the apoptotic cell shrinkage was ascribed to the increase of $[Mg^{2+}]_i$, not $[Ca^{2+}]_i$.

Another concern related to the increase in the fluorescence ratio of MGH/Halo-TMR is equilibration of intracellular and extracellular metal ions due to the loss of cell membrane integrity in the late stages of apoptosis.[38] During apoptosis imaging, the author observed further significant increases in the fluorescence ratios of both MGH/Halo-TMR and R-GECO/Halo-OG following increases in the ratios after apoptotic cell shrinkage (Figure 1-11, blue squares). This large fluorescence response during the late apoptotic stage is thought to reflect the loss of cell membrane integrity and the influx of extracellular metal ions, particularly Ca^{2+} (Ca^{2+} concentration in DMEM is approximately 1.8 mM).

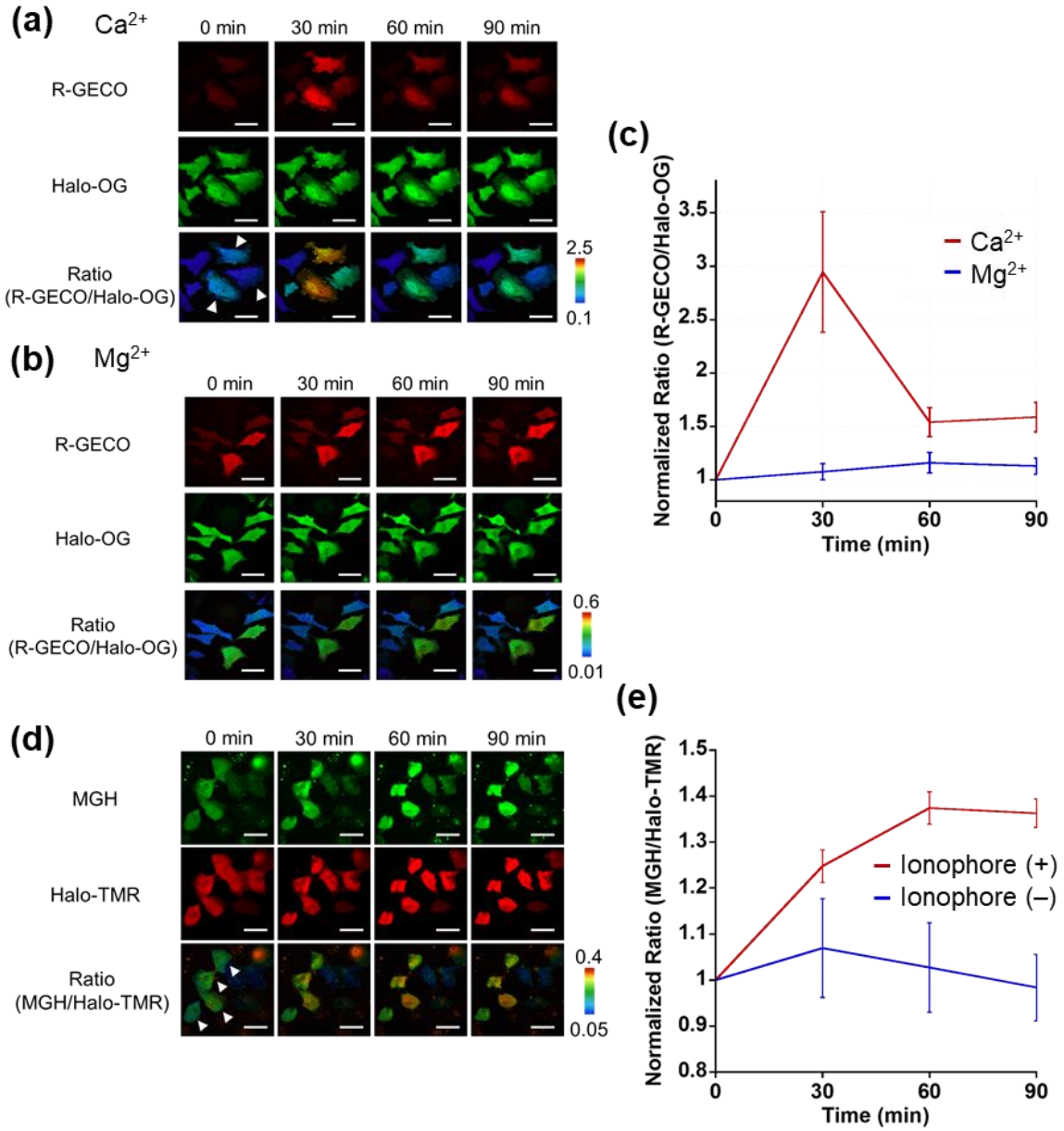

Figure 1-10. Evaluation of the response of R-GECO to (a) Ca^{2+} and (b) Mg^{2+} in living HeLa cells. The intracellular concentrations of Mg^{2+} and Ca^{2+} were changed using an ionophore, 4-bromo-A23187. HeLa cells were transfected with plasmids encoding R-GECO and HaloTag, then HaloTag was labeled with 50 nM Halo-OG. The cells were treated with 2.5 µM 4-bromo-A23187 and (a) 100 µM Ca^{2+} or (b) 30 mM Mg^{2+}. The fluorescence of R-GECO was normalized to that of Halo-OG to exclude the influence of changes in probe concentrations during imaging. Scale bar: 40 µm. (c) The normalized fluorescence ratios of R-GECO/Halo-OG are presented as line plots. The error bars denote SD (n = 3). (d) Evaluation of the response of MGH to Mg^{2+} in living HeLa cells. The intracellular concentration of Mg^{2+} was changed using 4-bromo-A23187. HeLa cells were transfected with a plasmid encoding HaloTag. HaloTag was labeled with 3 µM MGH(AM) for 30 min and then 50 nM Halo-TMR for 15 min. The cells were treated with 2.5 µM 4-bromo-A23187 and 30 mM Mg^{2+}. The fluorescence of MGH was normalized to that of Halo-TMR to exclude the influence of changes in probe concentrations during imaging. Scale bar: 40 µm. (e) The normalized fluorescence ratios of MGH/Halo-TMR are presented as line plots. The error bars denote SD (n = 3).

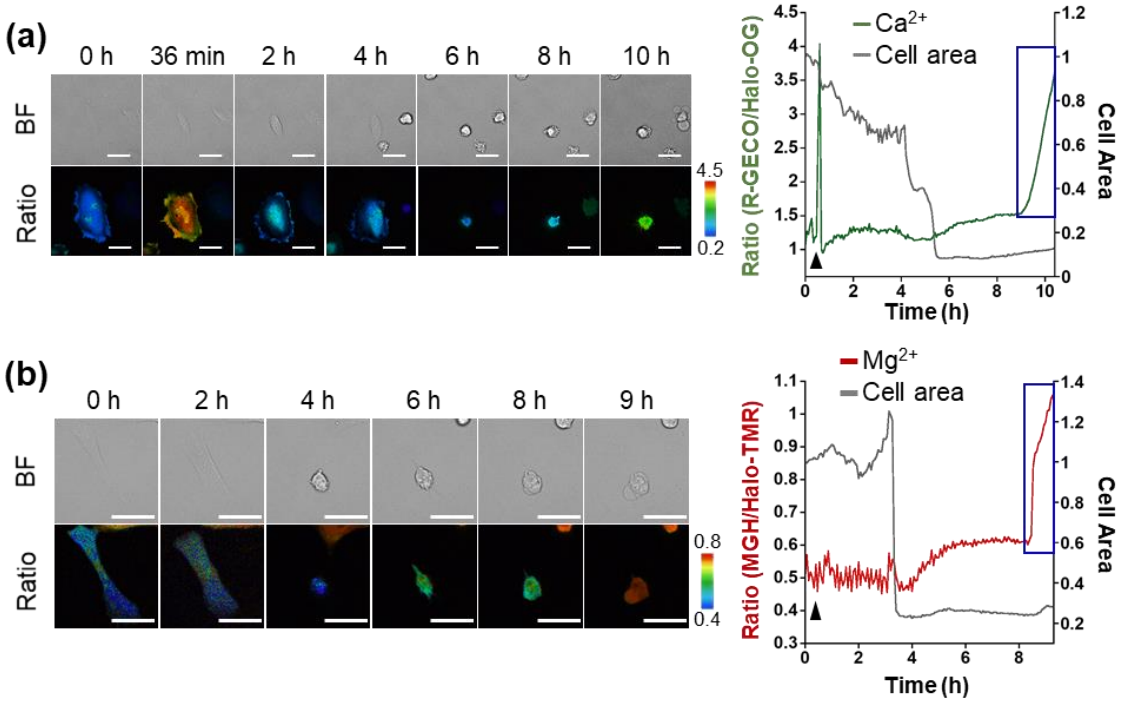

Figure 1-11. Lack of integrity of the cell membrane during the late stages of apoptosis. Representative confocal fluorescence images of (a) Ca^{2+} or (b) Mg^{2+} dynamics with progression of apoptosis in HeLa cells. Anti-Fas antibody (250 ng/mL) and cycloheximide (10 μg/mL) as apoptosis inducers were added at the indicated time point (arrow). Scale bar: 40 μm.

To elucidate the mechanism of $[Mg^{2+}]_i$ increase during apoptosis, the author focused on the correlation between $[Mg^{2+}]_i$ and intracellular ATP concentration; since most ATP forms a complex with Mg^{2+} in cells,[39] $[Mg^{2+}]_i$ is likely to be affected by ATP concentration. In fact, it has been reported that various stimulations, such as cyanide,[40] fructose,[41] and anoxia,[42] trigger an increase in $[Mg^{2+}]_i$ with a decrease in intracellular ATP or degradation of ATP to ADP or AMP. These reports suggested a close relationship between Mg^{2+} and ATP levels. Another previous study showed that intracellular ATP was released from apoptotic cells through the plasma membrane channel pannexin 1 (PANX1) to recruit monocyte.[43] Hence, the time course of ATP concentration change in apoptotic HeLa cells was visualized using a caspase-resistant version of ATeam,[44] a genetically encoded fluorescence resonance energy transfer (FRET)-based ATP sensor.[45] As a result, the ATP level significantly decreased in apoptotic cells after cell shrinkage (Figure 1-12a).

Although the simultaneous imaging of $[Mg^{2+}]_i$ and ATP concentration in apoptotic cells was desirable, it was not possible because the excitation and emission wavelengths of MGH and ATeam largely overlap. Therefore, fluorescence ratio changes for $[Mg^{2+}]_i$ and intracellular ATP concentration were plotted from 1 h before the cell shrinkage (Figure 1-12b). The time-course graphs of both concentrations indicated that $[Mg^{2+}]_i$ and intracellular ATP concentration were almost inversely correlated.

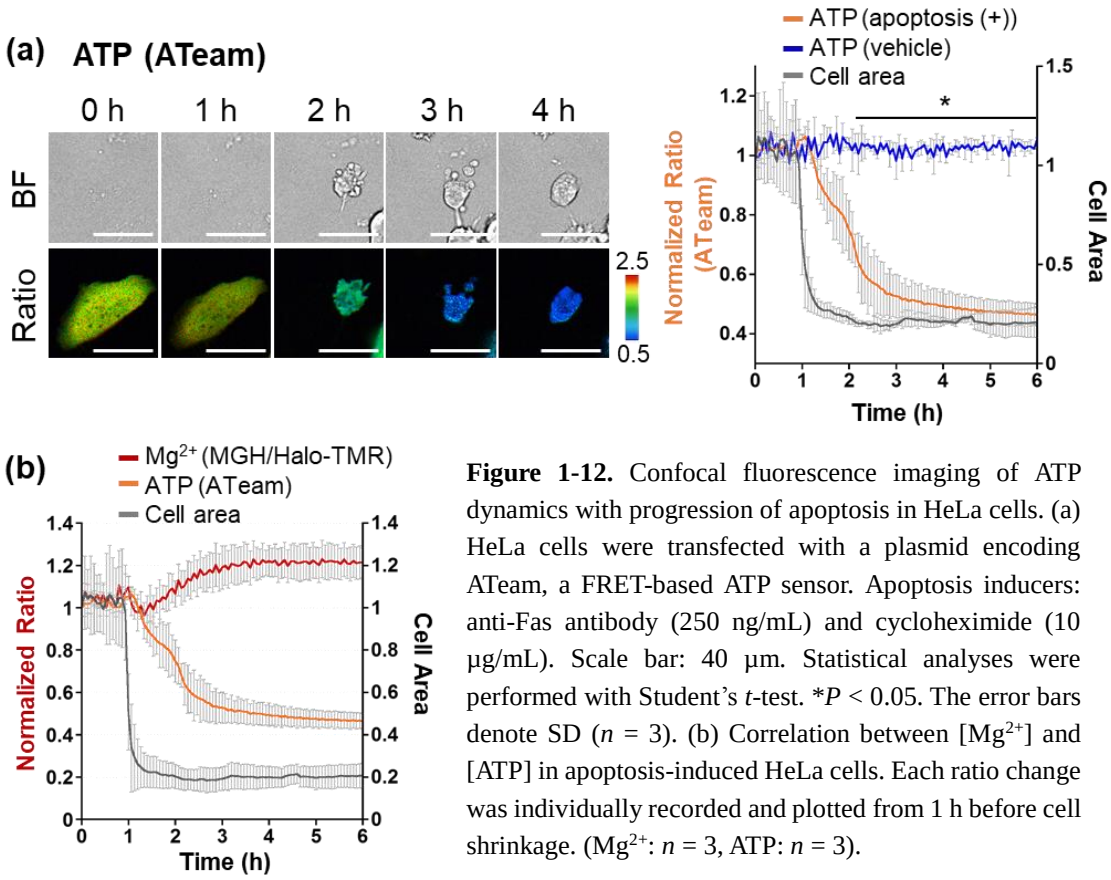

Figure 1-12. Confocal fluorescence imaging of ATP dynamics with progression of apoptosis in HeLa cells. (a) HeLa cells were transfected with a plasmid encoding ATeam, a FRET-based ATP sensor. Apoptosis inducers: anti-Fas antibody (250 ng/mL) and cycloheximide (10 µg/mL). Scale bar: 40 µm. Statistical analyses were performed with Student's *t*-test. **P* < 0.05. The error bars denote SD (*n* = 3). (b) Correlation between [Mg^{2+}] and [ATP] in apoptosis-induced HeLa cells. Each ratio change was individually recorded and plotted from 1 h before cell shrinkage. (Mg^{2+}: *n* = 3, ATP: *n* = 3).

The author hypothesized that the increase of Mg^{2+} level arose from disassociation of Mg^{2+} from ATP released by PANX1 channels in apoptotic cells. To confirm this hypothesis, ATP release from apoptotic cells was blocked by probenecid, an inhibitor of PANX1 channels.[43,46] In probenecid-treated HeLa cells, decrease of ATP level was not observed during apoptosis (Figure 1-13a). Furthermore, intracellular Mg^{2+} level also remained constant during apoptosis (Figure 1-13b). These data showed that free Mg^{2+} was released in apoptotic cells in association with the PANX1-mediated extracellular ATP release. This is the conclusive observation that Mg-ATP is also one of possible source of free Mg^{2+}. Importantly, a variety of endonucleases involved in DNA fragmentation during apoptosis requires Mg^{2+} to digest DNA.[47] The increase in Mg^{2+} levels after the cell shrinkage may be relevant to endonuclease activities. Further studies will be necessary to investigate the role of Mg^{2+} following apoptotic cell shrinkage.

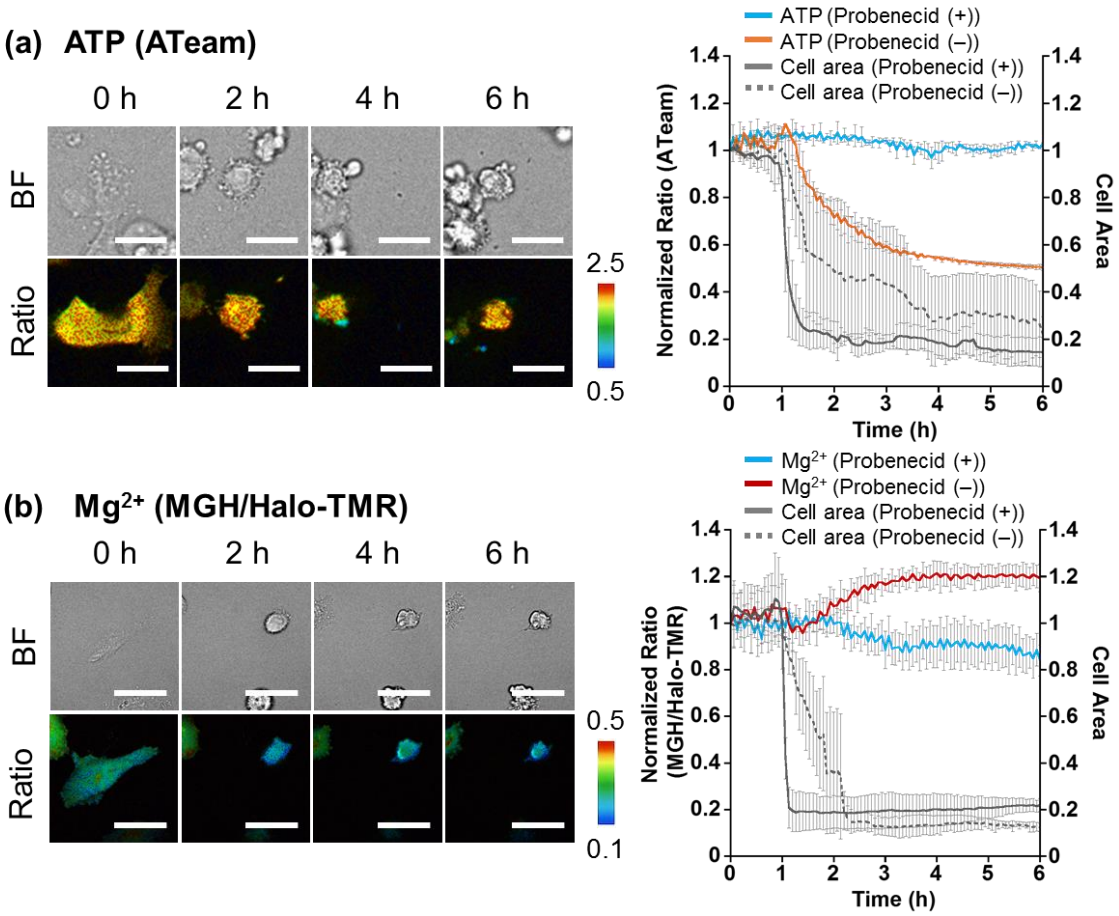

Figure 1-13. Confocal fluorescence imaging of (a) ATP or (b) Mg^{2+} concentration changes with progression of apoptosis in probenecid-treated HeLa cells. (a) HeLa cells were transfected with a plasmid encoding ATeam. (b) HeLa cells were transfected with a plasmid encoding HaloTag. Fluorescence of 3 µM MGH(AM) was normalized with 50 nM Halo-TMR to exclude the influence of changes in probe concentration during apoptosis. Anti-Fas antibody (250 ng/mL), cycloheximide (10 µg/mL) and probenecid (1.5 mM) were added before imaging. Scale bar: 40 µm. (Mg^{2+}: n = 3, ATP: n = 3).

Discussion

Fluorescence imaging with higher temporal and spatial resolution is a crucial technique for the analysis of target molecules. To elucidate the intracellular dynamics and physiological roles of free Mg^{2+}, this imaging system requires the long-term retention and localization of fluorescent Mg^{2+} probes in living cells. However, existing Mg^{2+} probes have not been suitable for such experiments, especially for long-term imaging. To overcome this problem, the author developed a combined system of a novel small-molecule Mg^{2+} probe, MGH, and a HaloTag, which is genetically localized in a variety of organelles. This noteworthy feature improved the spatiotemporal resolution for detecting intracellular Mg^{2+} dynamics, enabling the investigation of unexplored

phenomena related to Mg^{2+}. Recently, Buccella and the co-workers reported a similar imaging system combining a ratiometric Mg^{2+} probe, Mag-S-Tz, and HaloTag.[13] This probe was also localized at the target subcellular compartments in living cells after the labeling of a strained bicyclononyne ligand to HaloTag and the subsequent fluorogenic click reaction between Mag-S-Tz and the bicyclononyne. However, this two-step strategy requires more than 4 h to start the imaging experiment, and long-term imaging has not been achieved. Therefore, MGH is the first imaging probe that demonstrated long-term time-lapse imaging of local Mg^{2+} dynamics in living cells for 24 h.

Apoptosis is a process that takes several hours. Therefore, long-term imaging is essential for the clarification of intracellular free Mg^{2+} dynamics in apoptotic cells. In the 1990s, some groups showed an $[Mg^{2+}]_i$ increase during apoptosis.[2,3] However, more detailed mechanisms and timing of the $[Mg^{2+}]_i$ increase have been unclear owing to the lack of long-term Mg^{2+} imaging methods. MGH had suitable properties for long-term monitoring of $[Mg^{2+}]_i$ change during apoptosis. However, MGH showed a simple fluorescence in response to the change of $[Mg^{2+}]$ without an excitation or emission wavelength shift. This fluorescence spectral property was not ideal for the analysis of apoptotic cells because the fluorescence intensity is considerably affected by the probe concentration change during apoptosis. This problem was solved by introducing Halo-TMR as an internal standard, and thus calculating the signal ratio between MGH and Halo-TMR. Ratiometric two-fluorophore sensing systems have been employed in Ca^{2+} and Zn^{2+} imaging.[48,49] In addition, extracellular leakage of the internal standard during long-term imaging was prevented by using Halo-TMR in HaloTag-expressing cells.

The data analysis of Mg^{2+} and ATP imaging with MGH and ATeam suggested that the $[Mg^{2+}]_i$ increase after apoptotic cell shrinkage was caused by the dissociation of Mg^{2+} from ATP in association with the extracellular release of ATP through PANX1 channels. Suppression of $[Mg^{2+}]_i$ increase by a PANX1 inhibitor, probenecid, clearly demonstrated that the Mg-ATP is a main resource for the Mg^{2+} increase after the cell shrinkage. Although a close correlation between $[Mg^{2+}]_i$ and ATP levels has been previously reported, further evidence was suggested by biochemical characterization after the cell lysis without direct visualization of both molecular behaviors in cells.[41] Therefore, our result provides strong evidence regarding $[Mg^{2+}]_i$ increase as a consequence of intracellular ATP depletion.

In HeLa cells, the intracellular ATP concentration was estimated at 3–4 mM,[50,51] and it was reported that the intracellular ATP concentration in human T cells was almost depleted during apoptosis.[52] If all of the discharged ATP released Mg^{2+} in cells, $[Mg^{2+}]_i$, which is maintained at the hundred-micromolar level in living cells, would increase to the

several-millimolar level. However, $[Mg^{2+}]_i$ increased by only approximately 0.8 mM during apoptosis (Figure 1-9b). This result suggested two possibilities: (1) PANX1 channels released some extent of Mg-ATP complexes or (2) increased Mg^{2+} was buffered by Mg^{2+} transporters or channels. Recently, some Mg^{2+} transporters and channels were identified in the cell membrane and in the membrane of intracellular organelles (e.g. mitochondria and Golgi).[39] These Mg^{2+} transport mechanisms may contribute to the regulation of intracellular Mg^{2+} homeostasis. Since MGH can be localized on a Mg^{2+} transporter by tandemly expressed HaloTag, Mg^{2+} influx via Mg^{2+} transporters would be visualized using such organelle-localized probes. Further study with MGH should lead to the elucidation of Mg^{2+}-buffering mechanisms in apoptotic cells.

Experimental Methods

Materials and instruments

All chemicals used for organic synthesis were of the best grade available, supplied by Tokyo Chemical Industries, Wako Pure Chemical, or Sigma-Aldrich Chemical Co., and were used as received without further purification. The pcDNA-3.1-(+) vector was purchased from Invitrogen (21083-027). Restriction endonucleases and PrimeSTAR® HS DNA polymerase were purchased from Takara Bio, Inc. Plasmid DNA was isolated using a QIAprep Spin Miniprep kit (Qiagen). MGH(AM) was dissolved in DMSO (biochemical grade, Wako) before fluorescence measurements to facilitate solubilization in aqueous solution. HaloTag TMR Ligand and HaloTag Oregon Green Ligand were purchased from Promega. Anti-Fas (CH11) antibody was purchased from MBL. Cycloheximide was purchased from Wako. CMV-R-GECO1 was purchased from Addgene. Annexin V (Alexa Fluor 350) and Annexin V (Alexa Fluor 680), Magnesium Green, Magnesium Green(AM), ER-Tracker Red and MitoTracker Deep Red FM were purchased from Thermo Fisher Scientific. 2-deoxyglucose was purchased from Wako Pure Chemical. KCN was purchased from Tokyo Chemical Industries. 4-bromo-A23187 was purchased from Sigma-Aldrich.

GPC purifications were performed with a JAIGEL 1H-2H column (Japan Analytical Industry Co., Ltd.) using a GPC system that was comprised of a pump (LC-6AD, Shimadzu) and a detector (SPD-20A, Shimadzu). HPLC analyses were performed with an Inertsil ODS-3 (4.6 mm×250 mm) column (GL Sciences Inc.) by using an HPLC system that was comprised of a pump (PU-2080, Jasco) and a detector (MD-2010 or FP-2020, Jasco). Preparative HPLC was performed with an Inertsil ODS-3 (10.0 mm × 250 mm) column (GL Sciences Inc.) using an HPLC system that was comprised of a pump (PU-2087, Jasco) and a detector (UV-2075, Jasco). Buffer A was composed of 0.1% HCOOH in H_2O (for MGH(AM)) or 50 mM triethylammonium acetate in H_2O (for MGH); Buffer B was composed of 0.1% HCOOH in acetonitrile (for MGH(AM)) or pure acetonitrile (for MGH). NMR spectra were recorded on a JEOL JNM-AL400 instrument at 400 MHz for ^{1}H and at 100 MHz for ^{13}C NMR or a Bruker Avance 500 instrument at 500 MHz for ^{1}H NMR and 125 MHz for ^{13}C NMR, using tetramethylsilane as an internal standard. Mass spectra were measured either on a Waters LCT-Premier XE or on a JMS-700 (JEOL) mass spectrometer.

Fluorescence spectra were measured by using a Hitachi F7000 spectrometer. The slit widths were 2.5 nm for both excitation and emission, and the photomultiplier voltage was 700 V. UV-visible absorption spectra were measured using a Jasco aV-650 spectrophotometer. For photostability analysis of MGH and Halo-TMR, light irradiation

was performed using a Xe light source (MAX-303; Asahi Spectra) equipped with band pass filters (490/5 nm for MGH; 550/5 nm for Halo-TMR).

The fluorescence microscopic images were recorded using a confocal fluorescence microscopic imaging system including a fluorescence microscope (IX71, Olympus), an EMCCD (iXon3, Andor Technology), a confocal scanner unit (CSU-X1, Yokogawa Electric Corporation), and a multispectral LED light source (Spectra X light engine, Lumencor). The filter sets were BP377 ± 25/DM405/BA447 ± 30 (for Hoechst 33342, Alexa Fluor350), BP438 ± 12/DM442/BA482 ± 17 and BA562 ± 20 (for ATeam), BP488 ± 3/DM488/BA520 ± 17.5 (for MGH, Magnesium Green and Halo-OG), BP560 ± 13/DM561/BA624 ± 20 (for ER-Tracker™ Red, R-GECO1.0, Halo-TMR) and BP640 ± 7/DM647/BA692 ± 20 (for MitoTracker® Deep Red FM and Alexa Fluor680). The entire system was controlled by using the MetaMorph 7.6 software (Molecular Devices).

Fluorometric analysis

The relative fluorescence quantum yields of the compounds were obtained by comparing the area under the emission spectrum. The following equation was used to calculate the quantum yield:

$$\Phi_x = \Phi_{st} (I_x/I_{st})(A_{st}/A_x)(n_x^2/n_{st}^2)$$

, where Φ_{st} is the reported quantum yield of the standard, I is the integrated emission spectrum, A is the absorbance at the excitation wavelength, and n is the refractive index of the solvent. The subscripts x and st denote the sample and the standard, respectively. Fluorescein (Φ = 0.85 when excited at 492 nm in 100 mM NaOH aq.) was used as the standard.

The photostabilities of MGH and Halo-TMR (1 μM, 2 mL) were examined in 100 mM HEPES buffer (pH 7.4) with 115 mM KCl and 20 mM NaCl at 25 °C under continuous irradiation through band pass filters (490 ± 2.5 nm for MGH, 550 ± 2.5 nm for Halo-TMR, 4.8 mW/cm^2) using a Xe light source. The fluorescence intensities of MGH (λ_{ex} = 515 nm, λ_{em} = 538 nm) and Halo-TMR (λ_{ex} = 555 nm, λ_{em} = 579 nm) were measured every 5 min for 1 h.

Determination of dissociation constants

The apparent dissociation constants (K_d) of MGH, HaloTag-MGH, and Magnesium Green for Mg^{2+} and Ca^{2+} in 100 mM HEPES buffer (pH 7.4) including 115 mM KCl and 20 mM NaCl at 37 °C were calculated using the following equation,

$$[M^{2+}] = K_d (F–F_{min})/(F_{max}–F)$$

, where F is the fluorescence intensity at each metal ion concentration, F_{min} is the

fluorescence intensity before addition of the metal ions, and F_{max} is the fluorescence intensity at the saturation state.

Metal ion selectivity study

Metal ion selectivity was measured by adding either $MgCl_2$, $CaCl_2$, $ZnCl_2$, $CoCl_2$, $MnCl_2$, $NiCl_2$ or $CuCl_2$ in 100 mM HEPES buffer (pH 7.4) with 115 mM KCl, 20 mM NaCl and 1 μM MGH at 37 °C.

Construction of plasmids

pcDNA-3.1-(+)-HaloTag

The DNA fragment of HaloTag was amplified from pFC14A-HaloTag, which was purchased from Promega, by PCR using primers (forward primer: 5'-AAAGACGCTAGCGCCGCCATGGGATCCGAAATCGGTACTG-3', reverse primer: 5'-ATAGCAAAGCTTACCGGAAATCTCCAGAGT-3'). The fragment was cleaved using *Nhe*I and *Hind*III, then ligated to *Nhe*I-*Hind*III site of pcDNA-3.1-(+)-BL-tag[53] treated with the same restriction enzymes to generate pcDNA-3.1-(+)-HaloTag.

pcDNA-3.1-(+)-Halo-NLS

The DNA fragment of HaloTag was amplified from pFC14A-HaloTag by PCR using primers (forward primer: 5'-AAAGACGCTAGCGCCGCCATGGGATCCGAAATCGGTACTG-3', reverse primer: 5'-GCGACTAAGCTTACCGGAAATCTCCAGAGTAGAC-3'). The fragment was cleaved using *Nhe*I and *Hind*III, then ligated to *Nhe*I-*Hind*III site of pcDNA-3.1-(+)-BL-NLS[53] treated with the same restriction enzymes to generate pcDNA-3.1-(+)-Halo-NLS.

pcDNA-3.1-(+)-Lyn_{11}-Halo

The DNA fragment of HaloTag was amplified from pFC14A-HaloTag by PCR using primers (forward primer: 5'-AAAGACGGATCCGCCGCCATGGGATCCGAAATCGGTACTG-3', reverse primer: 5'-ATAGCAGAATTCACCGGAAATCTCCAGAGTAGAC-3'). The fragment was cleaved using *Bam*HI and *Eco*RI, then ligated to *Bam*HI- *Eco*RI site of pcDNA-3.1-(+) vector. The constructed plasmid was digested with *Hind*III and *Bam*HI and ligated in-frame into a similarly digested Lyn_{11} oligo DNA. The Lyn_{11} oligo DNA was amplified from a purchased oligo nucleotide template (5'-AATTAAAAGCTTGCCGCCATGGGATGTATAAAATCAAAAGGGAAAGACAGCGCGGGAGCAGATAGTGCTGGTAGTGCTGGTAGTGCTGGTGGATCCATCGGA-3' and 5'-TCCGATGGATCCACCAGCACTACCAGCACTACCAGCACTATCTGCTCC

CGCGCTGTCTTTCCCTTTTGATTTTATACATCCCATGGCGGCAAGCTTTTAATT-3’; Gene Design, Inc.) using the following primers (forward primer: 5’-AATTAAAAGCTTGCCGC-3’, reverse primer: 5’-AGGCTAGGATCCACCAG-3’).

pKmc-2xCOX8-Halo

The DNA fragment of HaloTag was amplified from pFC14A-HaloTag by PCR using primers (forward primer: 5’-GATAACGGATCCATGGGCTCCGAAATCG-3’, reverse primer: 5’-AAGATCGAATTCTTAACCGGAAATCTCCAGAGTAGAC-3’). The fragment was cleaved using *Bam*HI and *Eco*RI, then ligated to pKmc-2xCOX8-BL, which was a kind gift from Dr. Atsushi Miyawaki, treated with the same restriction enzymes to generate pKmc-2xCOX8-Halo.

pCMV-Halo-ER

The DNA fragment of HaloTag was amplified from pFC14A-HaloTag by PCR using primers (forward primer: 5’-GATAACACCGGTCGCCACCATGGGCTCCGAAATCG-3’, reverse primer: 5’-AAGATCAGATCTACCTCCTCCACCACCGGAAATCTCCAG AGTAGAC-3’). The fragment was cleaved using *Age*I and *Bgl*II, then ligated to pmKate2-ER, which was purchased from Evrogen (FP324), treated with the same restriction enzymes to generate pCMV-Halo-ER.

pET21b(+)-His-Halo

The DNA fragment of HaloTag was amplified from pFC14A-HaloTag by PCR using primers (forward primer: 5’-GATAACGGATCCGGAAGGATTTCACATATGGGCTCC GAAATCGGTACTGG-3’, reverse primer: 5’-AAGATCAAGCTTCTAACCGGAAATC TCCAGAGTAG-3’). The fragment was cleaved using *Bam*HI and *Hin*dIII then ligated to pET21b(+)-PYP3R[54] treated with the same restriction enzymes to generate pET21b(+)-His-Halo.

Preparation of HaloTag protein

Hexahistidine-tagged HaloTag was overexpressed in Escherichia coli cells, BL21 (DE3), then the cells were cultivated in Luria-Bertani medium at 37 °C. When the OD_{600} of the culture medium reached 0.6–0.8, the culture flask was incubated at 20 °C and isopropyl-β-D-thiogalactopyranoside (final concentration: 100 μM) was added to the medium. After protein expression was induced overnight, the cells were collected by centrifugation at 4,700 ×*g* for 12 min, and were resuspended in 50 mM sodium phosphate buffer (pH 8.0) with 300 mM NaCl. After cell lysis by sonication, the lysate was

centrifuged at 32,000 ×*g* for 20 min. The supernatant was loaded on cOmplete His-Tag Purification Resin. After the resin was washed with 50 mM sodium phosphate buffer (pH 8.0) with 300 mM NaCl and 5 mM imidazole, proteins adsorbed on the resin were eluted using 50 mM sodium phosphate buffer (pH 8.0) with 300 mM NaCl and 250 mM imidazole. Further purification was conducted by size exclusion chromatography (Superdex TM 75 10/300 GL, GE healthcare) using 100 mM HEPES buffer (pH 7.4) with 1 mM DTT to prevent dimerization of HaloTag. The purified protein was analyzed by SDS-PAGE for the purity check.

Detection of protein labeling by SDS-PAGE

HaloTag (40 μM) was added to a solution of MGH (30 μM) in 100 mM HEPES buffer (pH 7.4) with 115 mM KCl and 20 mM NaCl at 37 °C. After incubation for 1 h, the labeled protein was denatured in 2×SDS gel loading buffer (100 mM Tris-HCl buffer (pH 6.8), 4% SDS, 20% glycerol, and 10% mercaptoethanol) and resolved by SDS-PAGE. The fluorescence image of the gel was captured using a fluorescence image analyzer (Typhoon FLA 9500, GE Healthcare Bio-Sciences AB). The gels were stained with Coomassie Brilliant Blue prior to the capture of images.

Western blot analysis

HEK293 cells expressing CNNM4-FLAG in 24-well plates were lysed using 100 μL lysis buffer (100 mM Tris-HCl (pH 6.8), 4% SDS, 20% glycerol, and 100 mM DTT). The lysates were resolved by 10% SDS-PAGE and transferred onto polyvinylidene difluoride membranes. Anti-FLAG antibodies (1:1000) were used for detection of CNNM4-FLAG. Chemiluminescence was detected using the Amersham ECL Plus Western Blotting Detection System (GE Healthcare).

Cell culture

HEK293T cells, HEK293 cells, and HeLa cells were cultured in high-glucose Dulbecco's modified Eagle medium (DMEM) plus Gluta Max-I supplemented with 10% fetal bovine serum (FBS), 100 U/mL penicillin, and 100 μg/mL streptomycin. The cells were incubated at 37 °C in a humidified atmosphere of with 5% CO_2. A subculture was performed every 2–3 days from subconfluent (<80%) cultures using a trypsin-ethylenediamine tetraacetic acid solution. Transfection of plasmids was carried out in a glass-bottomed dish using Lipofectamine 3000 or 2000 according to the standard protocol.

Live-cell fluorescence imaging of MGH localization

HEK293T cells maintained in 10% FBS in DMEM at 37 °C in 5% CO_2 were transfected with pcDNA-3.1-(+)-Halo-NLS, pcDNA-3.1-(+)-Lyn_{11}-Halo, pcDNA-3.1-(+)-HaloTag, pKmc-2xCOX8-Halo or pCMV-Halo-ER plasmids using Lipofectamine 3000, and the cells were incubated at 37 °C for 24 h. Then, the cells were washed three times with HBSS and incubated in FBS-free DMEM containing 3 μM MGH(AM) for 1 h in a CO_2 incubator. After washing with HBSS, fluorescence images were captured in DMEM containing 10% FBS using a confocal fluorescence microscope at 37 °C.

Mg^{2+} extrusion experiments

HEK293 cells were transfected with pCMV-CNNM4-FLAG and pcDNA-3.1-(+)-Halo-NLS using Lipofectamine 2000, and the cells were incubated at 37 °C for 24 h. Then, the cells were incubated with Mg^{2+}-loading buffer (78.1 mM NaCl, 5.4 mM KCl, 1.8 mM $CaCl_2$, 40 mM $MgCl_2$, 5.5 mM glucose, 5.5 mM HEPES-KOH, pH 7.4), including 5 μM MGH(AM) or 2 μM Magnesium Green, for 1 h at 37 °C. The cells were rinsed once with loading buffer and viewed using an epifluorescence microscope (IX81 equipped with a DP30BW camera and a USH-1030L mercury lamp; Olympus). Fluorescence was measured every 20 s (excitation at 470–490 nm and emission at 505–545 nm) under the control of the MetaMorph software (Molecular Devices). Then, the buffer was changed to a Mg^{2+}-free buffer ($MgCl_2$ in the loading buffer was replaced with 60 mM NaCl). The Mg^{2+} extrusion experiment 24 h after loading MGH(AM) to HEK293 cells was performed as follows. HEK293 cells were firstly transfected with pcDNA-3.1-(+)-Halo-NLS, and the cells were incubated at 37 °C for 24 h. The cells were incubated with 5 μM MGH(AM) in DMEM (FBS free) for 1 h at 37 °C, and then the cells were transfected with pCMV-CNNM4-FLAG at 37 °C for 24 h. After incubation with Mg^{2+}-loading buffer for 30 min, the cells were rinsed once with loading buffer and viewed using an epifluorescence microscope.

Metal ion responsivity of MGH and R-GECO in HeLa cells

(a: R-GECO) HeLa cells were transfected with plasmids encoding R-GECO and HaloTag using Lipofectamine 3000. After 24 h, the cells were washed three times with HBSS and incubated in FBS-free DMEM containing 50 nM Halo-OG for 30 min at 37 °C under 5% CO_2. After washing with HBSS (free Ca^{2+} and Mg^{2+}), the cells were bathed in HBSS (free Ca^{2+} and Mg^{2+}). The cells were then treated with 2.5 μM 4-bromo-A23187 and 100 μM Ca^{2+} or 30 mM Mg^{2+}. The fluorescence of R-GECO was normalized according to the fluorescence of Halo-OG to exclude the influence of changes in the probe

concentration and the fluctuations in the light intensity.

(b: MGH) HeLa cells were transfected with a plasmid encoding HaloTag using Lipofectamine 3000. After 24 h, the cells were washed three times with HBSS, incubated in FBS-free DMEM containing 3 μM MGH(AM) for 30 min, and then treated with 50 nM Halo-TMR for 15 min at 37 °C under 5% CO_2. After washing with HBSS (free Ca^{2+} and Mg^{2+}), the cells were bathed in HBSS (free Ca^{2+} and Mg^{2+}). The cells were then treated with 2.5 μM 4-bromo-A23187 and 30 mM Mg^{2+}. The fluorescence of MGH was normalized according to the fluorescence of Halo-TMR to exclude the influence of changes in the probe concentration and fluctuations in the light intensity.

Fluorescence imaging during apoptosis

(a: Mg^{2+}) HeLa cells maintained in 10% FBS in DMEM at 37 °C in 5% CO_2 were transfected with the pcDNA-3.1-(+)-HaloTag plasmid using Lipofectamine 3000. After 24 h, the cells were washed twice with HBSS, incubated with 3 μM MGH(AM) for 30 min, and then treated with 50 nM Halo-TMR for 15 min at 37 °C under 5% CO_2. After washing with HBSS, fluorescence images were captured in DMEM containing 10% FBS and 5 μL AnnexinV (Alexa Fluor 350) using a confocal fluorescence microscope at 37 °C. Anti-Fas antibody (250 ng/mL) and cycloheximide (10 μg/mL) were added 30 min after the imaging started. Change in $[Mg^{2+}]_i$ was determined using the following equation:

$$[Mg^{2+}]_i = K_d\, Q(R–R_{min})/(R_{max}–R)$$

, where R is the signal ratio of MGH/Halo-TMR, R_{min} is the minimum value of R, R_{max} is the maximum value of R, Q is the signal ratio of Halo-TMR under minimum Mg^{2+} concentration to Halo-TMR under maximum Mg^{2+} concentration, and K_d is 0.67 mM for Halo-MGH. R_{min} and R_{max} were calculated after imaging experiments as follows. The apoptotic cells were washed with Mg^{2+}- and Ca^{2+}-free HHBSS buffer, then permeabilized with 20 μg/mL digitonin in Mg^{2+}- and Ca^{2+}-free HHBSS for 5 min. After washing the cells with Mg^{2+}- and Ca^{2+}-free HHBSS buffer, R_{min} was recorded by incubating the cells in Mg^{2+}- and Ca^{2+}-free HHBSS buffer containing 10 mM EDTA at 37 °C for 10 min. Then, R_{max} was recorded by incubating the cells in Ca^{2+}-free HHBSS buffer containing 50 mM $MgCl_2$ at 37 °C for 10 min.

(b: Ca^{2+}) HeLa cells maintained in 10% FBS in DMEM at 37 °C in 5% CO_2 were transfected with the pcDNA-3.1-(+)-HaloTag and CMV-R-GECO1 plasmids using Lipofectamine 3000. After 24 h, the cells were washed twice with HBSS and incubated with 100 nM Halo-OG for 30 min at 37 °C under 5% CO_2. After washing with HBSS, fluorescence images were captured in DMEM containing 10% FBS and 5 μL AnnexinV (Alexa Fluor 350) using a confocal fluorescence microscope at 37 °C.

(c: ATP) HeLa cells maintained in 10% FBS in DMEM at 37 °C in 5% CO_2 were transfected with the pcDNA-3.1-(+)-ATeam plasmid using Lipofectamine 3000. After 24 h, the cells were washed two times with HBSS; then, fluorescence images were captured in DMEM containing 10% FBS and 5 µL AnnexinV (Alexa Fluor 680) using a confocal fluorescence microscope at 37 °C.

Synthesis of compounds

Compounds **1**–**3** were prepared according to the previously described procedures.[24]

Synthesis of compound 1

o-Aminophenol (4.85 g, 44.5 mmol) and chloroacetic acid (21.0 g, 222 mmol) were added to a three-necked flask, and 2 M NaOH aq. (100 mL) was added to the solution until the pH decreased below 10. The mixture was stirred for 2 h at 100 °C. After cooling, the solvent was evaporated under reduced pressure. The crude mixture of compound **1**, excess NaOH and acetate residues was used in further synthesis without purification.
^{1}H NMR (400 MHz, D_2O) δ 6.79-6.69 (m, 4H), 4.35 (s, 2H), 3.73 (s, 4H).

Synthesis of compound 2

MeOH (120 mL) and H_2SO_4 (8.60 mL, 342 mmol) were added to the crude residue obtained in the preparation of compound **1**, and the mixture was stirred for 3 days at reflux temperature. After cooling, the salts were filtered off and the solvent was evaporated. The residue was dissolved in ethyl acetate and washed with 2 M NaOH aq. and then with brine. After the organic layer was dried over Na_2SO_4 and evaporated under reduced pressure, the residue was purified by flash column chromatography on silica gel (ethyl acetate/hexane = 3:7). Compound **2** (2.11 g, 31%) was obtained as a brown oil.
^{1}H NMR (400 MHz, $CDCl_3$) δ 6.95–6.79 (m, 4H), 4.66 (s, 2H), 4.21 (s, 4H), 3.78 (s, 3H), 3.72 (s, 6H); MS (ESI^+): Calcd for $[M+H]^+$ 326.1162, found 326.0683.

Synthesis of compound 3

Compound **2** (837 mg, 2.57 mmol) was dissolved in AcOH (10 mL), and fuming HNO_3 (160 µL, 3.86 mmol) dissolved in AcOH (1.0 mL) was added in a dropwise manner at 0 °C for over 5 min. After confirming the completion of the reaction, the reaction mixture was poured into ice-water. After extraction with DCM, the organic layer dried over with Na_2SO_4 and filtered. After removing of the solvent under reduced pressure, the residue was purified by column chromatography on silica gel (DCM/MeOH = 99.5:0.5). Compound **3** (738 mg, 77%) was obtained as a yellow solid.

^{1}H NMR (400 MHz, $CDCl_3$) δ 7.86 (dd, *J* = 2.0, 8.8 Hz, 1H), 7.62 (d, *J* = 2.0 Hz, 1H), 6.73 (d, *J* = 8.8 Hz, 1H), 4.68 (s, 2H), 4.28 (s, 4H), 3.82 (s, 3H), 3.78 (s, 6H); MS (ESI^+): Calcd for $[M+H]^+$ 371.1012, found 371.5169.

Synthesis of compound 4

Compound **3** (700 mg) was dissolved in 20 mL of MeOH/H_2O (3:1) and 3 mL of 2 M NaOH aqueous solution was added dropwise at 0 °C. The reaction mixture was then warmed to room temperature. After stirring for 6 h, Dowex-50 H^+ resin was added into the reaction mixture and the pH was adjusted to 5–6, then was filtered off, and the solvent was removed under reduced pressure. Compound **4** (620 mg) was obtained as an orange powder.

Synthesis of compound 5

Compound **4** (620 mg, 1.88 mmol) was dissolved in dry DMF (10.0 mL). Bromomethyl acetate (1.41 mL, 15.0 mmol) and dry TEA (3.15 mL, 22.6mmol) were added at room temperature under Ar. After stirring for 1 day, the solvent was removed under reduced pressure, and DCM was added to the residue, and washed with water. The organic layer was washed with brine, dried with Na_2SO_4 and evaporated. The residue was purified by GPC. Compound **5** (439 mg, 43%) was obtained as a yellow oil.
^{1}H NMR (500 MHz, $CDCl_3$) δ 7.87 (dd, *J* = 9.0, 2.5 Hz, 1H), 7.61 (d, *J* = 2.5 Hz, 1H), 6.74 (d, *J* = 9.0 Hz, 1H), 5.84 (s, 2H), 5.82 (s, 4H), 4.75 (s, 2H), 4.30 (s, 4H), 2.13 (s, 9H); ^{13}C NMR (125 MHz, $CDCl_3$) δ 169.5, 169.2, 166.5, 147.5, 144.9, 141.3, 119.2, 116.9, 108.7, 79.8, 79.4, 65.3, 53.8, 20.7, 20.6; HRMS (FAB^+): Calcd for $[M+H]^+$ 545.1770, found 545.1260.

Synthesis of compound 6

Compound **5** (200 mg, 0.37 mmol) was dissolved in MeOH (20 ml). Pd/C (20%, 18.8 mg) was added and the reaction was stirred for 1 h under H_2. The solution was filtered through a layer celite and evaporated under reduced pressure. Compound **6** (190 mg, quant.) was obtained as a yellow oil.
^{1}H NMR (400 MHz, $CDCl_3$) δ 6.87 (d, *J* = 8.0 Hz), 6.27 (dd, *J* = 8.0, 2.4 Hz, 1H), 6.21 (d, *J* = 2.4 Hz, 1H), 5.82 (s, 2H), 5.74 (s, 4H), 4.70 (s, 2H), 4.13 (s, 4H), 2.11 (s, 3H), 2.08 (s, 6H); ^{13}C NMR (100 MHz, $CDCl_3$) δ 170.0, 169.5, 167.9, 151.7, 143.4, 130.7, 123.5, 109.2, 103.4, 79.3, 79.2, 66.0, 54.0, 20.6; MS (ESI^+): Calcd for $[M+H]^+$ 515.1435, found 514.9805.

Compounds **7**–**9** were prepared according to the previously described procedures.[26]

Synthesis of compound 7

4-Chlororesorcinol (4.89 g, 33.8 mmol) and 4-carboxyphthalic anhydride (3.25 g, 16.9 mmol) were stirred in methanesulfonic acid (40 mL) at 90 °C for 14 h. The reaction mixture was then poured into 400 mL of stirred ice water, and the resulting suspension was filtered The residue was washed with H_2O and dried under vacuum at 90 °C overnight to give a brown solid (7.58 g). The product was carried forward without further purification.

Synthesis of compound 8

The brown solid (7.58 g) was stirred in 25 mL of acetic anhydride and 1.5 mL of pyridine and heated to reflux for 30 min. The reaction mixture was cooled to room temperature for 4 h and then filtered. The filtrate was added slowly into 75 mL of stirred H_2O, and the mixture was stirred for additional 10 min, and then extracted with ethyl acetate. The combined organic layer was washed with 0.4 M HCl aq. and brine, dried with Na_2SO_4, and evaporated to give compound **8** (4.40 g, 49%) as a yellow solid.
^{1}H NMR (500 MHz, CD_3Cl) δ 8.79 (d, *J* = 1.0 Hz, 1H), 8.45 (dd, *J* = 8.0, 1.5 Hz, 1H), 7.33 (d, *J* = 8.0 Hz, 1H), 7.18 (s, 2H), 6.87 (s, 2H), 2.83 (s, 6H); MS (ESI$^+$): Calcd for $[M+H]^+$ 529.0015, found 529.0502.

Synthesis of compound 9

Compound **8** (2.20 g, 4.16 mmol) was dissolved in 24 mL of MeOH/H_2O (3:1). 2 M NaOH aq. (4.5 mL) was added dropwise at 0 °C. The color of the solution changed quickly from yellow to orange. The reaction mixture was warmed at room temperature. After stirring for 2 h, Dowex-50 H^+ resin was added into the reaction mixture and the pH was adjusted to 5–6, then was filtered off, and the solvent was removed under reduced pressure. Compound **9** (1.85 g, quant.) was obtained as an orange powder.
^{1}H NMR (500 MHz, DMSO-*d*$_6$) δ 11.35 (bs, 2H), 8.42 (s, 1H), 8.31 (d, *J* = 8.0 Hz, 1H), 7.43 (d, *J* = 8.0 Hz, 1H), 6.91 (s, 2H), 6.78 (s, 2H); MS (ESI$^-$): Calcd for $[M–H]^-$ 442.9804, found 442.9261.

Synthesis of compound 10

Propargylamine (218 µL, 4.04 mmol) was combined with 37% formaldehyde aqueous solution (253 µL, 3.37 mmol) in 13 mL of acetonitrile under Ar and heated to reflux for 1 h. Compound **9** (1.50 g, 3.37 mmol) dissolved in 28 mL acetonitrile and 28

mL H_2O was added to the reaction solution, and the mixture was refluxed for 3 h. The reaction mixture was cooled, and the solvent was removed under reduced pressure to give compound **10** (1.30 g) as a red solid. The product was carried forward without further purification.
MS (ESI^+): Calcd for $[M+H]^+$ 512.0226, found 511.9580.

Synthesis of compound 11

Compound **10** (1.30 g) was stirred in 20 mL of acetic anhydride, and 800 µL of pyridine, and then heated to reflux for 1 h. After cooling at room temperature for 2 h, the reaction mixture was added slowly to 450 mL of stirred H_2O. After stirred for an additional 10 min, the mixture was extracted with ethyl acetate. The combined organic layer was washed with H_2O, 0.4 M HCl aq. and brine, dried with Na_2SO_4 and evaporated. The residue was purified by column chromatography on silica gel (DCM/MeOH = 99:1). Compound **11** (645 mg, 30%) was obtained as a colorless oil.
^1H NMR (500 MHz, $CDCl_3$) δ 8.80 (d, *J* = 1.0 Hz, 1H), 8.47 (dd, *J* = 8.0, 1.0 Hz, 1H), 7.35 (d, *J* = 8.0 Hz, 1H), 7.28 (s, 1H), 6.87 (s, 1H), 6.86 (s, 1H), 5.12–4.87 (m, 2H), 3.89 (d, *J* = 2.5 Hz, 2H), 2.40 (s, 3H), 2.38 (s, 3H), 2.31 (t, *J* = 2.5 Hz, 1H), 2.25 (s, 3H); ^{13}C NMR (125 MHz, $CDCl_3$) δ 171.4, 168.3, 168.0, 167.9, 167.4, 155.4, 149.3, 148.9, 148.8, 148.7, 137.2, 133.2, 128.6, 128.3, 127.9, 126.2, 124.3, 123.7, 123.3, 120.0, 117.1, 116.8, 113.3, 80.7, 78.0, 72.9, 37.0, 36.9, 21.5, 20.6, 20.5; HRMS (FAB^+): Calcd for $[M+H]^+$ 638.0543, found 638.0616.

Compounds **12** and **13** were prepared according to the previously described procedures.[55]

Synthesis of compound 12

Chromium trioxide (25.0 g, 162 mmol) was dissolved in 300 mL of 1.5 M H_2SO_4 aq., and the solution was cooled to 0 °C. 2-[2-(chloroethoxy)ethoxy]ethanol (8.30 g, 49.2 mmol) in 150 mL of acetone was dropwisely added, and the reaction mixture was stirred at room temperature for 3 h. The solvent was removed under reduced pressure, and the aqueous layer was extracted with DCM. The combined organic layer was washed with brine and dried with Na_2SO_4 and evaporated. Compound **12** (4.89 g, 42%) was obtained as a colorless oil.
^1H NMR (500 MHz, $CDCl_3$) δ 10.21 (bs, 1H), 4.23 (s, 2H), 3.79 (t, *J* = 5.5 Hz, 4H), 3.73 (t, *J* = 5.5 Hz, 2H), 3.65 (t, *J* = 5.5 Hz, 2H); MS (ESI^-): Calcd for $[M–H]^-$ 181.0346, found 180.9873.

Synthesis of compound 13

Compound **12** (3.38 g, 18.5 mmol) and NaN_3 (4.81 g, 74.0 mmol) in 13 mL of H_2O were stirred with heating at 80 °C for 32 h. After cooling to room temperature, the reaction mixture was acidified with 2 M HCl aq. and extracted with DCM. The combined organic layer was dried with Na_2SO_4 and evaporated. Compound **13** (2.39 g, 68%) was obtained as a colorless oil.

^{1}H NMR (500 MHz, $CDCl_3$) δ 9.40 (bs, 1H), 4.22 (s, 2H), 3.79–3.77 (m, 2H), 3.73–3.69 (m, 4H), 3.42 (t, *J* = 5.0 Hz, 2H); MS (ESI$^-$): Calcd for $[M–H]^-$ 188.0750, found 188.3099.

Synthesis of compound 14

Compound **13** (63.4 mg, 0.330 mmol) was dissolved in dry DMF (1 mL). PyBOP (229 mg, 0.44 mmol) and dry TEA (124 µL, 0.88 mmol) were added at room temperature under Ar. After stirring for 30 min, HaloTag® Amine (O2) Ligand (50.0 mg, 0.22 mmol) was added at room temperature. After stirring for 15 h, the solvent was removed under reduced pressure and ethyl acetate was added to the residue, and washed with 10% citric acid and water. The organic layer was washed with brine, dried with Na_2SO_4 and evaporated. The residue was purified by column chromatography on silica gel (DCM/MeOH = 98:2) and subsequently by GPC. Compound **14** (28.0 mg, 32%) was obtained as a colorless oil.

^{1}H NMR (500 MHz, $CDCl_3$) δ 7.28 (s, 1H), 4.01 (s, 2H), 3.70–3.41 (m, 20H), 1.79–1.76 (m, 2H), 1.62–1.59 (m, 2H), 1.46–1.44 (m, 2H), 1.39–1.37 (m, 2H); ^{13}C NMR (125 MHz, $CDCl_3$) δ 169.8, 71.3, 70.9, 70.6, 70.3, 70.1, 70.0, 69.8, 50.6, 45.1, 38.6, 32.5, 29.5, 26.7, 25.4; HRMS (FAB$^+$): Calcd for $[M+H]^+$ 395.1983, found 395.2067.

Synthesis of compound 15

Compound **11** (143 mg, 0.224 mmol) and EEDQ (60.9 mg, 0.246 mmol) were stirred in dry DCM (3 mL) at room temperature for 5 min under Ar. Compound **6** (139 mg, 0.269 mmol) was dissolved in dry DCM (2 mL) and added. The reaction was continued for 19 h, and the solution was evaporated. The residue was purified by column chromatography on silica gel (DCM/MeOH = 99:1). Compound **15** (73.7 mg, 29%) was obtained as a yellow solid.

^{1}H NMR (500 MHz, $CDCl_3$) δ 8.56 (s, 1H), 8.35 (d, *J* = 8.0 Hz, 1H), 8.20 (s, 1H), 7.37 (d, *J* = 8.0 Hz, 1H), 7.28 (s, 1H), 7.28 (s, 1H), 6.89 (d, *J* = 7.0 Hz, 1H), 6.89 (d, *J* = 7.0 Hz, 1H), 6.87 (s, 1H), 6.86 (s, 1H), 5.83 (s, 2H), 5.79 (s, 4H), 5.12–4.87 (m, 2H), 4.74 (s, 2H), 4.26 (s, 4H), 3.89 (d, *J* = 2.5 Hz, 2H), 2.38 (s, 3H),2.31 (s, 3H), 2.31 (t, *J* = 2.5 Hz, 1H), 2.24 (s, 3H), 2.15 (s, 3H), 2.12 (s, 6H); ^{13}C NMR (125 MHz, $CDCl_3$) δ 170.3,170.1,

170.0, 169.6, 168.2, 167.9, 167.5, 167.4, 163.2, 154.0, 149.8, 149.5, 149.0, 148.9, 148.8, 137.9, 135.9, 135.4, 133.0, 128.6, 128.2, 126.4, 124.8, 123.8, 123.7, 123.3, 120.7, 120.4, 116.9, 116.8, 114.4, 113.3, 107.7, 80.9, 79.7, 79.4, 78.3, 72.6, 65.7, 53.5, 36.8, 36.6, 21.7, 20.8, 20.7, 20.6, 20.5; HRMS (FAB^+): Calcd for M^+ 1133.1872, found 1133.1878.

Synthesis of MGH(AM)

Compound **15** (9.71 mg, 8.56 μmol) and compound **14** (4.06 mg, 10.3 μmol) were dissolved in 200 μL of DMF/H_2O (4:1). $CuSO_4$ (1.64 mg, 10.3 μmol) and sodium ascorbate (2.04 mg, 10.3 μmol) were added at room temperature. After stirring for 1.5 h, the solvent was removed under reduced pressure and ethyl acetate was added to the residue, and washed with water. The organic layer was washed with brine, dried with Na_2SO_4 and evaporated. The residue was purified by HPLC. Elution was performed with a 30-minlinear gradient from 55% CH_3CN/0.1% HCOOH to 70% CH_3CN/0.1% HCOOH. MGH(AM) (4.32 mg, 33%) was obtained as a colorless powder.

^1H NMR (500 MHz, Acetone-d_6) δ 9.84 (s, 1H), 8.57 (d, *J* = 1.0 Hz, 1H), 8.42 (dd, *J* = 8.0, 1.0 Hz, 1H), 7.86 (s, 1H), 7.68 (d, *J* = 8.0 Hz, 1H), 7.60 (d, *J* = 2.5 Hz, 1H), 7.45 (dd, *J* = 9.0, 2.5 Hz, 1H), 7.40 (s, 1H), 7.17–7.13 (m, 3H), 6.97 (d, *J* = 9.0 Hz, 1H), 5.84 (s, 2H), 5.77 (s, 4H), 5.11–4.92 (m, 2H), 4.85 (s, 2H), 4.59 (t, *J* = 5.5 Hz, 2H), 4.55 (s, 2H), 4.28 (s, 4H), 3.92 (t, *J* = 5.5 Hz, 2H), 3.84 (s, 2H), 3.64–3.63 (m, 4H), 3.59 (t, *J* = 7.0 Hz, 2H), 3.56–3.48 (m, 6H), 3.41 (t, *J* = 8.0 Hz, 2H), 3.37–3.34 (m, 2H), 2.44–2.28 (m, 9H), 2.08 (s, 3H), 2.06 (s, 6H), 1.78–1.72 (m, 2H), 1.56–1.50 (m, 2H), 1.47–1.41 (m, 2H),1.39–1.34 (m, 2H); ^{13}C NMR (125 MHz, $CDCl_3$) δ 171.8, 171.5, 170.9, 169.7, 169.6, 169.5, 169.4, 169.1, 165.2, 155.9, 151.5, 151.3, 150.8, 150.6, 150.3, 145.5, 139.8, 137.4, 137.0, 135.8, 130.5, 129.6, 128.2, 126.4, 126.1, 124.9, 124.8, 124.4, 123.4, 121.8, 119.4, 119.3, 115.9, 115.3, 109.7, 82.1, 80.9, 80.8, 72.4, 72.3, 72.1, 71.8, 71.7, 71.2, 71.0, 67.2, 55.02, 51.5, 46.7, 44.1, 40.0, 38.3, 34.3, 28.3, 27.1, 23.0, 21.7, 21.5, 21.4; HRMS (FAB^+): Calcd for $[M]^+$ 1527.3855, found 1527.3840.

Synthesis of MGH

MGH(AM) (2.41 mg, 1.58 μmol) was dissolved in MeOH (7 mL). 2 M NaOH aq. (31.2 μL, 63.2 μmol) was added dropwise and stirred at 0 °C for 1 day. Reaction completion was checked by HPLC, then 100 mM HEPES buffer (pH 7.4) with 115 mM KCl and 20 mM NaCl was added to the reaction solution and diluted to a final concentration 3 mM. The stock solution was quickly frozen by liquid nitrogen, and stored below –20 °C.

MS (ESI^-): Calcd for $[M–H]^-$ 1226.3010, found 1226.0365. HPLC chromatogram after

reaction is shown below. Elution was performed with a 15-minlinear gradient from 10% CH_3CN to 90% CH_3CN.

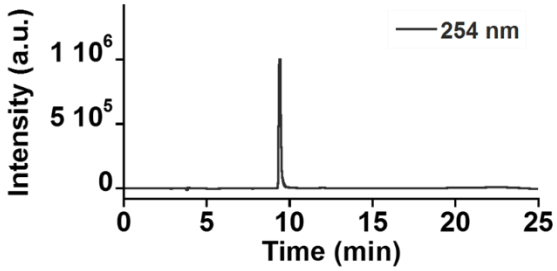

References

1. S. Orrenius, B. Zhivotovsky and P. Nicotera, *Nat. Rev. Mol. Cell Biol*. **2003**, *4*, 552–565.
2. T. Patel, S. F. Bronk and G. J. Gores, *J. Clin. Invest.* **1994**, *94*, 2183–2192.
3. M. M. Chien, K. E. Zahradka, M. K. Newell and J. H. Freed, *J. Biol. Chem.* **1999**, *274*, 7059–7066.
4. G. Zhang, J. J. Gruskos, M. S. Afzal and D. Buccella, *Chem. Sci*. **2015**, *6*, 6841–6846.
5. E. Tomat, E. M. Nolan, J. Jaworski and S. J. Lippard, *J. Am. Chem. Soc*. **2008**, *130*, 15776–15777.
6. M. Bannwarth, I. R. Corrêa Jr., M. Sztretye, S. Pouvreau, C. Fellay, A. Aebischer, L. Royer, E. Ríos and K. Johnsson, *ACS Chem. Biol*. **2009**, *4*, 179–190.
7. M. Kamiya and K. Johnsson, *Anal. Chem*. **2010**, *82*, 6472–6479.
8. D. Srikun, A. E. Albers, C. I. Nam, A. T. Iavarone and C. J. Chang, *J. Am. Chem. Soc*. **2010**, *132*, 4455–4465.
9. M. Abo, R. Minakami, K. Miyano, M. Kamiya, T. Nagano, Y. Urano and H. Sumimoto, *Anal. Chem*. **2014**, *86*, 5983–5990.
10. D. Li, L. Liu and W.-H. Li, *ACS Chem. Biol*. **2015**, *10*, 1054–1063.
11. M. Best, I. Porth, S. Hauke, F. Braun, D.-P. Herten and R. Wombacher, *Org. Biomol. Chem*. **2016**, *14*, 5606–5611.
12. T. Hirata, T. Terai, H. Yamamura, M. Shimonishi, T. Komatsu, K. Hanaoka, T. Ueno, Y. Imaizumi, T. Nagano and Y. Urano, *Anal. Chem*. **2016**, *88*, 2693–2700.
13. J. J. Gruskos, G. Zhang and D. Buccella, *J. Am. Chem. Soc.* **2016**, *138*, 14639–14649.
14. T. Fujii, Y. Shindo, K. Hotta, D. Citterio, S. Nishiyama, K. Suzuki and K. Oka, *J. Am. Chem. Soc*. **2014**, *136*, 2374–2381.
15. Y. Suzuki, H. Komatsu, T. Ikeda, N. Saito, S. Araki, D. Citterio, H. Hisamoto, Y. Kitamura, T. Kubota, J. Nakagawa, K. Oka and K. Suzuki, *Anal. Chem*. **2002**, *74*, 1423–1428.

16. H. Komatsu, N. Iwasawa, D. Citterio, Y. Suzuki, T. Kubota, K. Tokuno, Y. Kitamura, K. Oka and K. Suzuki, *J. Am. Chem. Soc.* **2004**, *126*, 16353–16360.
17. Y. Shindo, T. Fujii, H. Komatsu, D. Citterio, K. Hotta, K. Suzuki and K. Oka, *PLoS One* **2011**, *6*, e23684.
18. B. A. Griffin, S. R. Adams and R. Y. Tsien, *Science* **1998**, *281*, 269–272.
19. G. V. Los, L. Encell, M. McDougall, D. Hartzell, N. Karassina, C. Zimprich, M. Wood, R. Learish, R. Ohana, M. Urh, D. Simpson, J. Mendez, K. Zimmerman, P. Otto, G. Vidugiris, J. Zhu, A. Darzins, D. Klaubert, R. Bulleit and K. Wood, *ACS Chem. Biol.* **2008**, *3*, 373–382.
20. H. Szmacinski and J. R. Lakowicz, *J. Fluoresc.* **1996**, *6*, 83–95.
21. T. Ueno, Y. Urano, K. Setsukinai, H. Takakusa, H. Kojima, K. Kikuchi, K. Ohkubo, S. Fukuzumi and T. Nagano, *J. Am. Chem. Soc.* **2004**, *126*, 14079–14085.
22. T. Miura, Y. Urano, K. Tanaka, T. Nagano, K. Ohkubo and S. Fukuzumi, *J. Am. Chem. Soc.* **2003**, *125*, 8666–8671.
23. H. Kobayashi, M. Ogawa, R. Alford, P. L. Choyke and Y. Urano, *Chem. Rev.* **2010**, *110*, 2620–2640.
24. B. Metten, M. Smet, N. Boens and W. Dehaen, *Synthesis* **2005**, *11*, 1838–1844.
25. R. Y. Tsien, *Nature* **1981**, *290*, 527–528.
26. C. C. Woodroofe, R. Masalha, K. R. Barnes, C. J. Frederickson and S. J. Lippard, *Chem. Bio.* **2004**, *11*, 1659–1666.
27. R. P. Haugland, *Handbook of Fluorescent Probes and Research Products. 9th ed.*, Molecular Probes Inc., Eugene, Oregon, **2002**.
28. D. E. Clapham, *Cell* **2007**, *131*, 1047–1058.
29. D. Kalderon, B. L. Roberts, W. D. Richardson and A. E. Smith, *Cell* **1984**, *39*, 499–509.
30. M. D. Resh, *Cell* **1994**, *76*, 411–413.
31. T. Inoue, W. D. Heo, J. S. Grimley, T. J. Wandless and T. Meyer, *Nat. Methods* **2005**, *2*, 415–418.
32. L. Filippin, M. C. Abad, S. Gastaldello, P. J. Magalhães, D. Sandonà and T. Pozzan, *Cell Calcium* **2005**, *37*, 129–136.
33. F. Di Virgilio, T. H. Steinberg, J. A. Swanson and S. C. Silverstein, *J. Immunol.* **1988**, *140*, 915–920.
34. M. Mitsui, A. Abe, M. Tajimi and H. Karaki, *Jpn. J. Pharmacol.* **1993**, *61*, 165–170.
35. D. Yamazaki, Y. Funato, J. Miura, S. Sato, S. Toyosawa, K. Furutani, Y. Kurachi, Y. Omori, T. Furukawa, T. Tsuda, S. Kuwabata, S. Mizukami, K. Kikuchi and H. Miki, *PLoS Genet.* **2013**, *9*, e1003983.

36. D. Boehning, R. L. Patterson, L. Sedaghat, N. O. Glebova, T. Kurosaki and S. H. Snyder, *Nat. Cell Biol*. **2003**, *5*, 1051–1061.
37. Y. Zhao, S. Araki, J. Wu, T. Teramoto, Y.-F. Chang, M. Nakano, A. S. Abdelfattah, M. Fujiwara, T. Ishihara, T. Nagai and R. E. Campbell, *Science* **2011**, *333*, 1888–1891.
38. V. A. Patel, A. Longacre, K. Hsiao, H. Fan, F. Meng, J. E. Mitchell, J. Rauch, D. S. Ucker and J. S. Levine, *J. Biol. Chem*. **2006**, *281*, 4663–4670.
39. A. M. Romani, *Arch. Biochem. Biophys*. **2011**, *512*, 1–23.
40. A. W. Harman, A. L. Nieminen, J. J. Lemasters and B. Herman, *Biochem. Biophys. Res. Commun*. **1990**, *170*, 477–483.
41. V. Gaussin, P. Gailly, J. M. Gillis and L. Hue, *Biochem. J.* **1997**, *326*, 823–827.
42. A. Gasbarrini, A. B. Borle, H. Farghali, C. Bender, A. Francavilla and D. Van Thiel, *J. Biol. Chem*. **1992**, *267*, 6654–6663.
43. F. B. Chekeni, M. R. Elliott, J. K. Sandilos, S. F. Walk, J. M. Kinchen, E. R. Lazarowski, A. J. Armstrong, S. Penuela, D. W. Laird, G. S. Salvesen, B. E. Isakson, D. A. Bayliss and K. S. Ravichandran, *Nature* **2010**, *467*, 863–869.
44. H. Imamura, unpublished work.
45. H. Imamura, K. P. Huynh Nhat, H. Togawa, K. Saito, R. Iino, Y. Kato-Yamada, T. Nagai and H. Noji, *Proc. Natl. Acad. Sci. USA* **2009**, *106*, 15651–15656.
46. W. Silverman, S. Locovei and G. Dahl, *Am. J. Physiol. Cell Physiol*. **2008**, *295*, C761–C767.
47. P. Widlak, P. Li, X. Wang and W. T. Garrard, *J. Biol. Chem*. **2000**, *275*, 8226–8232.
48. F.-Y. Li, B. Chaigne-Delalande, C. Kanellopoulou, J. C. Davis, H. F. Matthews, D. C. Douek, J. I. Cohen, G. Uzel, H. C. Su and M. J. Lenardo, *Nature* **2011**, *475*, 471–476.
49. C. C. Woodroofe, A. C. Won and S. J. Lippard, *Inorg Chem*. **2005**, *44*, 3112–3120.
50. T. W. Traut, *Mo. Cell. Biochem*. **1994**, *140*, 1-22.
51. T. Yoshida, A. Kakizuka and H. Imamura, *Sci. Rep*. **2016**, *6*, 39618.
52. M. Leist, B. Single, A. F. Castoldi, S. Kühnle and P. Nicotera, *J. Exp. Med*. **1997**, *185*, 1481–1486.
53. S. Watanabe, S. Mizukami, Y. Akimoto, Y. Hori and K. Kikuchi, *Chem. Eur. J*. **2011**, *17*, 8342–8349.
54. Y. Hori S. Hirayama, M. Sato and K. Kikuchi, *Angew. Chem. Int. Ed.* **2015**, *54*, 14368–14371.
55. X. Chen, S. McRae, S. Parelkar and T. Emrick, *Bioconjugate Chem*. **2009**, *20*, 2331–2341.

Chapter 2

Highly Selective Tridentate Fluorescent Probes for Visualizing Intracellular Mg^{2+} Dynamics without Interference from Ca^{2+} Fluctuation

Chem. Commun. **2017**, *53*, 10644–10647.

Introduction

In order to investigate Mg^{2+}-related biology in detail, the development of highly selective Mg^{2+} probes has been of great interest. However, despite the significance and high demand, highly selective Mg^{2+} probes have been underdeveloped for decades. Commercially available fluorescent Mg^{2+} probes based on APTRA show higher affinities for Ca^{2+} (K_d (Mg^{2+}) = 1–4.7 mM, K_d (Ca^{2+}) = 6–35 μM). Although $[Ca^{2+}]_i$ ranges between 10 nM and 1 μM, some organelles such as the ER, mitochondria, and Golgi apparatus contain high concentrations of Ca^{2+} (hundreds of μM), and APTRA-based Mg^{2+} probes are unable to exclusively detect Mg^{2+} for dynamic monitoring. The KMG series, based on β-diketone with a bidentate coordination site,[1,2] have been reported as selective Mg^{2+} probes that show a low affinity for Ca^{2+} with millimolar range dissociation constants. However, it is difficult for the bidentate ligand to distinguish free Mg^{2+} from the Mg-ATP complex, which is the most abundant form of Mg^{2+} in living cells.[3] Diaza-18-crown-6-hydroxyquinoline (DCHQ1) can also selectively bind to intracellular Mg^{2+} and image total intracellular Mg^{2+} due to its high affinity for Mg^{2+}.[4] However, part of the multidentate metal ligand is integrated in the fluorophore, making functional extension quite difficult. For example, inherent limitations such as short wavelength excitation and intracellular localization problems have not improved.[5] Therefore, for the elucidation of detailed Mg^{2+} dynamics in cells, development of novel design principle and selective probes for intracellular free Mg^{2+} have been eagerly anticipated. In this chapter, the author developed novel Mg^{2+}-selective fluorescent probes with a tridentate Mg^{2+} chelator designed by adjusting the rigid cavity size of the chelator moiety. The new probes demonstrated selective visualization of $[Mg^{2+}]_i$ changes without interference from intracellular Ca^{2+} fluctuation.

Design of novel Mg^{2+}-selective chelators

For the design of a novel Mg^{2+}-selective chelator, the author focused on the differences in the coordination properties of Mg^{2+} and Ca^{2+} complexes. Mg^{2+} invariably forms hexacoordinate complexes, while Ca^{2+} adopts 6–8 coordinate bonding arrangements.[6] The distance between Mg^{2+} and the ligand atoms ranges from 2.05 to 2.25 Å, whereas for Ca^{2+}, the distance varies between 2.2 and 2.7 Å.[6] These distinct differences suggest that Mg^{2+} forms a more rigid complex, whereas Ca^{2+} complexes exhibit more flexibility. For a Mg^{2+}-selective chelator, the author conceived of a new design principle that rigid chelators would possibly show stronger affinity for Mg^{2+} over Ca^{2+}. Moreover, a recent study suggested the importance of low denticity for Mg^{2+}-selective chelators.[7] On the basis of these design principles, the author synthesized several rigid Mg^{2+} chelators (Figure 2-1 and Supplementary Figures). Among them, a tridentate iminocoumarin-based chelator (compound A) recognized Mg^{2+} without response to Ca^{2+} interference (Figure 2-1a). Since $[Mg^{2+}]_i$ is estimated to be in the rage of 0.5–1 mM, the ideal K_d value for Mg^{2+} should be around 1 mM.[8] However, the affinity of compound A for Mg^{2+} was too weak to calculate the K_d for Mg^{2+}. Then, the author modified the ligand structure to enhance the affinity for Mg^{2+} by increasing the denticity. However, this approach improved the affinity not only for Mg^{2+}, but also for Ca^{2+} (compound B and compound C in Figures 2-1b and c). Then, the author adopted another approach to make the chelator structure of compound A more rigid. The new ligand, 2,8-dicarboxyquinoline (DCQ), showed a large blue shift in the absorption spectra upon addition of 0.1 mM Mg^{2+} which indicated the adequate affinity for Mg^{2+} (Figure 2-1d). On the other hand, addition of Ca^{2+} barely shifted the absorption maximum wavelength. This result suggested that DCQ had the potential to be a suitable chelator for a selective Mg^{2+} probes.

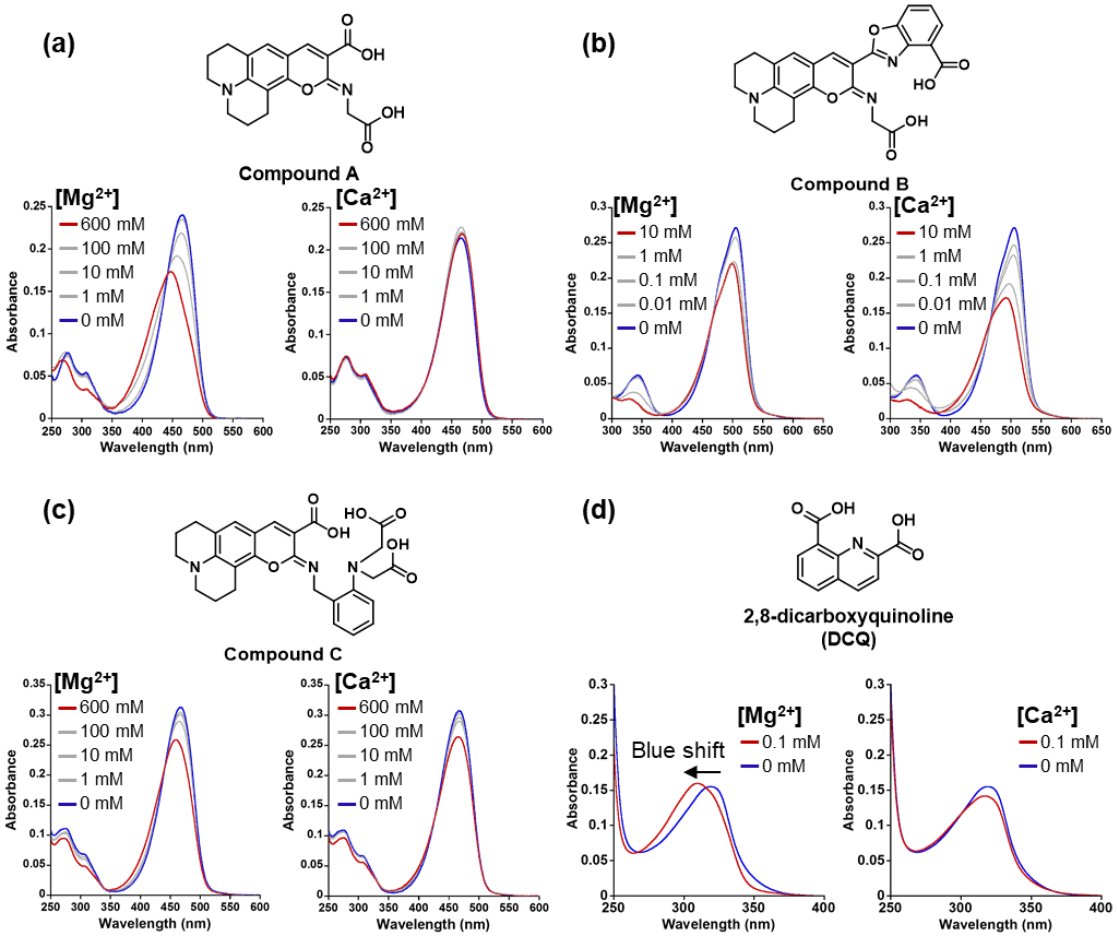

Figure 2-1. UV-vis absorption spectra of (a) 10 μM compound A, (b) 5 μM compound B, (c) 10 μM compound C and (d) 10 μM 2,8-dicarboxyquinoline in the presence and absence of Mg^{2+} or Ca^{2+} in 100 mM HEPES buffer (pH 7.4) at 37 °C.

Synthesis and optical properties of Mg^{2+}-selective fluorescent probes

DCQ was attached to the 9'-position of a 2,7-dichloro-6-hydroxyxanthen-3-one skeleton for the development of a Mg^{2+}-selective fluorescent probe. MGQ-1 was designed to demonstrate Mg^{2+}-sensing based on a photo-induced electron transfer (PeT) mechanism, since the coordination of Mg^{2+} changes the HOMO and LUMO energy levels of the DCQ moiety.[9] MGQ-1 was synthesized according to Scheme 2-1.

Scheme 2-1

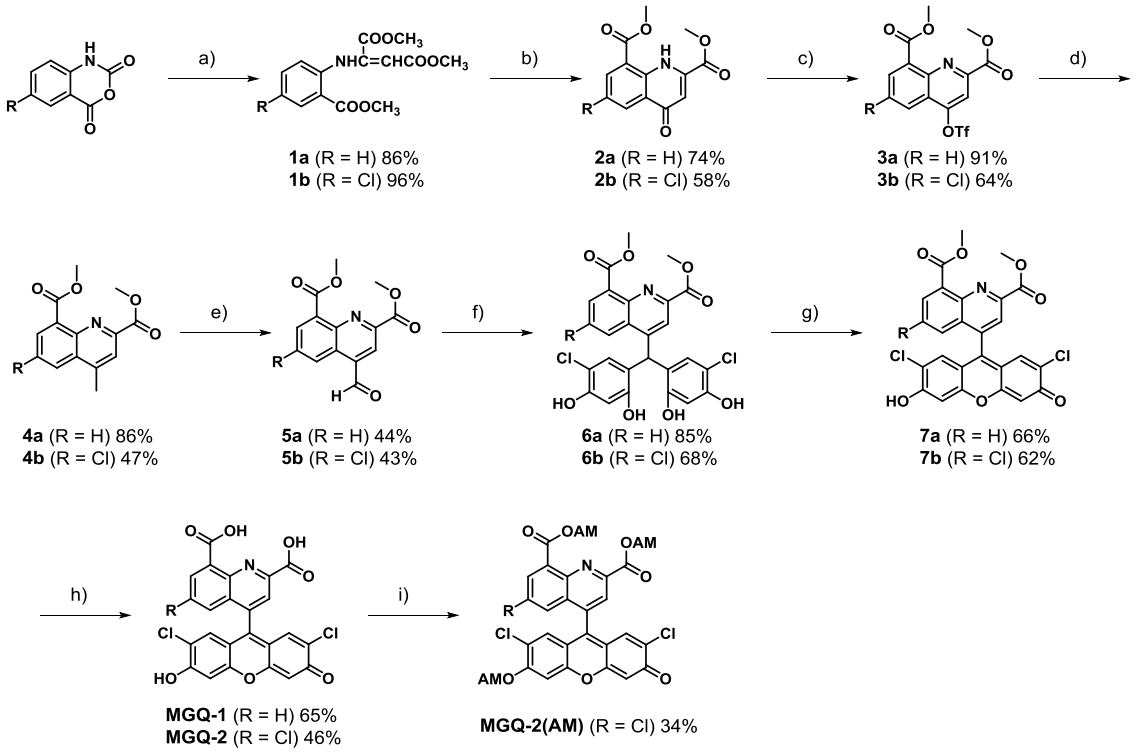

a) dimethyl acetylenedicarboxylate, sodium methoxide, MeOH, reflux; b) diphenyl ether, reflux; c) trifluoromethanesulfonic anhydride, 2,6-lutidine, DMAP, DCM, 0 °C→r.t.; d) methylboronic acid, K_2CO_3, Pd(dppf)Cl_2·CH_2Cl_2, dioxane, 100 °C; e) SeO_2, dioxane, 80 °C; f) 4-chlororesorcinol, 8% (v/v) $MeSO_3H$, DCM/Et_2O (1:1), r.t.; g) *p*-TsOH·H_2O, AcOH, 60 °C; h) 2 M NaOH aq., MeOH/H_2O (3:1), r.t.; i) bromomethyl acetate, DIEA, DMF, r.t.

Although the absorption spectra of MGQ-1 showed little change with 100 mM Mg^{2+} (Figure 2-2a), the fluorescence intensity considerably decreased as Mg^{2+} concentration was increased (Φ_{free} = 0.36, Φ_{bound} < 0.01) (Figure 2-2a and Table 2-1). This turn-off response was attributed to the suppression of the fluorescence by the donor-excited PeT (d-PeT).[10] The HOMO and LUMO energy levels of DCQ are lower than APTRA and the formation of Mg^{2+} complex stabilizes the LUMO and HOMO levels of the Mg^{2+} chelator (Figure 2-3). In the calculation, the protonated form of the DCQ was used to evaluate the orbital energy changes instead of the Mg^{2+}-bound form (Figure 2-3a). The K_d of MGQ-1 for Mg^{2+} was calculated to be 0.14 mM, which was a suitable K_d to detect change in $[Mg^{2+}]_i$ (Figure 2-2b). Importantly, the affinity for Ca^{2+} (K_d (Ca^{2+}) = 1.0 mM) was much weaker than that of the widely used APTRA-based Mg^{2+} probes (K_d (Ca^{2+}) = 6–35 μM). This K_d value indicated that MGQ-1 would not respond to $[Ca^{2+}]_i$ changes over its hysiological range during various cellular events.[11]

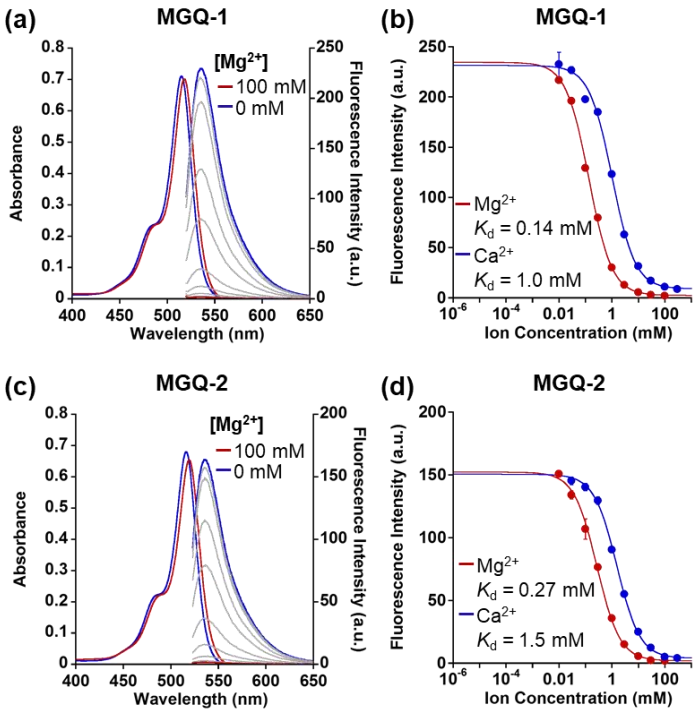

Figure 2-2. (a) Absorption and emission spectra of MGQ-1 at different Mg^{2+} concentrations. Absorption spectra of 10 μM MGQ-1 were measured in the presence or absence of 100 mM Mg^{2+} (100 mM HEPES buffer, 115 mM KCl, 20 mM NaCl, pH 7.4, 37 °C). Emission spectra of 1 μM MGQ-1 were measured in a buffer (100 mM HEPES, 115 mM KCl, 20 mM NaCl, pH 7.4, 37 °C). [Mg^{2+}] = 0, 0.01, 0.03, 0.1, 0.3, 1, 3, 10, 30, 100 mM. λ_{ex} = 515 nm. (b) Mg^{2+}- and Ca^{2+}-titration curves of MGQ-1 emission at 536 nm (λ_{ex} = 515 nm). The error bars denote SD (n = 3). (c) Absorption and emission spectra of MGQ-2 under the same conditions as in (a). (d) Mg^{2+}- and Ca^{2+}-titration curves of MGQ-2 emission at 536 nm (λ_{ex} = 515 nm). The error bars denote SD (n = 3).

Table 2-1. Spectroscopic properties of MGQ-1 and MGQ-2[a]

	λ_{abs}/nm	λ_{em}/nm	ε/cm^{-1} M^{-1}	Φ_{free}[b] (Φ_{bound})	K_d (Mg^{2+}) /mM	K_d (Ca^{2+}) /mM
MGQ-1	515	536	71,000	0.36 (<0.01)	0.14	1.0
MGQ-2	516	536	69,000	0.33 (<0.01)	0.27	1.5

[a] Measured at 37 °C in 100 mM HEPES buffer (pH 7.4) with 115 mM KCl and 20 mM NaCl.

[b] Relative fluorescence quantum yield determined by using fluorescein (Φ = 0.85 in 0.1 M NaOH aq.) as a standard. Φ_{free} and Φ_{bound} denote the relative fluorescent quantum yield in the absence and presence of 100 mM Mg^{2+}, respectively.

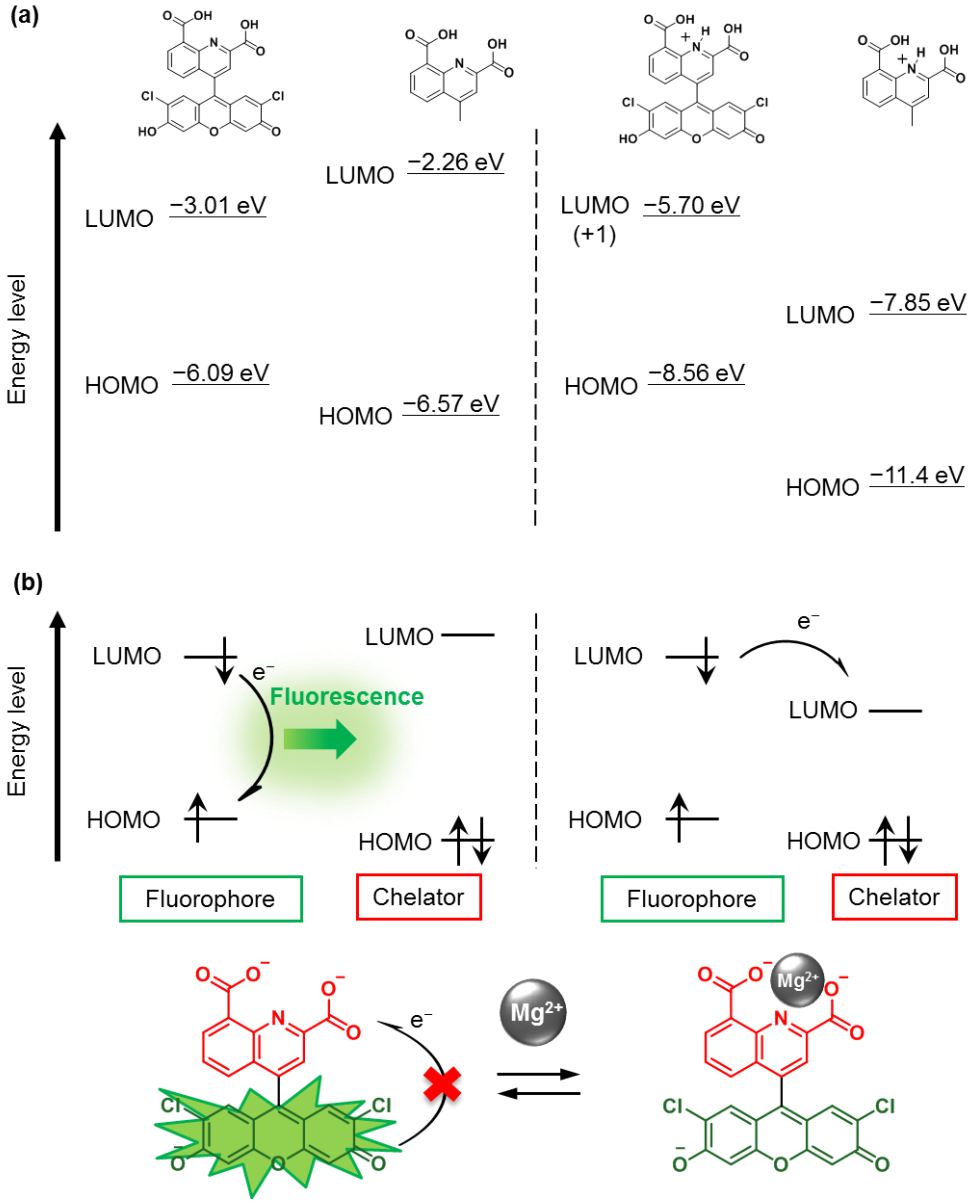

Figure 2-3. (a) Quantum chemical calculation of HOMO and LUMO energy levels of MGQ-1 and protonated MGQ-1 in water (B3LYP/6-31G(d)). (b) Turn-off mechanism of MGQ-1 caused by d-PeT.

However, the fluorescence intensity of MGQ-1 was affected by pH changes over a neutral pH range (pH 6–8) due to d-PeT caused by protonation of the quinoline moiety (Figure 2-4a). To decrease the pK_a of MGQ-1, an electron-withdrawing chloro group was introduced into the 6-position of the DCQ moiety and MGQ-2 was synthesized (Scheme 2-1). As expected, MGQ-2 showed almost no fluorescence response to pH fluctuation in the neutral pH range (pH 7–8) (Figure 2-4a). Moreover, introduction of a chlorine atom resulted in the further improvement of K_d values for both Mg^{2+} (0.27 mM) and Ca^{2+} (1.5

mM) (Figures 2-2c and d). Overall, MGQ-2 exhibited superior optical properties for visualizing $[Mg^{2+}]_i$ changes compared with MGQ-1. Then, the author evaluated the metal ion selectivity of MGQ-2 with other biologically-relevant metal ions (Figure 2-4d). MGQ-2 bound Zn^{2+} with a K_d of 540 nM (Figure 2-4c). However, this value was much weaker than the affinity for Zn^{2+} (K_d (Zn^{2+}) = 3 nM) of Fura-2, a widely used Ca^{2+} fluorescent probe.[12] Although MGQ-2 also showed some responses to other metal ions such as Cu^{2+} and Co^{2+} (Fig. S4c), the concentrations of these ions are maintained at very low level in cells.[13] Therefore, these ions are unlikely to interfere with Mg^{2+} sensing by MGQ-2 in typical cell samples. Through the photobleaching experiment with a Xe light source, MGQ-2 showed higher photostability than fluorescein although the fluorescence intensity decreased slightly during long-term irradiation (Figure 2-4e).

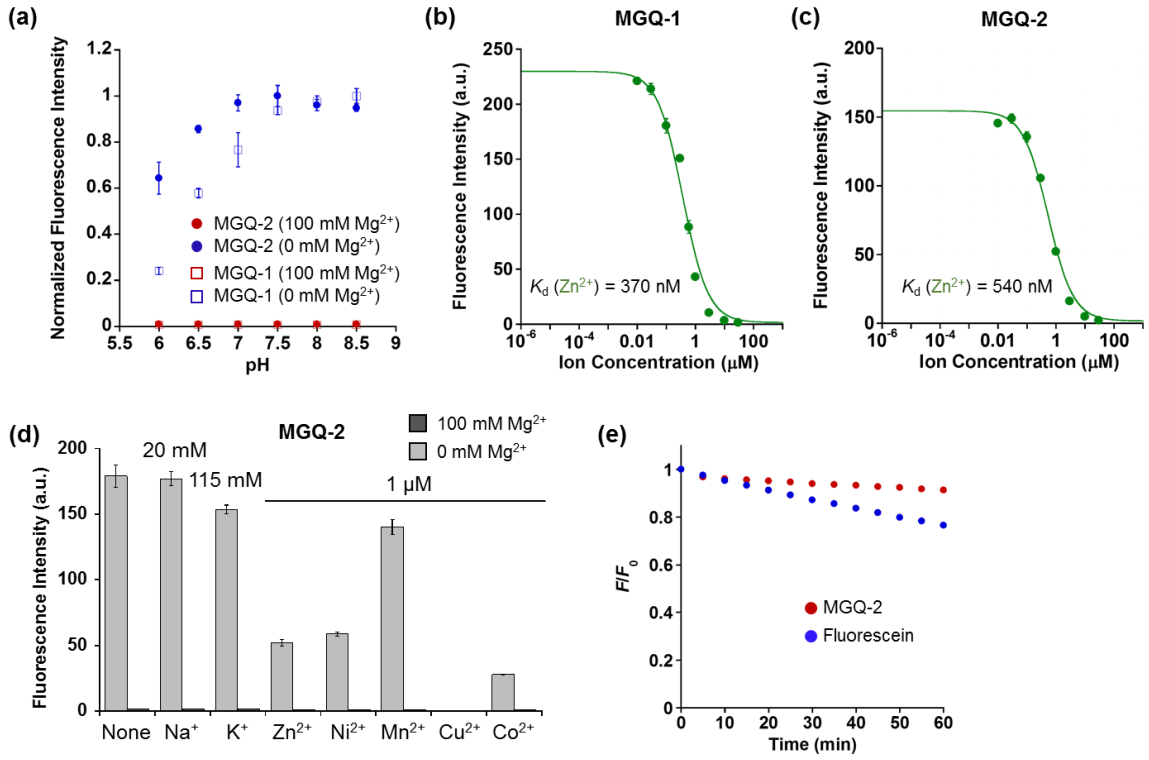

Figure 2-4. (a) Effect of the pH on the fluorescence intensity of MGQ-1 and MGQ-2 in the pH region of 6.0–6.5 (in 100 mM MES buffer, 115 mM KCl, 20 mM NaCl) and 7.0–8.5 (in 100 mM HEPES buffer, 115 mM KCl, 20 mM NaCl), with or without 100 mM of Mg^{2+}. The error bars denote SD (n = 3). (b, c) Zn^{2+}-titration curves of (b) MGQ-1 and (c) MGQ-2 measured from their emissions at 536 nm (100 mM HEPES buffer, 115 mM KCl, 20 mM NaCl, pH 7.4, 37 °C). $[Zn^{2+}]$ = 0, 0.01, 0.03, 0.1, 0.3, 0.6, 1, 3, 10, 30 μM. λ_{ex} = 515 nm. (d) Metal ion selectivity of 1 μM MGQ-2 in the presence and absence of 100 mM Mg^{2+}. Na^+ was added at 20 mM, and K^+ was added at 115 mM (100 mM HEPES buffer, pH 7.4, 37 °C). Zn^{2+}, Ni^{2+}, Mn^{2+}, Cu^{2+} or Co^{2+} were added to a final concentration of 1 μM (100 mM HEPES buffer, 115 mM KCl, 20 mM NaCl, pH 7.4, 37 °C). The error bars denote SD (n = 3). (e) Photostability of MGQ-2 during continuous irradiation (4.0 mW/cm^2). Changes in the fluorescence intensity (F) were normalized by the initial fluorescence intensity (F_0). The error bars denote SD (n = 3).

Next, the response of MGQ-2 to Mg-ATP was evaluated, because bidentate *β*-diketone-based probes such as the KMG series do not adequately distinguish free Mg^{2+} from the ATP-bound form.[3] Addition of 0.3–10 mM Mg^{2+} as a 1:1 complex with ATP to tridentate MGQ-2 showed a similar absorption wavelength shift as the addition of 0.3–10 mM free Mg^{2+} (Figures 2-5a, b and c). The fluorescence intensity of MGQ-2 significantly decreased as the Mg-ATP concentration was increased, where apparent dissociation constant $K_{d,app}$ for Mg-ATP was 0.92 mM (Figures 2-5e and f). However, the fluorescence intensity recovered in the presence of excess ATP (Figure 2-5g). These results strongly indicate that MGQ-2 binds to free Mg^{2+} by competing with ATP at less than a 10 mM concentration of Mg-ATP. However, addition of 30 mM Mg-ATP resulted in a large decrease of the absorbance with a slight wavelength shift, which indicates the formation of a MGQ-2-Mg-ATP ternary complex in the presence of such highly concentrated Mg-ATP (Figures 2-5c and d). The concentration of ATP in living cells is on the order of several mM.[14] Therefore, these results indicate that the tridentate probe MGQ-2 can discriminately detect free Mg^{2+} under physiological conditions, although it binds Mg^{2+} competitively with ATP due to its relatively small K_d.

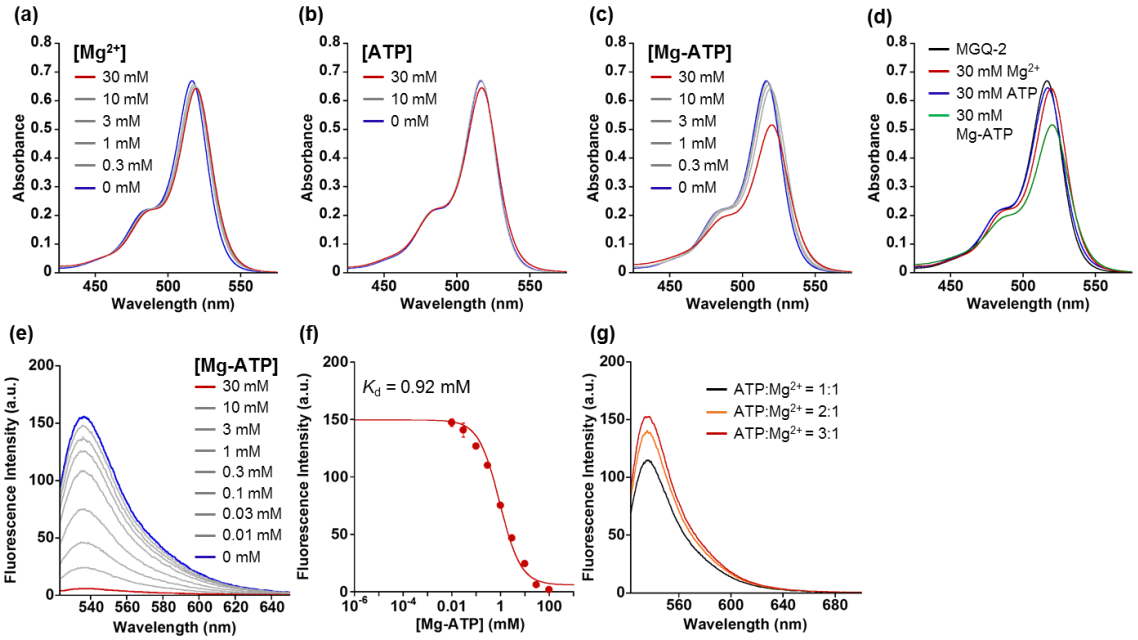

Figure 2-5. UV-vis spectra of 10 µM MGQ-2 in the presence of (a) Mg^{2+}, (b) ATP, or (c) Mg-ATP (100 mM HEPES, 115 mM KCl, 20 mM NaCl, pH 7.4, 37 °C). [Mg^{2+}] or [Mg-ATP] = 0, 0.3, 1, 3, 10, 30 mM. [ATP] = 0, 10, 30 mM. (d) UV-vis spectra of 10 µM MGQ-2 in the presence of 30 mM Mg^{2+}, ATP or Mg-ATP. (e) Emission spectra of 1 µM MGQ-2 in the presence of Mg-ATP (100 mM HEPES, 115 mM KCl, 20 mM NaCl, pH 7.4, 37 °C). [Mg-ATP] = 0, 0.01, 0.03, 0.1, 0.3, 1, 3, 10, 30 mM. λ_{ex} = 515 nm. (f) Mg-ATP-titration curve of MGQ-2 measured from its emission at 536 nm. The error bars denote SD (n = 3). (g) Emission spectra of 1 µM MGQ-2 in the presence of different ratios of ATP to Mg^{2+}. Black line; 0.3 mM ATP and 0.3 mM Mg^{2+}. Orange line; 0.6 mM ATP and 0.3 mM Mg^{2+}. Red line; 0.9 mM ATP and 0.3 mM Mg^{2+}.

Detection of Mg^{2+} extrusion through CNNM4

For live-cell imaging applications, MGQ-2 was derivatized to the acetoxymethyl (AM) form, MGQ-2(AM), to enhance its cell membrane permeability (Scheme 2-1). After penetration into the cells, the AM esters are quickly cleaved by intracellular esterases, and the Mg^{2+}-sensitivity is recovered. The intracellular distribution of MGQ-2 in HEK293 cells was confirmed through spinning-disk confocal fluorescence microscopy. The fluorescence of MGQ-2 was observed throughout the entire cell, although it seemed to localize mainly in the nuclei (Figure 2-6a). To examine the response of MGQ-2 to Mg^{2+} in living cells, the author performed Mg^{2+} export experiments by using a Mg^{2+} transporter, ancient conserved domain protein/cyclin M4 (CNNM4).[15] HEK293 cells transiently expressing CNNM4 were incubated with MGQ-2(AM) in 40 mM Mg^{2+} buffer. After 45 min, the extracellular solution was exchanged with a 0 mM Mg^{2+} buffer to artificially promote Mg^{2+} export via CNNM4. The fluorescence intensity of MGQ-2 quickly increased after the Mg^{2+} release from the cytosol to the extracellular medium (Figures 2-6b and c), demonstrating the inverse response of the fluorescence intensity of MGQ-2 to a decrease in $[Mg^{2+}]_i$.

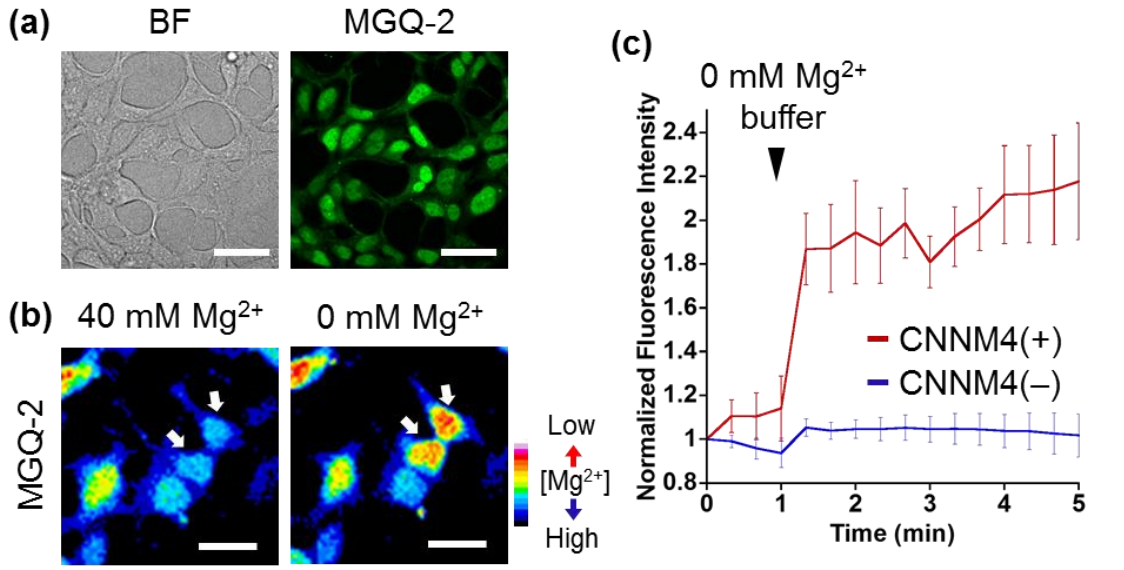

Figure 2-6. (a) Intracellular distribution of MGQ-2 in HEK293 cells. HEK293 cells were incubated with 2 µM MGQ-2(AM) for 45 min at 37 °C. Scale bar: 40 µm. (b) Confocal fluorescence microscopic images of Mg^{2+} export with MGQ-2. HEK293 cells transfected with CNNM4-FLAG were incubated with Mg^{2+}-loading buffer (78.1 mM NaCl, 5.4 mM KCl, 1.8 mM $CaCl_2$, 40 mM $MgCl_2$, 5.5 mM glucose, 5.5 mM HEPES-KOH, pH 7.4), including 2 µM MGQ-2(AM), for 45 min at 37 °C. These cells were subjected to Mg^{2+} depletion 1 min after the imaging started. Scale bar: 20 µm. (c) The relative fluorescence intensity of MGQ-2 was presented as line plots. The error bars denote SD (n = 5).

Responsivity of MGQ-2 toward increase in $[Ca^{2+}]_i$

The author confirmed that MGQ-2 does not respond to $[Ca^{2+}]_i$ changes in living cells. HEK293 cells expressing a genetically-encoded Ca^{2+} specific fluorescent probe, R-GECO, which increases red fluorescence intensity in response to $[Ca^{2+}]_i$,[16] were incubated with MGQ-2(AM) or a commercially available Mg^{2+} probe, Magnesium Green(AM), for 45 min. After washing the cells with Mg^{2+}- and Ca^{2+}-free HEPES-buffered Hanks' balanced salt solution (HHBSS), 10 mM Ca^{2+} in Mg^{2+}-free HHBSS was added to the cells. Then, 5 μM ionomycin, which is a Ca^{2+} ionophore, was added after 1 min to introduce Ca^{2+} into the cells. A large increase in the fluorescence intensity of R-GECO, which indicates $[Ca^{2+}]_i$ increase, was observed after the addition of ionomycin (Figure 2-7). As for the Mg^{2+} probes, although the fluorescence signal of Magnesium Green considerably increased in response to the Ca^{2+} influx, the fluorescence intensity of MGQ-2 remained constant. This result clearly shows that MGQ-2 is superior for the exclusive detection of $[Mg^{2+}]_i$ change without interference from Ca^{2+} fluctuations when compared to standard APTRA-based Mg^{2+} probes.

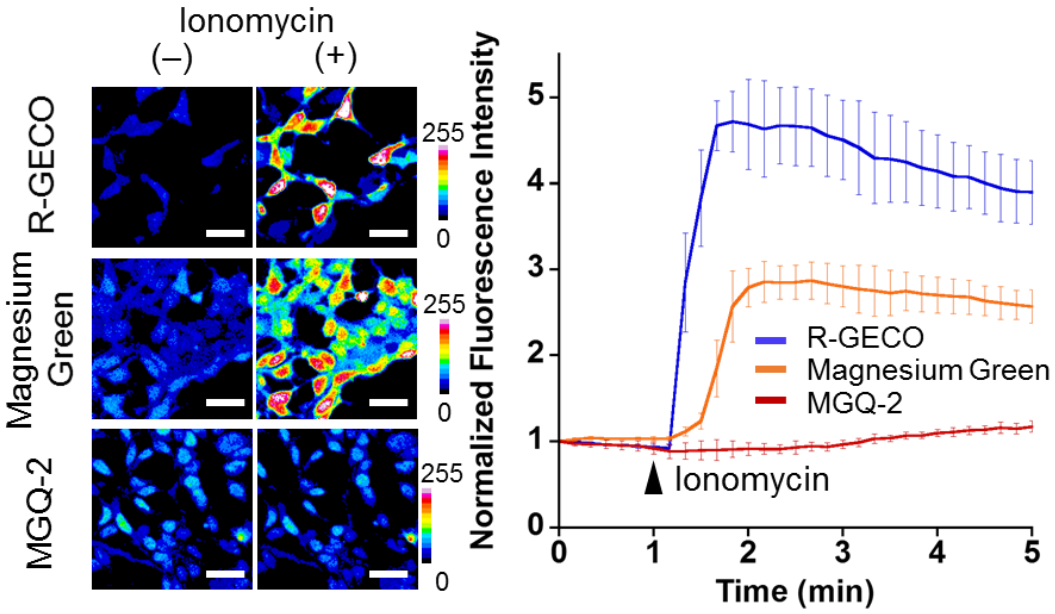

Figure 2-7. Ca^{2+} responsivity of MGQ-2 in HEK293 cells. HEK293 cells expressing R-GECO were loaded with 2 μM MGQ-2(AM) or Magnesium Green(AM) for 45 min at 37 °C. After washing with Mg^{2+}- and Ca^{2+}-free HHBSS, 10 mM Ca^{2+} in Mg^{2+}-free HHBSS was added to the cells. Then, 5 μM ionomycin, a Ca^{2+} ionoophore, was added at the indicated time point (arrow). Scale bar: 40 μm. The error bars denote SD (n = 5).

Supplementary Figures

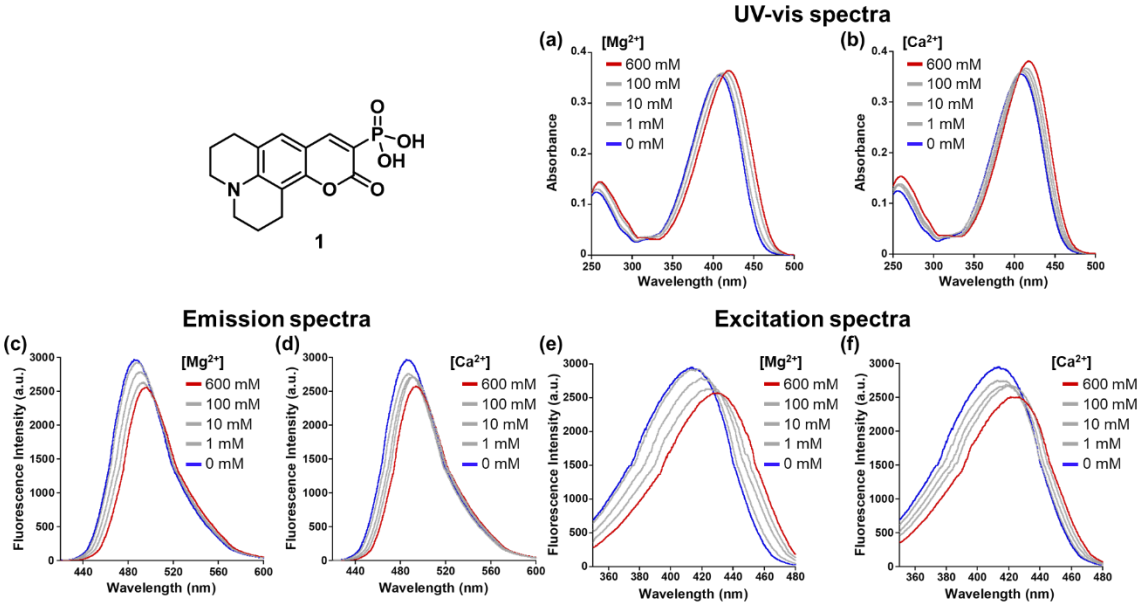

Figure S2-1. (a, b) Absorption spectra of 10 μM compound **1** in 100 mM HEPES buffer (pH 7.4). (a) $[Mg^{2+}]$ = 0, 1, 10, 100, 600 mM. (b) $[Ca^{2+}]$ = 0, 1, 10, 100, 600 mM. (c, d) Emission spectra of 10 μM compound **1** in 100 mM HEPES buffer (pH 7.4) (λ_{ex} = 412 nm). (c) $[Mg^{2+}]$ = 0, 1, 10, 100, 600 mM. (d) $[Ca^{2+}]$ = 0, 1, 10, 100, 600 mM. (e, f) Excitation spectra of 10 μM compound **1** in 100 mM HEPES buffer (pH 7.4) (λ_{em} = 485 nm). (e) $[Mg^{2+}]$ = 0, 1, 10, 100, 600 mM. (f) $[Ca^{2+}]$ = 0, 1, 10, 100, 600 mM.

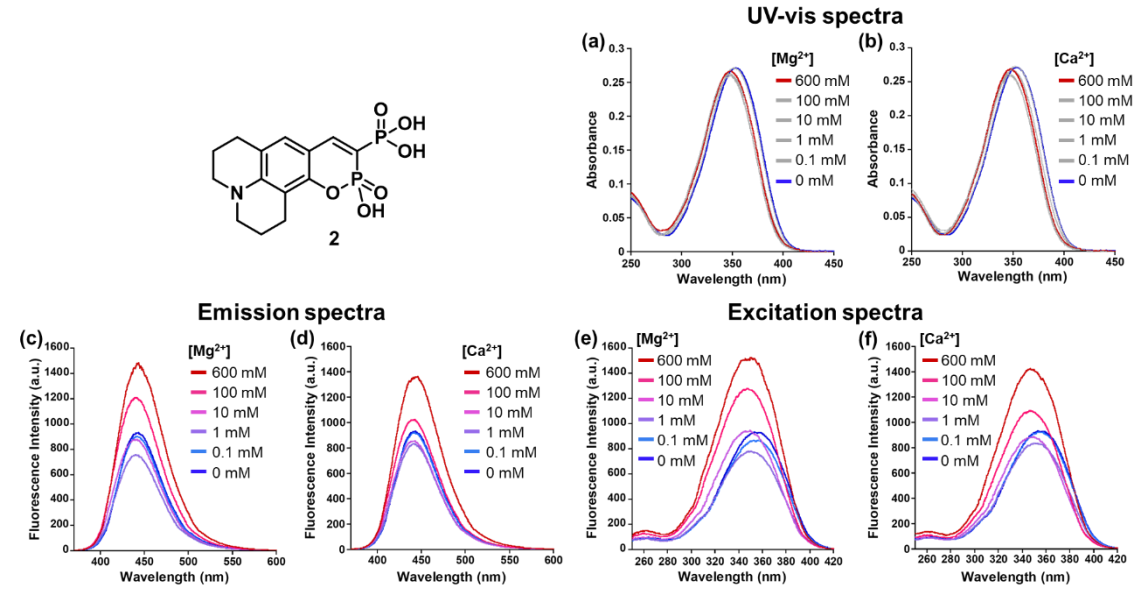

Figure S2-2. (a, b) Absorption spectra of 10 μM compound **2** in 100 mM HEPES buffer (pH 7.4). (a) $[Mg^{2+}]$ = 0, 0.1, 1, 10, 100, 600 mM. (b) $[Ca^{2+}]$ = 0, 0.1, 1, 10, 100, 600 mM. (c, d) Emission spectra of 1 μM compound **2** in 100 mM HEPES buffer (pH 7.4) (λ_{ex} = 355 nm). (c) $[Mg^{2+}]$ = 0, 0.1, 1, 10, 100, 600 mM. (d) $[Ca^{2+}]$ = 0, 0.1, 1, 10, 100, 600 mM. (e, f) Excitation spectra of 1 μM compound **2** in 100 mM HEPES buffer (pH 7.4) (λ_{em} = 442 nm). (e) $[Mg^{2+}]$ = 0, 0.1, 1, 10, 100, 600 mM. (f) $[Ca^{2+}]$ = 0, 0.1, 1, 10, 100, 600 mM.

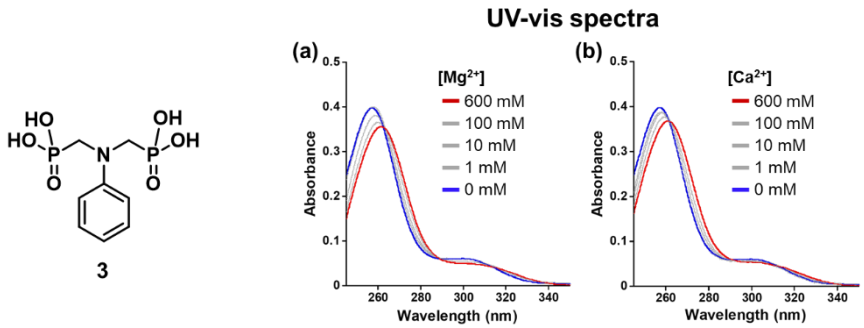

Figure S2-3. (a, b) Absorption spectra of 20 μM compound **3** in 100 mM HEPES buffer (pH 7.4). (a) $[Mg^{2+}]$ = 0, 1, 10, 100, 600 mM. (b) $[Ca^{2+}]$ = 0, 1, 10, 100, 600 mM.

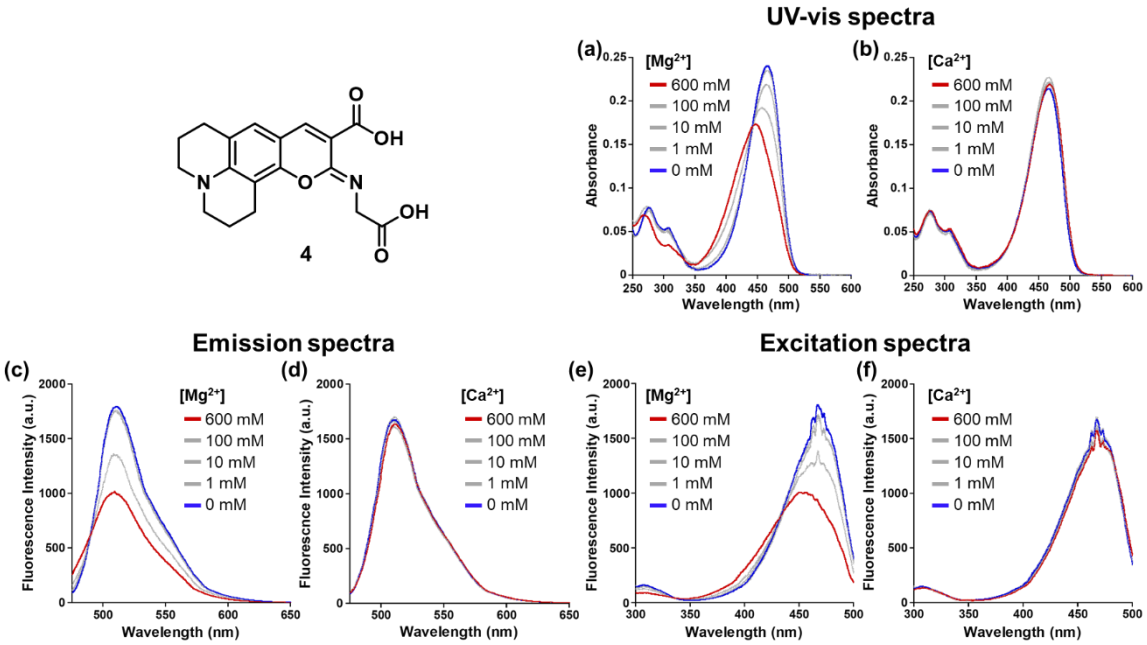

Figure S2-4. (a, b) Absorption spectra of 15 μM compound **4** in 100 mM HEPES buffer (pH 7.4). (a) $[Mg^{2+}]$ = 0, 1, 10, 100, 600 mM. (b) $[Ca^{2+}]$ = 0, 1, 10, 100, 600 mM. (c, d) Emission spectra of 15 μM compound **4** in 100 mM HEPES buffer (pH 7.4) (λ_{ex} = 465 nm). (c) $[Mg^{2+}]$ = 0, 1, 10, 100, 600 mM. (d) $[Ca^{2+}]$ = 0, 1, 10, 100, 600 mM. (e, f) Excitation spectra of 15 μM compound **4** in 100 mM HEPES buffer (pH 7.4) (λ_{em} = 508 nm). (e) $[Mg^{2+}]$ = 0, 1, 10, 100, 600 mM. (f) $[Ca^{2+}]$ = 0, 1, 10, 100, 600 mM.

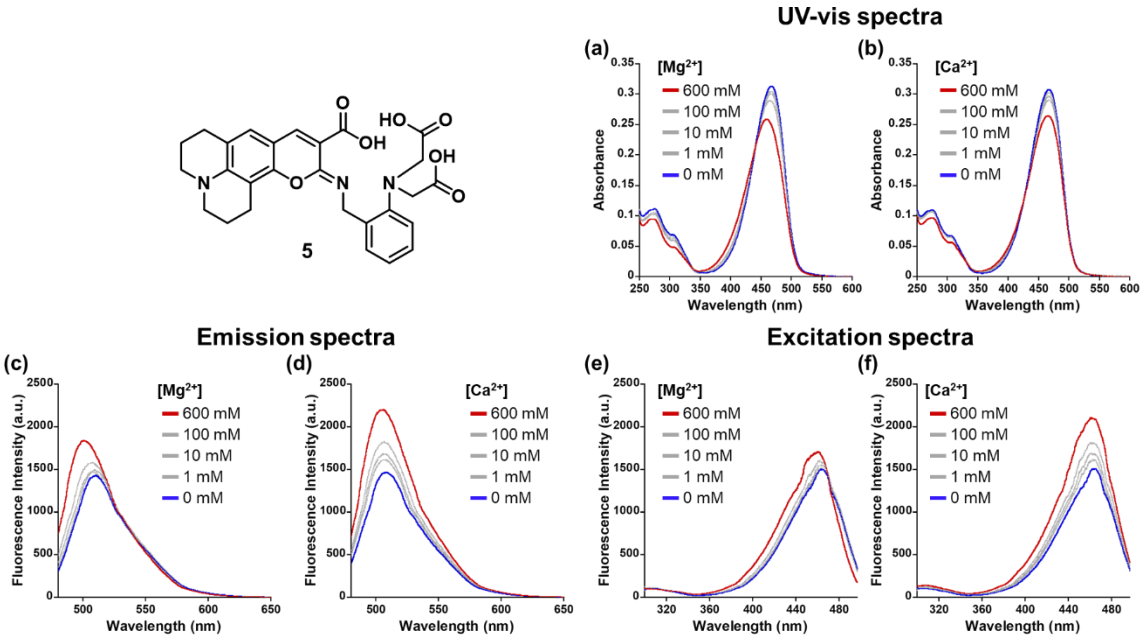

Figure S2-5. (a, b) Absorption spectra of 10 μM compound **5** in 100 mM HEPES buffer (pH 7.4). (a) $[Mg^{2+}]$ = 0, 1, 10, 100, 600 mM. (b) $[Ca^{2+}]$ = 0, 1, 10, 100, 600 mM. (c, d) Emission spectra of 1 μM compound **5** in 100 mM HEPES buffer (pH 7.4) (λ_{ex} = 465 nm). (c) $[Mg^{2+}]$ = 0, 1, 10, 100, 600 mM. (d) $[Ca^{2+}]$ = 0, 1, 10, 100, 600 mM. (e, f) Excitation spectra of 1 μM compound **5** in 100 mM HEPES buffer (pH 7.4) (λ_{em} = 508 nm). (e) $[Mg^{2+}]$ = 0, 1, 10, 100, 600 mM. (f) $[Ca^{2+}]$ = 0, 1, 10, 100, 600 mM.

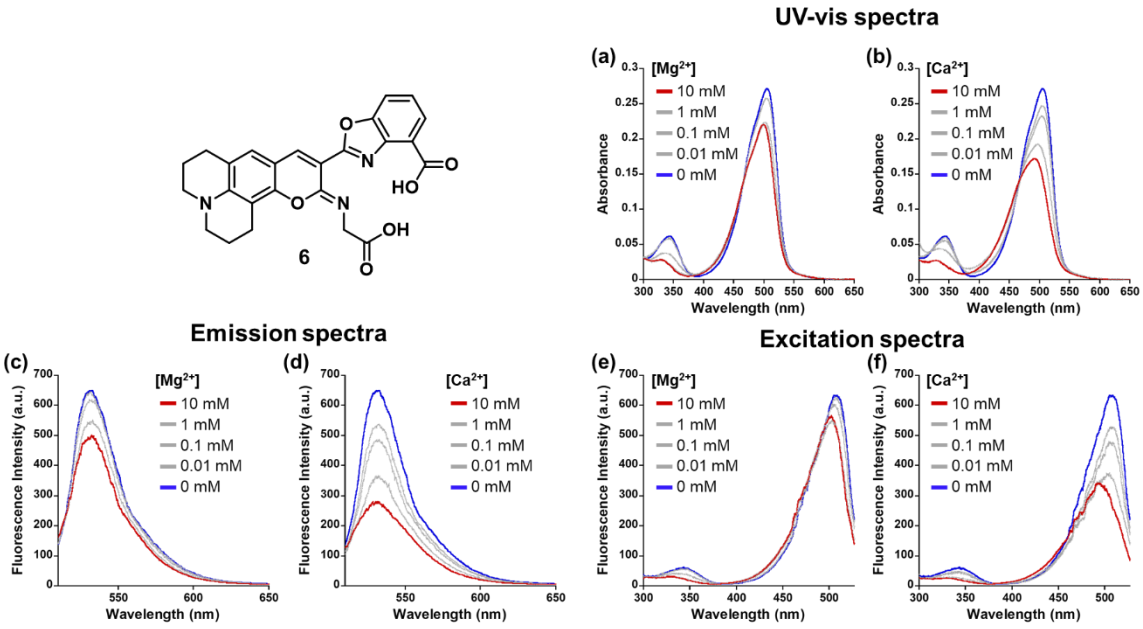

Figure S2-6. (a, b) Absorption spectra of 5 μM compound **6** in 100 mM HEPES buffer (pH 7.4). (a) $[Mg^{2+}]$ = 0, 0.01, 0.1, 1, 10 mM. (b) $[Ca^{2+}]$ = 0, 0.01, 0.1, 1, 10 mM. (c, d) Emission spectra of 1 μM compound **6** in 100 mM HEPES buffer (pH 7.4) (λ_{ex} = 505 nm). (c) $[Mg^{2+}]$ = 0, 0.01, 0.1, 1, 10 mM. (d) $[Ca^{2+}]$ = 0, 0.01, 0.1, 1, 10 mM. (e, f) Excitation spectra of 1 μM compound **6** in 100 mM HEPES buffer (pH 7.4) (λ_{em} = 533 nm). (e) $[Mg^{2+}]$ = 0, 0.01, 0.1, 1, 10 mM. (f) $[Ca^{2+}]$ = 0, 0.01, 0.1, 1, 10 mM.

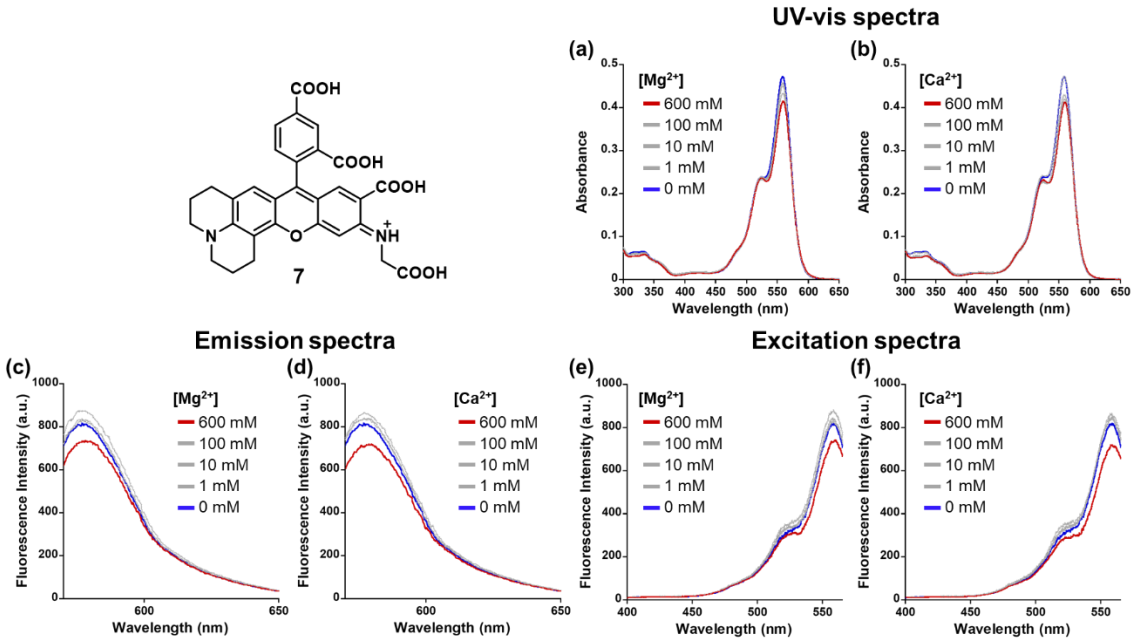

Figure S2-7. (a, b) Absorption spectra of 5 μM compound **7** in 100 mM HEPES buffer (pH 7.4). (a) $[Mg^{2+}]$ = 0, 1, 10, 100, 600 mM. (b) $[Ca^{2+}]$ = 0, 1, 10, 100, 600 mM. (c, d) Emission spectra of 1 μM compound **7** in 100 mM HEPES buffer (pH 7.4) (λ_{ex} = 559 nm). (c) $[Mg^{2+}]$ = 0, 1, 10, 100, 600 mM. (d) $[Ca^{2+}]$ = 0, 1, 10, 100, 600 mM. (e, f) Excitation spectra of 1 μM compound **7** in 100 mM HEPES buffer (pH 7.4) (λ_{em} = 577 nm). (e) $[Mg^{2+}]$ = 0, 1, 10, 100, 600 mM. (f) $[Ca^{2+}]$ = 0, 1, 10, 100, 600 mM.

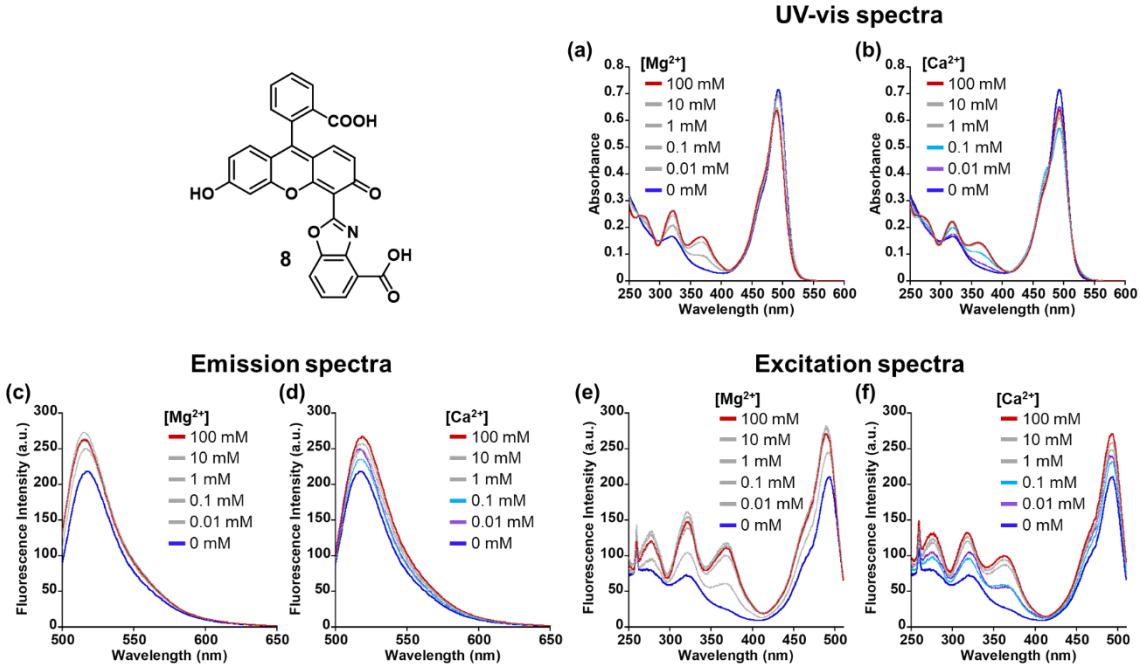

Figure S2-8. (a, b) Absorption spectra of 10 μM compound **8** in 100 mM HEPES buffer (pH 7.4). (a) $[Mg^{2+}]$ = 0, 0.01, 0.1, 1, 10, 100 mM. (b) $[Ca^{2+}]$ = 0, 0.01, 0.1, 1, 10, 100 mM. (c, d) Emission spectra of 1 μM compound **8** in 100 mM HEPES buffer (pH 7.4) (λ_{ex} = 494 nm). (c) $[Mg^{2+}]$ = 0, 0.01, 0.1, 1, 10, 100 mM. (d) $[Ca^{2+}]$ = 0, 0.01, 0.1, 1, 10, 100 mM. (e, f) Excitation spectra of 1 μM compound **8** in 100 mM HEPES buffer (pH 7.4) (λ_{em} = 518 nm). (e) $[Mg^{2+}]$ = 0, 0.01, 0.1, 1, 10, 100 mM. (f) $[Ca^{2+}]$ = 0, 0.01, 0.1, 1, 10, 100 mM.

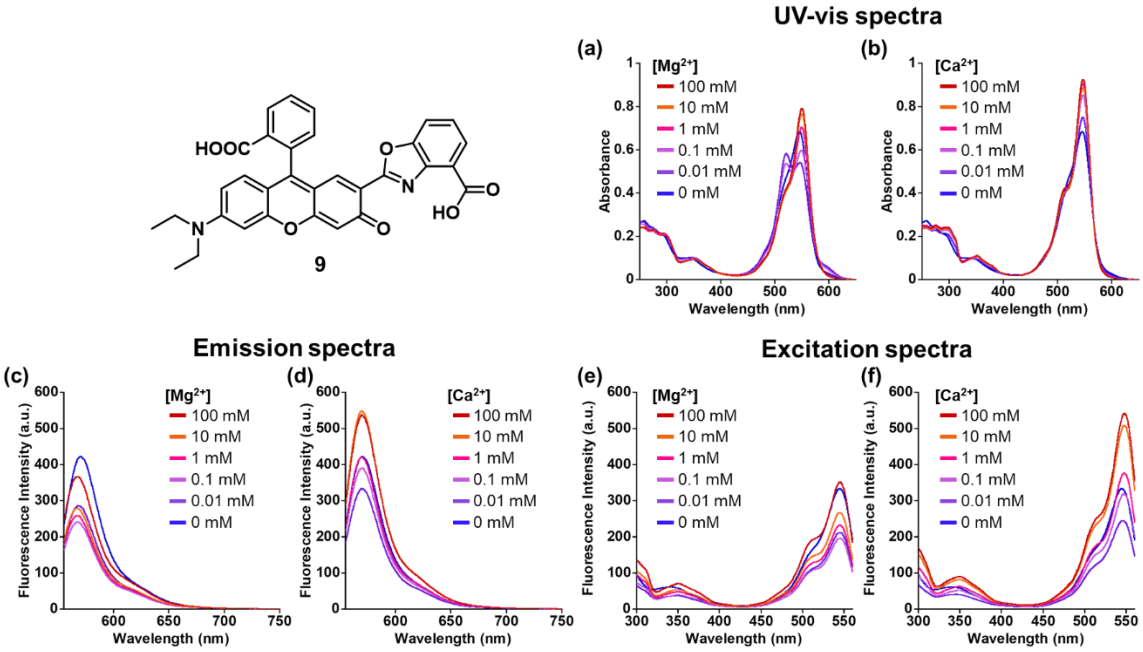

Figure S2-9. (a, b) Absorption spectra of 10 μM compound **9** in 100 mM HEPES buffer (pH 7.4). (a) $[Mg^{2+}]$ = 0, 0.01, 0.1, 1, 10, 100 mM. (b) $[Ca^{2+}]$ = 0, 0.01, 0.1, 1, 10, 100 mM. (c, d) Emission spectra of 1 μM compound **9** in 100 mM HEPES buffer (pH 7.4) (λ_{ex} = 545 nm). (c) $[Mg^{2+}]$ = 0, 0.01, 0.1, 1, 10, 100 mM. (d) $[Ca^{2+}]$ = 0, 0.01, 0.1, 1, 10, 100 mM. (e, f) Excitation spectra of 1 μM compound **9** in 100 mM HEPES buffer (pH 7.4) (λ_{em} = 571 nm). (e) $[Mg^{2+}]$ = 0, 0.01, 0.1, 1, 10, 100 mM. (f) $[Ca^{2+}]$ = 0, 0.01, 0.1, 1, 10, 100 mM.

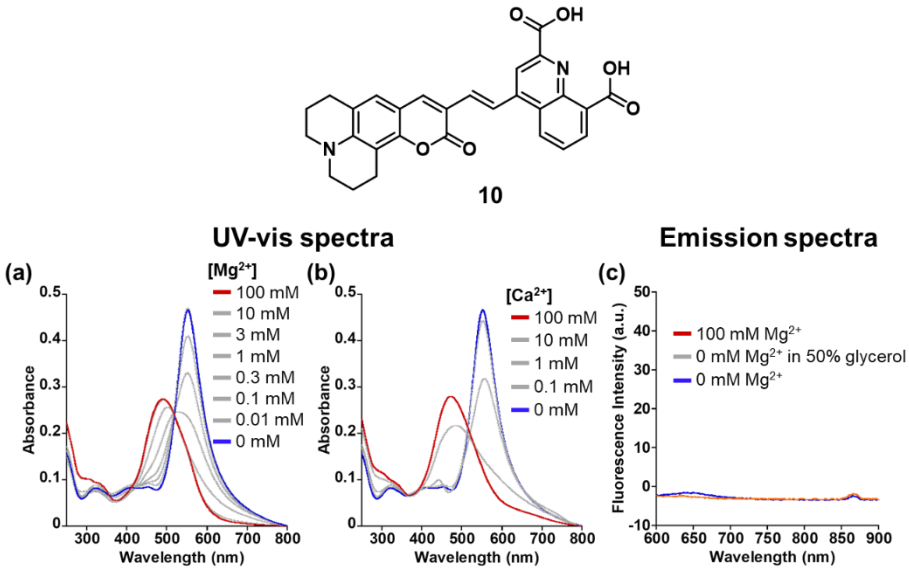

Figure S2-10. (a, b) Absorption spectra of 10 μM compound **10** in 100 mM HEPES buffer (pH 7.4). (a) $[Mg^{2+}]$ = 0, 0.01, 0.1, 0.3, 1, 3, 10, 100 mM. (b) $[Ca^{2+}]$ = 0, 0.1, 1, 10, 100 mM. (c) Emission spectra of 1 μM compound **10** in 100 mM HEPES buffer (pH 7.4) with or without 100 mM Mg^{2+} (λ_{ex} = 552 nm).

Experimental Methods

Materials and instruments

General chemicals for organic synthesis were of the best grade available, supplied by Tokyo Chemical Industries, Wako Pure Chemical, or Sigma-Aldrich Chemical Co, and were used without further purification. Analytical thin-layer chromatography was performed on 60F254 silica plates (Merck & Co., Inc.). Silica gel column chromatography was performed using BW-300 (Fuji Silysia Chemical Ltd.). MGQ-1, MGQ-2 and MGQ-2(AM) were dissolved in DMSO (biochemical grade, Wako) before fluorescence measurements to facilitate solubilization in aqueous solution. Magnesium Green(AM) was purchased from Thermo Fisher Scientific. Ionomycin was purchased from Wako. CMV-R-GECO1.0 was purchased from Addgene. ATP was obtained from Wako Pure Chemical as its disodium salt.

GPC purifications were performed with a JAIGEL 1H-2H column (Japan Analytical Industry Co., Ltd.) using a GPC system that was comprised of a pump (LC-6AD, Shimadzu) and a detector (SPD-20A, Shimadzu). HPLC analyses were performed with an Inertsil ODS-3 (4.6 mm×250 mm) column (GL Sciences Inc.) using an HPLC system that was comprised of a pump (PU-2080, Jasco) and a detector (MD-2010, Jasco). Preparative HPLC was performed with an Inertsil ODS-3 (10.0 mm × 250 mm) column (GL Sciences Inc.) using an HPLC system that comprised a pump (PU-2087, JASCO) and a detector (UV-2075, JASCO). Buffer A was 0.1% HCOOH in H_2O (for MGQ-2(AM)) or 50 mM triethylammonium acetate in H_2O (for MGQ-1 and MGQ-2); Buffer B was 0.1% HCOOH in acetonitrile (for MGQ-2(AM)) or pure acetonitrile (for MGQ-1 and MGQ-2). NMR spectra were recorded on a Bruker Avance 500 instrument at 500 MHz for ^{1}H NMR and 125 MHz for ^{13}C NMR, using tetramethylsilane as an internal standard. Mass spectra were measured on a Waters LCT-Premier XE mass spectrometer or on a JMS-700 (JEOL).

Fluorescence spectra were measured using a Hitachi F7000 spectrometer. The slit widths were 2.5 nm for both excitation and emission, and the photomultiplier voltage was 700 V. UV-visible absorbance spectra were measured using a Jasco aV-650 spectrophotometer. For photostability analysis of MGQ-2, the light irradiation was performed by using a xenon light source (MAX-303, Asahi Spectra) equipped with a band pass filter (490/5 nm for MGQ-2 and fluorescein).

Fluorescence microscopic images were recorded using a confocal fluorescence microscopic imaging system including a fluorescence microscope (IX71, Olympus), an EMCCD (iXon3, Andor Technology), a confocal scanner unit (CSU-X1, Yokogawa Electric Corporation), and a multispectral LED light source (Spectra X light engine,

Lumencor). The filter sets were BP488 ± 3/DM488/BA520 ± 17.5 (for MGQ-2 and Magnesium Green) and BP560 ± 13/DM561/BA624 ± 20 (for R-GECO1.0). The whole system was controlled using MetaMorph 7.6 software (Molecular Devices).

Fluorometric analysis

The relative fluorescence quantum yields of the compounds were obtained by comparing the area under the emission spectrum. The following equation was used to calculate quantum yield:

$$\Phi_x = \Phi_{st} (I_x/I_{st})(A_{st}/A_x)(n_x^2/n_{st}^2)$$

, where Φ_{st} is the reported quantum yield of the standard, I is the integrated emission spectrum, A is the absorbance at the excitation wavelength, and n is the refractive index of the solvent used. The subscripts x and st denote sample and standard, respectively. Fluorescein (Φ = 0.85 when excited at 492 nm in 100 mM NaOH aq.) was used as the standard.

Photostability of MGQ-2 (1 μM, 2 mL) was examined with a 100 mM HEPES buffer (pH 7.4) with 115 mM KCl and 20 mM NaCl at 25 °C under continuous light irradiation through a band pass filter (490 ± 2.5 nm, 4.0 mW/cm^2) using a xenon light source. The fluorescence intensity (λ_{ex} = 515 nm, λ_{em} = 536 nm) was measured every 5 min for 1 h.

Determination of dissociation constants

The apparent dissociation constants (K_d) of MGQ-1 and MGQ-2 for metal ions in 100 mM HEPES buffer (pH 7.4) containing 115 mM KCl and 20 mM NaCl were calculated using the following equation,

$$[M^{n+}] = K_d (F - F_{min})/(F_{max} - F)$$

, where F is the fluorescence intensity at each metal ion concentration, F_{min} is the fluorescence intensity before addition of the metal ions, and F_{max} is the fluorescence intensity at the saturation point.

Metal ion selectivity study

Metal ion selectivity was measured by adding either $MgCl_2$, NaCl, KCl, $ZnCl_2$, $CoCl_2$, $MnCl_2$, $NiCl_2$ or $CuCl_2$ to 1 μM MGQ-2 solution. The fluorescence intensity of MGQ-2 with 20 mM Na^+ or 115 mM K^+ was measured in 100 mM HEPES buffer (pH 7.4). The fluorescence intensity with 1 μM Zn^{2+}, Co^{2+}, Mn^{2+}, Ni^{2+}, or Cu^{2+} was measured in 100 mM HEPES buffer (pH 7.4) with 115 mM KCl and 20 mM NaCl.

Quantum chemical calculation

All calculations of HOMO and LUMO energy levels were performed using the Gaussian 09 program. The geometries of the ground state structures were optimized using Density Functional Theory (DFT) at the B3LYP level. The 6-31G(d) basis set was used for all atoms.

Cell culture

HEK293 cells were cultured in high-glucose Dulbecco's modified Eagle medium (DMEM) plus Gluta Max-I supplemented with 10% fetal bovine serum (FBS), 100 U/mL penicillin, and 100 μg/mL streptomycin. Cells were incubated at 37 °C in a humidified atmosphere with 5% CO_2. A subculture was performed every 2–3 days from subconfluent (<80%) cultures using a trypsin-ethylenediamine tetraacetic acid solution. Transfection of plasmids was carried out in a glass-bottomed dish using Lipofectamine 3000 according to the standard protocol.

Live-cell fluorescence imaging of MGQ-2(AM)

HEK293 cells maintained in 10% FBS in DMEM at 37 °C in 5% CO_2 were washed three times with HBSS and incubated in FBS-free DMEM containing 2 μM MGQ-2(AM) for 45 min in a CO_2 incubator. After washing with HBSS, the medium was replaced with DMEM and the fluorescence images were captured using a confocal fluorescence microscope.

Mg^{2+} export experiment

HEK293 cells were transfected with pCMV-CNNM4-FLAG using Lipofectamine 3000, and the cells were incubated at 37 °C for 24 h. Then, the cells were incubated with Mg^{2+}-loading buffer (78.1 mM NaCl, 5.4 mM KCl, 1.8 mM $CaCl_2$, 40 mM $MgCl_2$, 5.5 mM glucose, 5.5 mM HEPES-KOH, pH 7.4), including 2 μM MGQ-2(AM) or 2 μM Magnesium Green(AM), for 45 min at 37 °C. The cells were rinsed once with loading buffer and the fluorescence images were captured every 20 s using a confocal fluorescence microscope. Then, the buffer was changed to a Mg^{2+}-free buffer ($MgCl_2$ in the loading buffer was replaced with 60 mM NaCl).

Responsivity of MGQ-2 toward increase in $[Ca^{2+}]_i$

HEK293 cells were transfected with pCMV-R-GECO1.0 using Lipofectamine 3000, and the cells were incubated at 37 °C for 24 h. Then, the cells were incubated FBS-free DMEM containing 2 μM MGQ-2(AM) or 2 μM Magnesium Green(AM) for 45 min at

37 °C. The cells were rinsed twice with Mg^{2+}- and Ca^{2+}-free HEPES-buffered Hanks balanced salt solution (HHBSS), then 10 mM Ca^{2+} in Mg^{2+}-free HHBSS was added to the cells. Then, time lapse images were taken with 5 μM ionomycin added after 1 min. The fluorescence images were captured every 10 s using a confocal fluorescence microscope.

Chemical synthesis

Synthesis of compound 1a

Isatic anhydride (4.08 g, 25.0 mmol), dimethyl acetylenedicarboxylate (4.60 mL, 37.5 mmol) and sodium methoxide (54.0 mg, 1.00 mmol) were stirred in MeOH (40 mL) at reflux temperature for 3 h. After cooling, the solvent was evaporated. The residue was then purified by flash column chromatography on silica gel (ethyl acetate/hexane) and subsequently by GPC. Compound **1a** (6.45 g, 86% yield) was obtained as a yellow solid. ^{1}H NMR (500 MHz, $CDCl_3$) δ 11.4 (s, 1H), 7.98 (dd, *J* = 8.0, 1.5 Hz, 1H), 7.36 (m, 1H), 7.00 (m, 1H), 6.66 (m, 1H), 5.60 (s, 1H), 3.96 (s, 1H), 3.79 (s, 1H), 3.73 (s, 1H); ^{13}C NMR (125 MHz, $CDCl_3$) δ 168.4, 167.4, 165.4, 144.7, 142.5, 133.1, 131.5, 121.6, 118.5, 117.2, 99.2, 52.9, 52.4, 51.6; HRMS (FAB^+): Calcd for $[M+H]^+$ 294.0899, found 294.0981.

Synthesis of compound 1b

5-chloroisatic anhydride (2.51 g, 12.7 mmol), dimethyl acetylenedicarboxylate (1.87 mL, 15.3 mmol) and sodium methoxide (27.4 mg, 0.508 mmol) were stirred in MeOH (30 mL) at reflux temperature for 2 h. After cooling, the solvent was evaporated. The residue was then purified by flash column chromatography on silica gel (ethyl acetate/hexane). Compound **1b** (4.01 g, 96%) was obtained as a yellow solid.
^{1}H NMR (500 MHz, $CDCl_3$) δ 11.4 (s, 1H), 7.95 (dd, *J* = 2.0 Hz, 1H), 7.31 (dd, *J* = 6.5, 2.0 Hz 1H), 7.58 (d, *J* = 6.5 Hz, 1H), 5.66 (s, 1H), 3.96 (s, 1H), 3.79 (s, 1H), 3.75 (s, 1H); ^{13}C NMR (125 MHz, $CDCl_3$) δ 168.2, 166.4, 165.0, 144.1, 141.2, 133.0, 131.1, 126.7, 119.7, 118.1, 100.3, 53.01, 52.64, 51.68; HRMS (FAB^+): Calcd for $[M+H]^+$ 328.0510, found 328.0592.

Synthesis of compound 2a

Compound **1a** (5.67 g, 21.7 mmol) was stirred in diphenyl ether (18.1 g) at reflux temperature for 3 h. After cooling, the reaction mixture was purified by flash column chromatography on silica gel (ethyl acetate/hexane). Compound **2a** (4.19 g, 74%) was obtained as a colorless solid.

^{1}H NMR (500 MHz, $CDCl_3$) δ 12.4 (s, 1H), 8.61 (m, 1H), 8.45 (dd, *J* = 8.0, 1.5 Hz, 1H), 7.41 (dd, *J* = 8.0 Hz, 1H), 7.02 (d, *J* = 2.0 Hz, 1H), 4.06 (s, 3H), 4.04 (s, 3H); ^{13}C NMR (125 MHz, $CDCl_3$) δ 179.0, 167.7, 162.8, 140.1, 137.2, 136.1, 132.8, 127.2, 123.0, 115.9, 112.5, 53.8, 52.8; HRMS (FAB^+): Calcd for $[M+H]^+$ 262.0637, found 262.0720.

Synthesis of compound 2b

Compound **1b** (3.98 g, 12.1 mmol) was stirred in diphenyl ether (15.0 g) at reflux temperature for 3 h. After cooling, the reaction mixture was purified by flash column chromatography on silica gel (ethyl acetate/hexane). Compound **2b** (2.08 g, 58%) was obtained as a colorless solid.

^{1}H NMR (500 MHz, $CDCl_3$) δ 12.3 (s, 1H), 8.61 (m, 1H), 8.38 (d, *J* = 2.5 Hz, 1H), 7.01 (d, *J* = 2.0 Hz, 1H), 4.06 (s, 3H), 4.05 (s, 3H); ^{13}C NMR (125 MHz, $CDCl_3$) δ 177.8, 166.6, 162.5, 138.4, 137.3, 136.1, 131.9, 129.3, 128.2, 117.5, 112.5, 53.9, 55.1; HRMS (FAB^+): Calcd for $[M+H]^+$ 296.0248, found 296.0327.

Synthesis of compound 3a

Compound **2a** (3.24 g, 12.4 mmol), 2,6-lutidine (2.16 mL, 18.6 mmol) and 4-(dimethylamino)pyridine (303 mg, 2.48 mmol) were dissolved in DCM (33 mL), and the solution was cooled to 0 °C. Trifluoromethanesulfonic anhydride (3.05 mL, 18.6 mmol) was added dropwise, and the reaction mixture was stirred at room temperature for 2 h. The solvent was removed under reduced pressure. The residue was purified by flash column chromatography on silica gel (ethyl acetate/hexane). Compound **3a** (4.43 g, 91%) was obtained as a brown solid.

^{1}H NMR (500 MHz, $CDCl_3$) δ 8.27 (d, *J* = 8.0 Hz, 2H), 8.23 (s, 1H), 7.86 (dd, *J* = 8.0 Hz, 1H), 4.09 (s, 3H), 4.08 (s, 3H); ^{13}C NMR (125 MHz, $CDCl_3$) δ 166.7, 164.4, 153.6, 149.7, 146.7, 133.0, 132.9, 129.6, 124.0, 122.5, 112.7, 53.6, 53.0; HRMS (FAB^+): Calcd for $[M+H]^+$ 393.0130, found 393.0217.

Synthesis of compound 3b

Compound **2b** (1.98 g, 6.68 mmol), 2,6-lutidine (1.17 mL, 10.0 mmol) and 4-(dimethylamino)pyridine (163 mg, 1.34 mmol) were dissolved in DCM (22 mL), and the solution was cooled to 0 °C. Trifluoromethanesulfonic anhydride (1.64 mL, 10.0 mmol) was added dropwise, and the reaction mixture was stirred at room temperature for 3 h. The solvent was removed under reduced pressure. The residue was purified by flash column chromatography on silica gel (ethyl acetate/hexane). Compound **3a** (1.82 g, 64%) was obtained as a brown solid.

^{1}H NMR (500 MHz, $CDCl_3$) δ 8.24 (s, 1H), 8.20 (s, 2H), 4.09 (s, 3H), 4.08 (s, 3H); ^{13}C NMR (125 MHz, $CDCl_3$) δ 165.4, 164.1, 152.5, 149.7, 145.1, 136.3, 134.4, 134.0, 123.3, 122.7, 113.3, 53.7, 53.2; HRMS (FAB^+): Calcd for $[M+H]^+$ 427.9740, found 427.9825.

Synthesis of compound 4a

Compound **3a** (2.21 g, 5.62 mmol) was dissolved in dioxane (40 mL), and methylboronic acid (1.01 g, 16.9 mmol), K_2CO_3 (3.11 g, 22.5 mmol), and [1,1'-bis(diphenylphosphino)ferrocene] dichloropalladium(II) complex with dichloromethane (459 mg, 0.562 mmol) were added to the solution. The solution was heated to reflux for 2 h. After cooling, the organic layer was washed with water, dried with Na_2SO_4 and evaporated. The residue was then purified by flash column chromatography on silica gel (ethyl acetate/hexane). Compound **4a** (1.25 g, 86%) was obtained as a brown solid.
^{1}H NMR (500 MHz, $CDCl_3$) δ 8.20 (dd, *J* = 8.5, 1.5 Hz, 1H), 8.15 (dd, *J* = 8.5, 1.5 Hz, 1H), 8.10 (s, 1H), 7.69 (dd, *J* = 8.5 Hz, 1H), 4.09 (s, 3H), 4.05 (s, 3H), 2.81 (s, 3H); ^{13}C NMR (125 MHz, $CDCl_3$) δ 167.8, 166.1, 148.3, 146.1, 144.8, 132.8, 131.3, 129.4, 127.3, 127.2, 122.2, 53.1, 52.7, 19.2; HRMS (FAB^+): Calcd for $[M+H]^+$ 260.0845, found 260.0927.

Synthesis of compound 4b

Compound **3b** (1.61 g, 3.75 mmol) was dissolved in dioxane (20 mL), and methylboronic acid (449 mg, 7.5 mmol), K_2CO_3 (2.07 g, 15.0 mmol), and [1,1'-bis(diphenylphosphino)ferrocene] dichloropalladium(II) complex with dichloromethane (306 mg, 0.375 mmol) were added to the solution. The solution was heated to reflux for 7 h. After cooling, the organic layer was washed with water, dried with Na_2SO_4 and evaporated. The residue was then purified by flash column chromatography on silica gel (ethyl acetate/hexane). Compound **4b** (705 mg, 64%) was obtained as a brown solid.
^{1}H NMR (500 MHz, $CDCl_3$) δ 8.15 (d, *J* = 2.5 Hz, 1H), 8.11 (s, 1H), 8.08 (d, *J* = 2.5 Hz, 1H), 4.08 (s, 3H), 4.04 (s, 3H), 2.77 (s, 3H); ^{13}C NMR (125 MHz, $CDCl_3$) δ 166.4, 165.7, 148.5, 145.4, 143.3, 134.4, 133.6, 132.1, 130.3, 126.1, 122.9, 53.18, 52.93, 19.15; HRMS (FAB^+): Calcd for $[M+H]^+$ 294.0455, found 294.0535.

Synthesis of compound 5a

Compound **4a** (500 mg, 1.93 mmol) and selenium dioxide (429 mg, 3.86 mmol) were stirred in dioxane (8 mL) at 80 ºC for 3 h. After cooling, the solution was filtered and evaporated under reduced pressure. The residue was purified by flash column chromatography on silica gel (ethyl acetate/hexane). Compound **5a** (232 mg, 44%) was

obtained as a colorless solid.
^{1}H NMR (500 MHz, $CDCl_3$) δ 10.5 (s, 1H), 9.27 (dd, *J* = 8.5, 1.5 Hz, 1H), 8.64 (s, 1H), 8.22 (dd, *J* = 8.5, 1.5 Hz, 1H), 7.88 (dd, *J* = 8.5 Hz, 1H), 4.11 (s, 3H), 4.09 (s, 3H); ^{13}C NMR (125 MHz, $CDCl_3$) δ 192.4, 167.3, 165.0, 149.2, 154.9, 137.9, 132.9, 131.8, 130.6, 128.0, 126.7, 124.7, 53.5, 52.9; HRMS (FAB^+): Calcd for $[M+H]^+$ 274.0637, found 274.0718.

Synthesis of compound 5b

Compound **4b** (251 mg, 0.856 mmol) and selenium dioxide (104 mg, 0.942 mmol) were stirred in dioxane (8 mL) at 80 ºC for 3 h. After cooling, the solution was filtered and evaporated under reduced pressure. The residue was purified by flash column chromatography on silica gel (ethyl acetate/hexane). Compound **5b** (113 mg, 43%) was obtained as a colorless solid.
^{1}H NMR (500 MHz, $CDCl_3$) δ 10.5 (s, 1H), 9.32 (d, *J* = 2.5 Hz, 1H), 8.64 (s, 1H), 8.16 (d, *J* = 2.5 Hz, 1H), 4.10 (s, 3H), 4.09 (s, 3H); ^{13}C NMR (125 MHz, $CDCl_3$) δ 192.0, 164.9, 164.7, 149.2, 144.4, 137.6, 136.9, 134.2, 132.8, 127.8, 127.1, 125.3, 53.54, 53.10; HRMS (FAB^+): Calcd for $[M+H]^+$ 308.0248, found 308.0326.

Synthesis of compound 6a

Compound **5a** (97.8 mg, 0.358 mmol) and 4-chlororesorcinol (114 mg, 0.788 mmol) were added to a flame-dried three-necked flask under N_2. A DCM/Et_2O (1:1) (10 mL) mixture was added to the flask, and then $MeSO_3H$ (800 μL) was added dropwise at room temperature. The solution was stirred for 17 h. After confirming the completion of the reaction, the solution was diluted with Et_2O, poured into saturated aqueous $NaHCO_3$ and acidified with 2 M HCl aq. to pH 5~6. The solution was extracted with ethyl acetate, and the combined organic extracts were dried with Na_2SO_4 and evaporated under reduced pressure. The residue was purified by flash column chromatography on silica gel (DCM/MeOH). Compound **6a** (166 mg, 85%) was obtained as a pink solid.
^{1}H NMR (500 MHz, Acetone-d_6) δ 8.24 (dd, *J* = 9.0, 1.5 Hz, 1H), 7.92 (dd, *J* = 7.0, 1.5 Hz, 1H), 7.77 (s, 1H), 7.70 (dd, *J* = 9.0, 7.0 Hz, 1H), 6.76 (s, 1H), 6.71 (s, 2H), 6.70 (s, 2H), 3.96 (s, 3H), 3.91 (s, 3H); ^{13}C NMR (125 MHz, Acetone-d_6) δ 170.0, 167.4, 156.0, 154.5, 154.1, 150.3, 146.5, 137.1, 132.1, 130.5, 129.9, 129.5, 128.1, 122.6, 122.0, 112.4, 106.0, 53.87, 53.47, 40.46; HRMS (FAB^+): Calcd for $[M+H]^+$ 544.0488, found 544.0575.

Synthesis of compound 6b

Compound **5b** (101 mg, 0.330 mmol) and 4-chlororesorcinol (105 mg, 0.725 mmol)

were added to a flame-dried three-necked flask under N_2. A DCM/Et_2O (1:1) (10 mL) mixture was added to the flask, and then $MeSO_3H$ (800 µL) was added dropwise at room temperature. The solution was stirred for 20 h. After confirming the completion of the reaction, the solution was diluted with Et_2O, poured into saturated aqueous $NaHCO_3$ and acidified with 2 M HCl aq. to pH 5~6. The solution was extracted with ethyl acetate, and the combined organic extracts were dried with Na_2SO_4 and evaporated under reduced pressure. The residue was purified by flash column chromatography on silica gel (DCM/MeOH). Compound **6b** (130 mg, 68%) was obtained as a pink solid.

^{1}H NMR (500 MHz, Acetone-d_6) δ 8.24 (d, J = 2.5 Hz, 1H), 7.93 (d, J = 2.5 Hz, 1H), 7.81 (s, 1H), 6.76 (s, 2H), 6.71 (s, 2H), 6.68 (s, 1H), 3.98 (s, 3H), 3.91 (s, 3H); ^{13}C NMR (125 MHz, Acetone-d_6) δ 168.5, 167.1, 155.9, 154.6, 153.6, 150.7, 145.0, 138.9, 134.9, 132.2, 131.0, 130.9, 126.9, 122.8, 122.0, 112.6, 106.0, 53.99, 53.82, 40.31; HRMS (FAB$^+$): Calcd for $[M+H]^+$ 578.0098, found 578.0182.

Synthesis of compound 7a

Compound **6a** (122 mg, 0.223 mmol) and *p*-TsOH·H_2O (4.25 mg, 22.3 µmol) were dissolved in CH_3COOH (6 mL) and stirred at 60 °C under N_2 for 19 h. After cooling, the solution was evaporated under reduced pressure and purified by flash column chromatography on silica gel (DCM/MeOH). Compound **7a** (77.0 mg, 66%) was obtained as an orange solid.

^{1}H NMR (500 MHz, DMSO-d_6) δ 8.25 (s, 1H), 8.01 (dd, J = 7.0, 1.5 Hz, 1H), 7.83 (dd, J = 8.5, 1.5 Hz, 1H), 7.71 (dd, J = 7.0, 8.5 Hz, 1H), 7.06 (s, 2H), 6.83 (s, 2H), 4.00 (s, 3H), 3.97 (s, 3H); ^{13}C NMR (125 MHz, DMSO-d_6) δ 167.1, 164.0, 147.6, 143.7, 143.3, 139.4, 133.3, 129.7, 128.5, 127.5, 127.4, 126.4, 122.1, 103.4, 52.27, 51.88; HRMS (FAB$^+$): Calcd for $[M+H]^+$ 524.0226, found 524.0314.

Synthesis of compound 7b

Compound **6b** (120 mg, 0.207 mmol) and *p*-TsOH·H_2O (3.94 mg, 20.7 µmol) were dissolved in CH_3COOH (8 mL) and stirred at 60 °C under N_2 for 19 h. After cooling, the solution was evaporated under reduced pressure and purified by flash column chromatography on silica gel (DCM/MeOH). Compound **7b** (71.7 mg, 62%) was obtained as an orange solid.

^{1}H NMR (500 MHz, DMSO-d_6) δ 8.25 (s, 1H), 8.17 (d, J = 2.5 Hz, 1H), 8.01 (d, J = 2.5 Hz, 1H), 7.08 (s, 2H), 6.78 (s, 2H), 4.01 (s, 3H), 3.97 (s, 3H); ^{13}C NMR (125 MHz, DMSO-d_6) δ 166.8, 164.9, 148.9, 144.1, 143.2, 140.2, 136.3, 134.2, 131.1, 128.8, 128.5, 126.9, 124.1, 104.4, 53.41, 53.22; HRMS (FAB$^+$): Calcd for $[M+H]^+$ 557.9836, found

557.9905.

Synthesis of MGQ-1

Compound **7a** (20.0 mg, 38.1 μmol) was dissolved in 4 mL of MeOH/H_2O (3:1). A 2 M NaOH solution (300 μL) was added dropwise at 0 °C. The reaction mixture was then warmed to room temperature. After stirring for 3 h, the solution was acidified with 2 M HCl aq. and then extracted with ethyl acetate. The combined organic extracts were dried with Na_2SO_4 and evaporated under reduced pressure. The residue was purified by reversed-phase HPLC under the following conditions: A/B = 10/90 (0 min), 30/70 (30 min) (solvent A: MeCN; solvent B: 50 mM trimethylamine acetate (TEAA)). After lyophilization, MGQ-1·2.5Et_3N (18.6 mg, 65%) was obtained as a purple powder.
^{1}H NMR (500 MHz, CD_3CN) δ 8.71 (dd, *J* = 7.0, 1.5 Hz, 1H), 8.26 (s, 1H), 7.88 (dd, *J* = 8.0, 1.5 Hz, 1H), 7.86 (dd, *J* = 7.0, 8.0 Hz, 1H), 6.79 (s, 2H), 6.39 (s, 2H); ^{13}C NMR (125 MHz, CD_3CN) δ 174.7, 167.7, 167.2, 157.5, 154.3, 145.6, 145.2, 144.3, 135.4, 130.9, 129.1, 128.8, 127.7, 127.6, 126.1, 123.4, 110.4, 104.5; HRMS (FAB^+): Calcd for $[M+H]^+$ 495.9913, found 495.9998.

Synthesis of MGQ-2

Compound **7b** (13.9 mg, 24.9 μmol) was dissolved in 4 mL of MeOH/H_2O (3:1). A 2 M NaOH solution (300 μL) was added dropwise at 0 °C. The reaction mixture was then warmed to room temperature. After stirring for 3 h, the solution was acidified with 2 M HCl aq. and then extracted with ethyl acetate. The combined organic extracts were dried with Na_2SO_4 and evaporated under reduced pressure. The residue was purified by reversed-phase HPLC under the following conditions: A/B = 15/85 (0 min), 45/55 (30 min) (solvent A: MeCN; solvent B: 50 mM TEAA). After lyophilization, MGQ-2·2.5Et_3N (8.98 mg, 46%) was obtained as a purple powder.
^{1}H NMR (500 MHz, CD_3CN) δ 8.55 (d, *J* = 2.5 Hz, 1H), 8.27 (s, 1H), 7.88 (d, *J* = 2.5 Hz, 1H), 6.78 (s, 2H), 6.39 (s, 2H); ^{13}C NMR (125 MHz, CD_3CN) δ 174.7, 167.1, 166.8, 157.6, 154.6, 144.9, 143.9, 143.5, 135.2, 134.6, 129.2, 129.0, 128.9, 127.5, 124.4, 110.5, 104.5; HRMS (FAB^+): Calcd for $[M+H]^+$ 529.9523, found 529.9593.

Synthesis of MGQ-2(AM)

MGQ-2 (8.50 mg, 16.0 μmol) and DMF (1.5 mL) was added to a flame-dried three-necked flask under N_2. DIEA (13.8 μL, 80.0 μmol) and bromomethyl acetate (7.84 μL, 80.0 μmol) were added at room temperature. After stirring for 18 h, the solvent was removed under reduced pressure, and ethyl acetate was added to the residue and then it

was washed with water. The organic layer was washed with brine, dried with Na_2SO_4 and evaporated. The residue was purified by HPLC under the following conditions: A/B = 55/45 (0 min), 65/35 (30 min) (solvent A: 0.1% HCOOH in MeCN; solvent B: 0.1% HCOOH in H_2O). After lyophilization, MGQ-2(AM) (4.06 mg, 34%) was obtained as an orange solid.

^{1}H NMR (500 MHz, CD_3CN) δ 8.12 (s, 1H), 8.03 (d, *J* = 2.0 Hz, 1H), 7.45 (d, *J* = 2.0 Hz, 1H), 7.35 (s, 1H), 7.03 (s, 1H), 6.92 (s, 1H), 6.46 (s, 1H), 5.97 (s, 2H), 5.94 (s, 2H), 5.84 (s, 2H), 2.10 (s, 3H), 2.03 (s, 3H), 2.02 (s, 3H); ^{13}C NMR (125 MHz, CD_3CN) δ 177.8, 170.3, 170.2, 170.1, 165.2, 163.5, 158.6, 157.4, 153.0, 148.6, 144.2, 142.6, 140.6, 136.4, 135.7, 135.1, 132.7, 129.3, 129.2, 128.2, 127.7, 124.4, 121.2, 121.0, 116.4, 105.9, 104.0, 85.69, 81.12, 80.57, 20.59, 20.50; HRMS (FAB^+): Calcd for $[M+H]^+$ 746.0157, found 746.0234.

References

1. H. Komatsu, N. Iwasawa, D. Citterio, Y. Suzuki, T. Kubota, K. Tokuno, Y. Kitamura, K. Oka and K. Suzuki, *J. Am. Chem. Soc*. **2004**, *126*, 16353–16360.
2. Y. Shindo, T. Fujii, H. Komatsu, D. Citterio, K. Hotta, K. Suzuki and K. Oka, *PLoS One* **2011**, *6*, e23684.
3. S. C. Schwartz, B. Pinto-Pacheco, J.-P. Pitteloud and D. Buccella, *Inorg. Chem*. **2014**, *53*, 3204–3209.
4. G. Farruggia, S. Iotti, L. Prodi, M. Montalti, N. Zaccheroni, P. B. Savage, V. Trapani, P. Sale and F. I. Wolf, *J. Am. Chem. Soc*. **2006**, *128*, 344–350.
5. A. Sargenti, G. Farruggia, N. Zaccheroni, C. Marraccini, M. Sgarzi, C. Cappadone, E. Malucelli, A. Procopio, L. Prodi, M. Lombardo and S. Iotti, *Nat. Protoc*. **2017**, *12*, 461–471.
6. M. E. Maguire and J. A. Cowan, *Biometals* **2002**, *15*, 203–210.
7. M. Brady, S. D. Piombo, C. Hu and D. Buccella, *Dalton Trans*. **2016**, *45*, 12458–12464.
8. P. A. Otten, R. E. London and L. A. Levy, *Bioconjugate Chem*. **2001**, *12*, 203–212.
9. H. Kobayashi, M. Ogawa, R. Alford, P. L. Choyke and Y. Urano, *Chem. Rev*. **2010**, *110*, 2620–2640.
10. T. Ueno, Y. Urano, K. Setsukinai, H. Takakusa, H. Kojima, K. Kikuchi, K. Ohkubo, S. Fukuzumi and T. Nagano, *J. Am. Chem. Soc*. **2004**, *126*, 14079–14085.
11. D. E. Clapham, *Cell* **2007**, *131*, 1047–1058.
12. R. P. Haugland, *Handbook of Fluorescent Probes and Research Products. 9th ed.*, Molecular Probes Inc., Eugene, Oregon, **2002**.

13. K. P. Carter, A. M. Young and A. E. Palmer, *Chem. Rev*. **2014**, *114*, 4564–4601.
14. T. Yoshida, A. Kakizuka and H. Imamura, *Sci. Rep*. **2016**, *6*, 39618.
15. D. Yamazaki, Y. Funato, J. Miura, S. Sato, S. Toyosawa, K. Furutani, Y. Kurachi, Y. Omori, T. Furukawa, T. Tsuda, S. Kuwabata, S. Mizukami, K. Kikuchi and H. Miki, *PLoS Genet*. **2013**, *9*, e1003983.
16. Y. Zhao, S. Araki, J. Wu, T. Teramoto, Y.-F. Chang, M. Nakano, A. S. Abdelfattah, M. Fujiwara, T. Ishihara, T. Nagai and R. E. Campbell, *Science* **2011**, *333*, 1888–1891.

Chapter 3

HaloTag-conjugated Mg^{2+}-selective Fluorescent Probe for Visualizing Mg^{2+} Dynamics in Specific Organelles over a Long Time Period

In preparation

Introduction

In chapter 2, the author developed highly selective fluorescent Mg^{2+} probes with the novel tridentate chelator. In order to investigate Mg^{2+} dynamics in organelles with high concentration of Ca^{2+} (hundreds μM levels), selective organelle targetability should be provided for MGQ-2. In chapter 1, the author has developed the versatile system to localize Mg^{2+} probes in specific organelles by exploiting a protein-tag, HaloTag. Therefore, in this chapter, the author developed a novel Mg^{2+}-selective fluorescent probe that enables specific localization in HaloTag-expressing organelles by combining the Mg^{2+}-selective probe, MGQ-2, with HaloTag labeling system. This probe could be a useful technique for investigating Mg^{2+} dynamics in specific organelles without interference from Ca^{2+} fluctuations. Particularly, in the ER, mitochondria, and Golgi apparatus, Mg^{2+} dynamics still remain unsolved due to high concentrations of Ca^{2+}. Therefore, elucidation of unknown Mg^{2+}-related biology is expected by using the organelle-targetable Mg^{2+}-selective probe.

Synthesis and optical properties of HaloTag-conjugatable Mg^{2+}-selective fluorescent probe

MGQ-2, which exhibited superior properties for selective detection of $[Mg^{2+}]_i$ change in chapter 2, was attached to HaloTag ligand (Scheme 3-1) by Mannich reaction for development of HaloTag-conjugatable Mg^{2+}-selective fluorescent probe, MGQ-2-Halo (Scheme 3-2).

Scheme 3-1

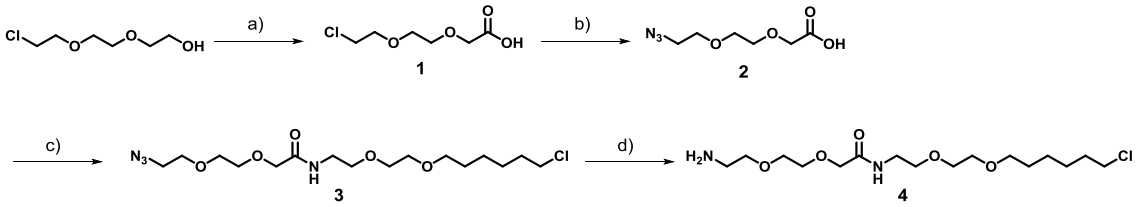

a) Cr_3O, 1.5 M H_2SO_4, acetone, 0 °C→r.t., 42%; b) NaN_3, H_2O, 80 °C, 68%; c) HaloTag Amine (O2) ligand, PyBOP, TEA, DMF, r.t., 32%; d) Pd/C, H_2, MeOH, r.t., quant.

Scheme 3-2

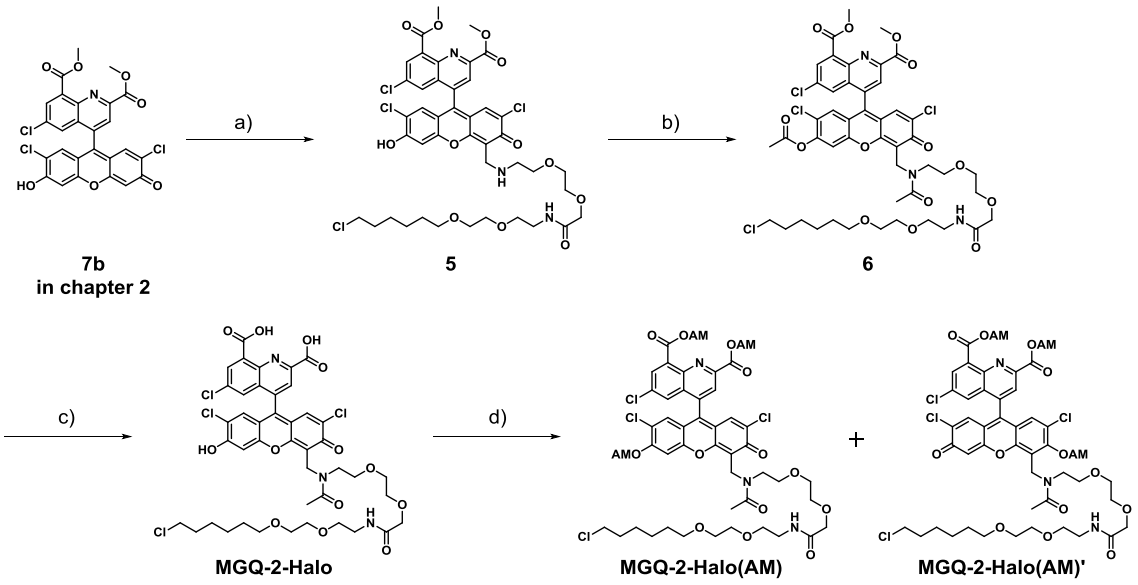

a) compound **4**, paraformaldehyde, CH_3CN/H_2O (1:1), 90 ºC; b) pyridine, Ac_2O, DMF, r.t.; c) 2 M NaOH aq., $MeOH/H_2O$ (3:1), r.t., 16% (3 steps); d) bromomethyl acetate, DIEA, DMF, r.t., 15% obtained as a 1:1 mixture

The absorption spectra of MGQ-2-Halo showed little variation with 100 mM Mg^{2+} (Figure 3-1a), and the fluorescence intensity considerably decreased as Mg^{2+} concentration was increased (Φ_{free} = 0.44, Φ_{bound} < 0.01, K_d (Mg^{2+}) = 0.23 mM) (Figures 3-1a, b and Table 3-1). This turn-off response was attributed to the suppression of the fluorescence by d-PeT as with MGQ-2. The affinity for Ca^{2+} was calculated to be 1.1 mM, which was sufficiently low to hamper recognition of $[Ca^{2+}]_i$ change (Figure 3-1b and Table 3-1). MGQ-2-Halo showed almost no fluorescence response to pH fluctuation in the neutral pH range (pH 7–8) (Figure 3-1c). In acidic pH region, the fluorescence intensity was decreased due to d-PeT caused by protonation of the quinoline moiety. These properties were similar to MGQ-2. Therefore, introduction of HaloTag ligand to

MGQ-2 scarcely affected the optical and coordination properties. The author also examined optical properties of HaloTag-conjugated MGQ-2-Halo, HaloTag-MGQ-2-Halo, after incubation with purified HaloTag protein for 1 h at 37 °C. The changes in absorption and emission spectra after addition of Mg^{2+} were almost same with MGQ-2-Halo (Figures 3-1d and e). The dissociation constants for Mg^{2+} and Ca^{2+} were calculated to be 0.13 and 0.65 mM, respectively (Figure 3-1f and Table 3-1). Approximately 2-fold enhancement of the K_d values for Mg^{2+} and Ca^{2+} corresponded to the case of HaloTag-conjugated MGH in chapter 1.

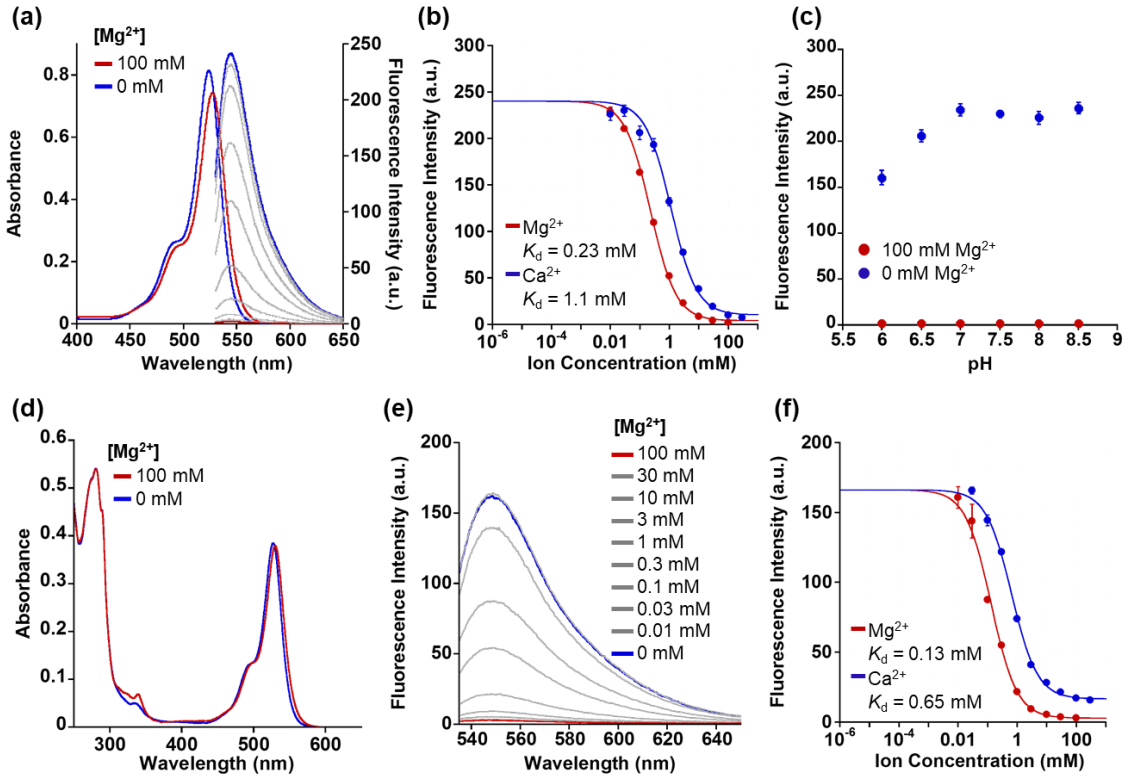

Figure 3-1. (a) Absorption and emission spectra of MGQ-2-Halo at different Mg^{2+} concentrations. Absorption spectra of 10 μM MGQ-2-Halo in the presence or absence of 100 mM Mg^{2+} (100 mM HEPES buffer, 115 mM KCl, 20 mM NaCl, pH 7.4, 37 °C). Emission spectra of 1 μM MGQ-2-Halo in the presence of Mg^{2+} (100 mM HEPES, 115 mM KCl, 20 mM NaCl, pH 7.4, 37 °C). [Mg^{2+}] = 0, 0.01, 0.03, 0.1, 0.3, 1, 3, 30, 100 mM. λ_{ex} = 524 nm. (b) Mg^{2+}- and Ca^{2+}-titration curves of MGQ-2-Halo emission at 545 nm (λ_{ex} = 524 nm). [Ca^{2+}] = 0, 0.01, 0.03, 0.1, 0.3, 1, 3, 10, 30, 100 mM. The error bars denote SD (n = 3). (c) Effect of the pH on the fluorescence intensity of MGQ-2-Halo between pH 6.0–6.5 (in 100 mM MES buffer, 115 mM KCl, 20 mM NaCl) and pH 7.0–8.5 (in 100 mM HEPES buffer, 115 mM KCl, 20 mM NaCl), with or without 100 mM Mg^{2+}. The error bars denote SD (n = 3). (d) Absorption spectra of 5 μM HaloTag-MGQ-2-Halo in the presence or absence of 100 mM Mg^{2+} (100 mM HEPES buffer, 115 mM KCl, 20 mM NaCl, pH 7.4, 37 °C). (e) Emission spectra of 1 μM HaloTag-MGQ-2-Halo complex in the presence of Mg^{2+} (100 mM HEPES, 115 mM KCl, 20 mM NaCl, pH 7.4, 37 °C). [Mg^{2+}] = 0, 0.01, 0.03, 0.1, 0.3, 1, 3, 10, 30, 100 mM. λ_{ex} = 527 nm. (f) Mg^{2+}- and Ca^{2+}-titration curves of HaloTag-MGQ-2-Halo emission at 545 nm (λ_{ex} = 527 nm). [Ca^{2+}] = 0, 0.01, 0.03, 0.1, 0.3, 1, 3, 10, 30, 100 mM. The error bars denote SD (n = 3).

Table 3-1. Spectroscopic properties of MGQ-2-Halo and HaloTag-MGQ-2-Halo[a]

	λ_{abs}/nm	λ_{em}/nm	ε/cm^{-1} M^{-1}	Φ_{free}[b] (Φ_{bound})	K_d (Mg^{2+}) /mM	K_d (Ca^{2+}) /mM
MGQ-2-Halo	524	545	81,000	0.44 (<0.01)	0.23	1.1
HaloTag-MGQ-2-Halo	527	545	77,000	0.38 (<0.01)	0.13	0.65

[a] Measured at 37 °C in 100 mM HEPES buffer (pH 7.4) with 115 mM KCl and 20 mM NaCl.

[b] Relative fluorescence quantum yield determined by using fluorescein (Φ = 0.85 in 0.1 M NaOH aq.) as a standard. Φ_{free} and Φ_{bound} denote the relative fluorescent quantum yield in the absence and presence of 100 mM Mg^{2+}, respectively.

Subcellular targeting of MGQ-2-Halo and long-term imaging in living cells

For live-cell imaging applications, MGQ-2-Halo was derivatized to the acetoxymethyl (AM) form, MGQ-2-Halo(AM), to enhance its cell membrane permeability (Scheme 3-2). HEK293 cells were loaded with 1 μM MGQ-2-Halo(AM) for 45 min at 37 °C. After washing the cells, the intracellular distribution of MGQ-2-Halo in HEK293 cells was confirmed through spinning-disk confocal fluorescence microscopy. The fluorescence of MGQ-2-Halo was homogeneously observed throughout the entire cell unlike the relatively strong localization of MGQ-2 to nuclei in chapter 2 (Figure 3-2). The author assumed that enhancement of hydrophilicity of MGQ-2-Halo caused by introducing hydrophilic ethylene glycol linker between the Mg^{2+} sensor part and the HaloTag ligand improved the intracellular distribution. The author confirmed the subcellular targeting of MGQ-2-Halo to a variety of organelles. HEK293 cells were transfected with a plasmid encoding HaloTag (intracellular region), Halo-NLS (Nuclei), Lyn_{11}-Halo (inner leaflet of cell membrane), or Halo-ER (ER). The HaloTag proteins in transfected cells were labeled with 1 μM MGQ-2-Halo(AM) for 45 min at 37 °C. The fluorescence of MGQ-2-Halo was observed from each target domain without nonspecific fluorescence signals (Figure 3-2). The intended targeting of MGQ-2-Halo to the ER was confirmed by the colocalization with the fluorescent signals of ER-Tracker Red (Figure 3-2). Thus, MGQ-2-Halo successfully localized to various intracellular components. In particular, Mg^{2+} dynamics in ER still remain unknown because ER contains very high concentration of Ca^{2+} (0.5–1 mM), where APTRA-based Mg^{2+} probes cannot visualize Mg^{2+} dynamics correctly due to high affinity for Ca^{2+} (K_d (Ca^{2+}) = 6–35 μM).[1] Therefore, MGQ-2-Halo would be a useful tool to elucidate Mg^{2+}-related biology in such Ca^{2+}-rich organelles.

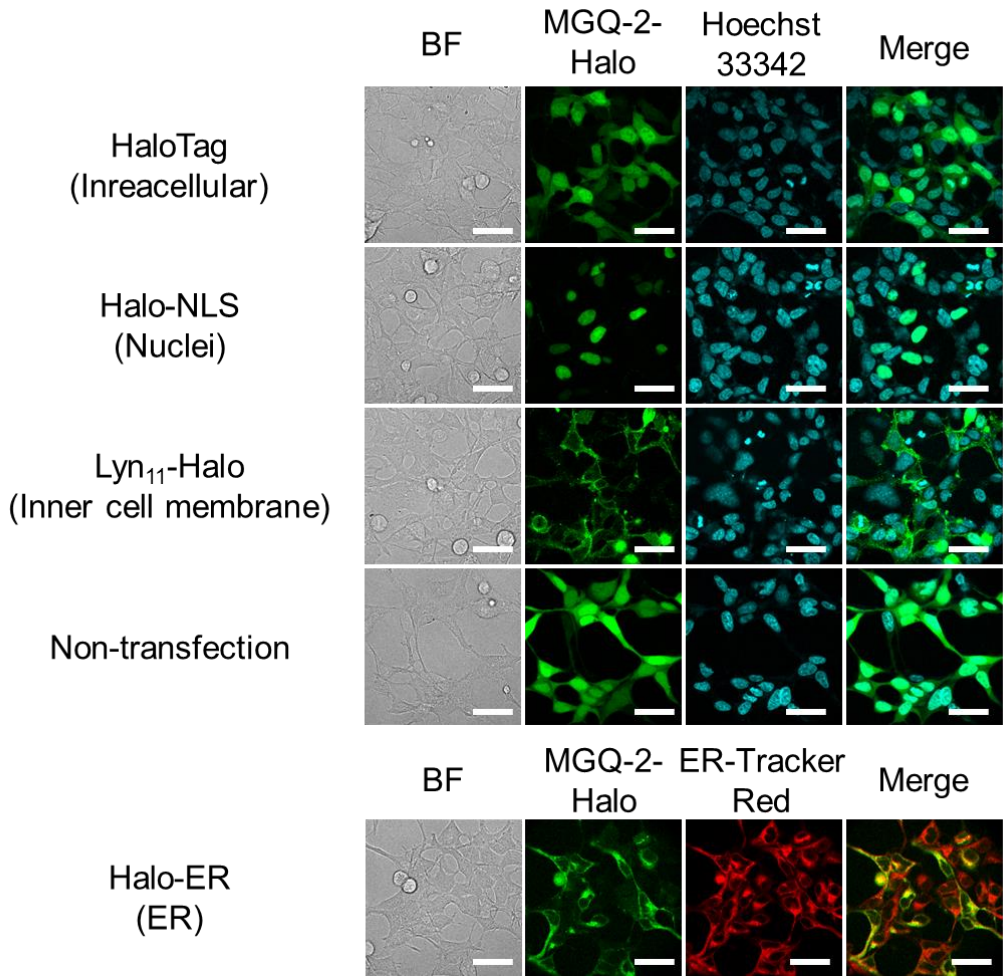

Figure 3-2. Confocal fluorescence microscopic images of MGQ-2-Halo localization in HEK293 cells transfected with a plasmid encoding HaloTag (intracellular region), Halo-NLS (nuclei), Lyn_{11}-Halo (inner leaflet of cell membrane), or Halo-ER (ER). Labeling reactions of fusion proteins in HEK293 cells with 1 μM MGQ-2-Halo(AM) and staining with 200 ng/mL Hoechst 33342 or 200 nM ER-Tracker Red were performed for 45 min at 37 °C. Scale bar: 40 μm.

Next, long-term Mg^{2+} imaging was attempted in living cells for 24 h by using the nucleus-localized MGQ-2-Halo. MGQ-2 which lacks HaloTag ligand was not suitable for long-term imaging due to the very prompt extracellular leakage by anion transporters.[2,3] In fact, the fluorescence of MGQ-2 quickly decreased in a time-dependent manner, and completely disappeared after 2 h (Figures 3-3b and c). In contrast, the fluorescence of nucleus-localized MGQ-2-Halo was continuously detected for 24 h (Figures 3-3a and c). These results indicated that MGQ-2-Halo enables imaging of Mg^{2+} dynamics for more than 24 h.

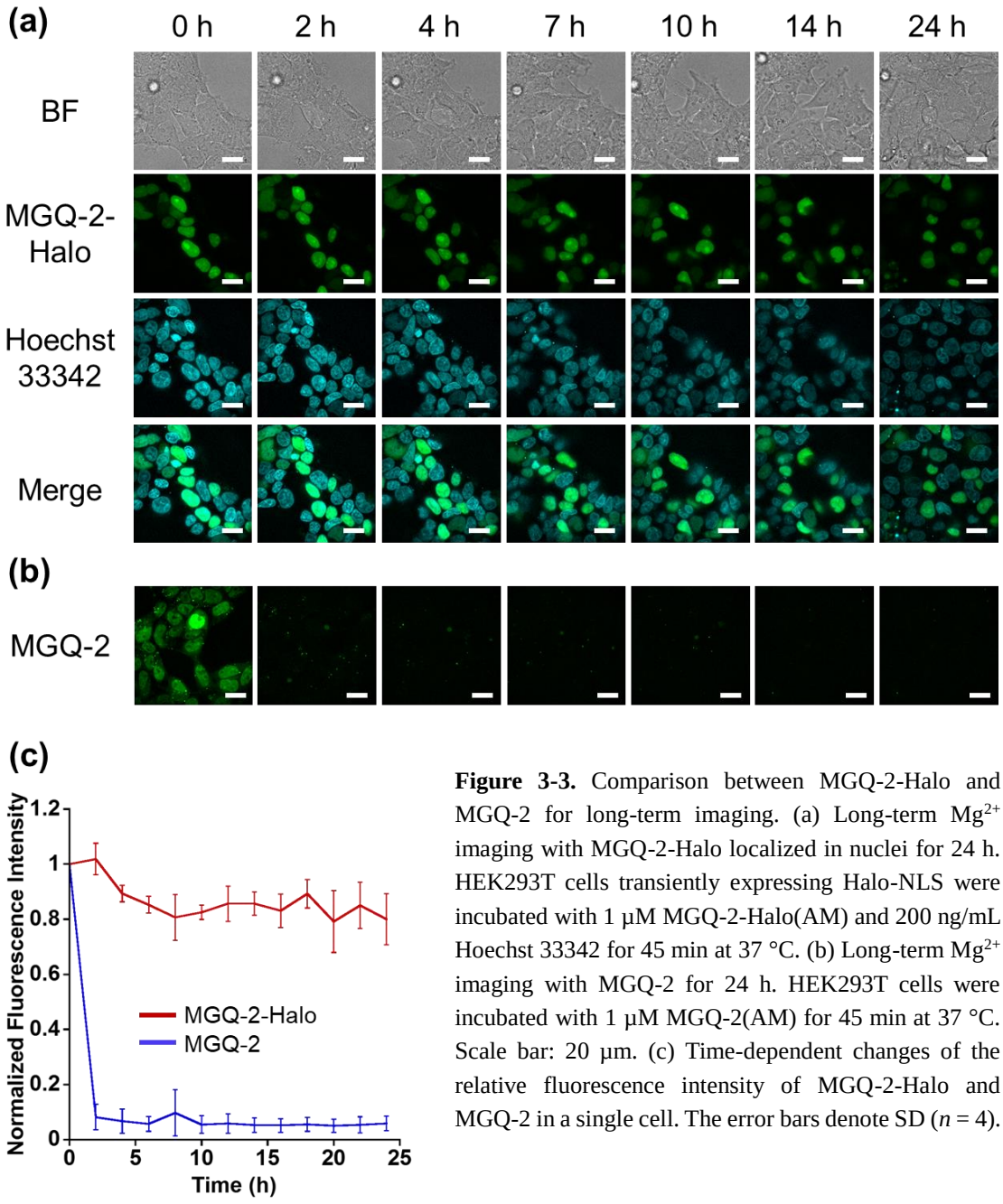

Figure 3-3. Comparison between MGQ-2-Halo and MGQ-2 for long-term imaging. (a) Long-term Mg^{2+} imaging with MGQ-2-Halo localized in nuclei for 24 h. HEK293T cells transiently expressing Halo-NLS were incubated with 1 μM MGQ-2-Halo(AM) and 200 ng/mL Hoechst 33342 for 45 min at 37 °C. (b) Long-term Mg^{2+} imaging with MGQ-2 for 24 h. HEK293T cells were incubated with 1 μM MGQ-2(AM) for 45 min at 37 °C. Scale bar: 20 μm. (c) Time-dependent changes of the relative fluorescence intensity of MGQ-2-Halo and MGQ-2 in a single cell. The error bars denote SD (n = 4).

Responsivity of HaloTag-conjugated MGQ-2-Halo to Mg^{2+} in cells

To examine the response of HaloTag-conjugated MGQ-2-Halo to Mg^{2+} in living cells, $[Mg^{2+}]_i$ change was induced by using a Mg^{2+} transporter, CNNM4.[4] CNNM4-FLAG and HaloTag were co-expressed in HEK293 cells, and the cells were loaded with MGQ-2-Halo(AM) in 40 mM Mg^{2+} buffer. After incubation for 45 min, the extracellular solution was replaced with Mg^{2+}-free buffer to release intracellular Mg^{2+} through CNNM4. The fluorescence intensity of HaloTag-conjugated MGQ-2-Halo immediately increased after Mg^{2+} depletion from the extracellular buffer (Figures 3-4). The fluorescence of the probe in control cells not overexpressing CNNM4 remained constant after addition of Mg^{2+}-free buffer. Thus, it was confirmed that HaloTag-conjugated MGQ-2-Halo responded to $[Mg^{2+}]_i$ change.

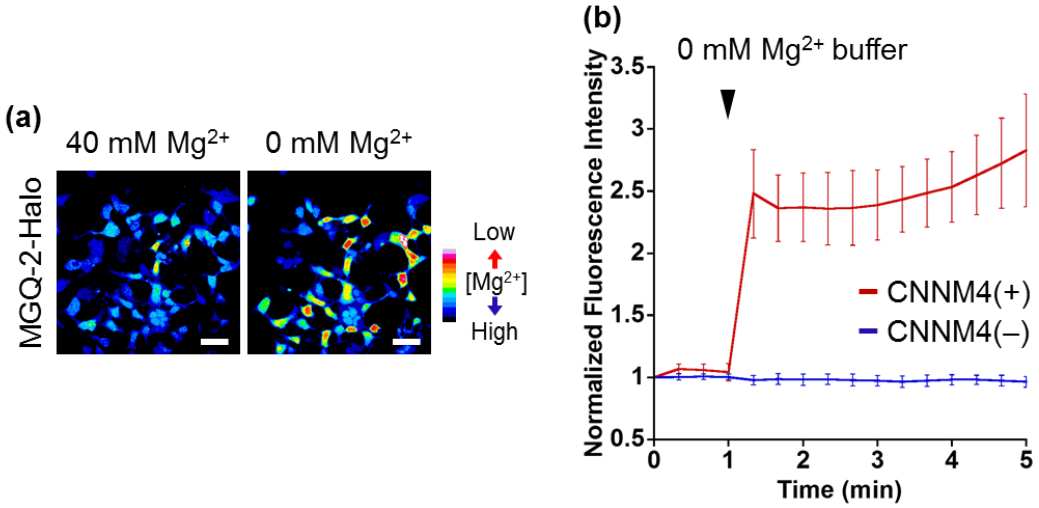

Figure 3-4. (a) Confocal fluorescence microscopic images of Mg^{2+} extrusion with HaloTag-conjugated MGQ-2-Halo. HEK293 cells transfected with CNNM4-FLAG and HaloTag were incubated with Mg^{2+}-loading buffer (78.1 mM NaCl, 5.4 mM KCl, 1.8 mM $CaCl_2$, 40 mM $MgCl_2$, 5.5 mM glucose, 5.5 mM HEPES-KOH, pH 7.4), including 1 μM MGQ-2-Halo(AM) for 45 min at 37 °C. These cells were subjected to Mg^{2+} depletion 1 min after the imaging started. Scale bar: 40 μm. (b) The normalized fluorescence intensity of HaloTag-conjugated MGQ-2-Halo in HEK293 cells subjected to Mg^{2+} depletion. The error bars denote SD (n = 5).

Responsivity of MGQ-2-Halo toward increase in $[Ca^{2+}]_i$

The author confirmed that HaloTag-conjugated MGQ-2-Halo does not respond to $[Ca^{2+}]_i$ variations in living cells. HEK293 cells expressing a genetically-encoded Ca^{2+} specific fluorescent probe, R-GECO,[5] and HaloTag were incubated with MGQ-2-Halo(AM) or a commercially available Mg^{2+} probe, Magnesium Green(AM), for 45 min. After washing the cells with Mg^{2+}- and Ca^{2+}-free HHBSS, 10 mM Ca^{2+} in Mg^{2+}-free HHBSS was added to the cells. After 1 min, 5 µM ionomycin, which is a Ca^{2+} ionophore, was added to introduce extracellular Ca^{2+} into the cells. A large increase in the fluorescence intensity of R-GECO, which indicates $[Ca^{2+}]_i$ increase, was observed after the addition of ionomycin (Figure 3-5). As for the Mg^{2+} probes, although the fluorescence signal of Magnesium Green considerably increased in response to the Ca^{2+} increase, the fluorescence intensity of HaloTag-conjugated MGQ-2-Halo remained constant. This result shows that HaloTag-conjugated MGQ-2-Halo enables to exclusively detect $[Mg^{2+}]_i$ changes without interference from Ca^{2+} fluctuations.

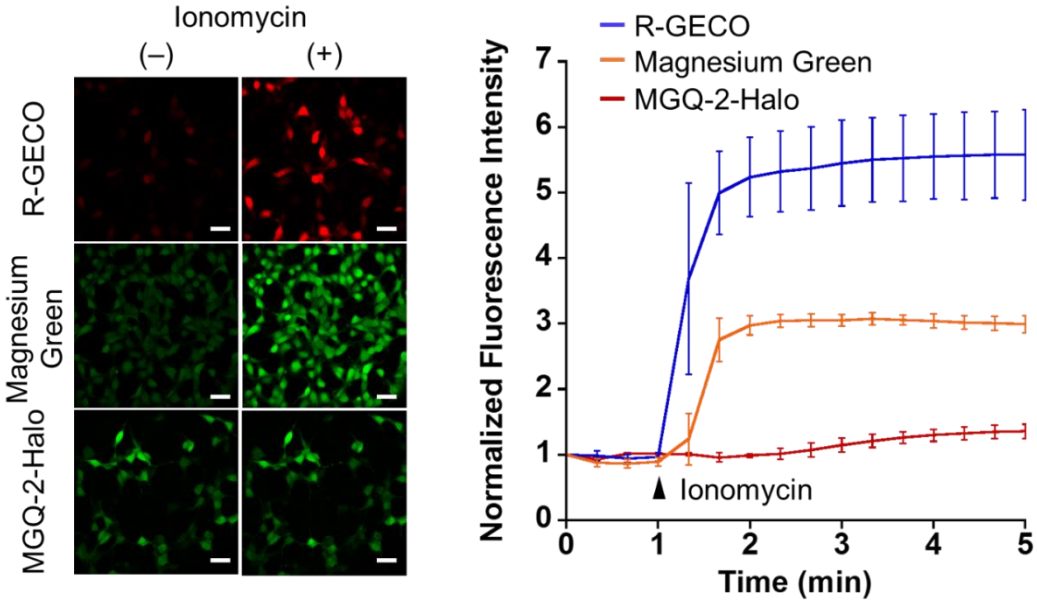

Figure 3-5. Ca^{2+} responsivity of HaloTag-conjugated MGQ-2-Halo in HEK293 cells. HEK293 cells expressing R-GECO and HaloTag were loaded with 1 µM MGQ-2-Halo(AM) or Magnesium Green(AM) for 45 min at 37 °C. After washing with Mg^{2+}- and Ca^{2+}-free HHBSS, 10 mM Ca^{2+} in Mg^{2+}-free HHBSS was added to the cells. Then, 5 µM ionomycin, a Ca^{2+} ionoophore, was added at the indicated time point (arrow). Scale bar: 40 µm. The error bars denote SD (n = 5).

Discussion

Although MGQ-2-Halo has a much smaller affinity for Ca^{2+} than the conventional probes, the probe structure must be further improved for precise evaluation of Mg^{2+} dynamics in Ca^{2+}-rich organelles such as Golgi apparatus, ER and mitochondria (Figure 3-6). In the Golgi apparatus, since pH lies in the range of 6–6.5, the quinoline moiety of DCQ would be protonated. To develop less pH-sensitive Mg^{2+} probes, the author is planning to decrease the pK_a of DCQ by introducing a stronger electron-withdrawing group or by changing the chelator skeleton. ER contains very high concentration of Ca^{2+} ($[Ca^{2+}]_{ER}$ = 0.5–1 mM). Therefore, MGQ-2-Halo (K_d (Ca^{2+}) = 1.1 mM) likely forms complex with Ca^{2+} in the ER. The author needs to develop a Mg^{2+} chelator with weaker affinity for Ca^{2+} by changing from DCQ to chelators with weaker negative charges or more electron deficient chelators. MGQ-2-Halo(AM) was incapable of localizing in mitochondrial matrix due to quick cleavage of AM esters. Modification with propionyloxymethyl (PM) esters or butyryloxymethyl (BM) esters instead of AM esters would be helpful to reduce the speed of de-esterification.[6] These improved derivatives will be powerful chemical tools to clarify unknown physiological Mg^{2+} roles hidden behind the high-concentration of Ca^{2+} in these organelles.

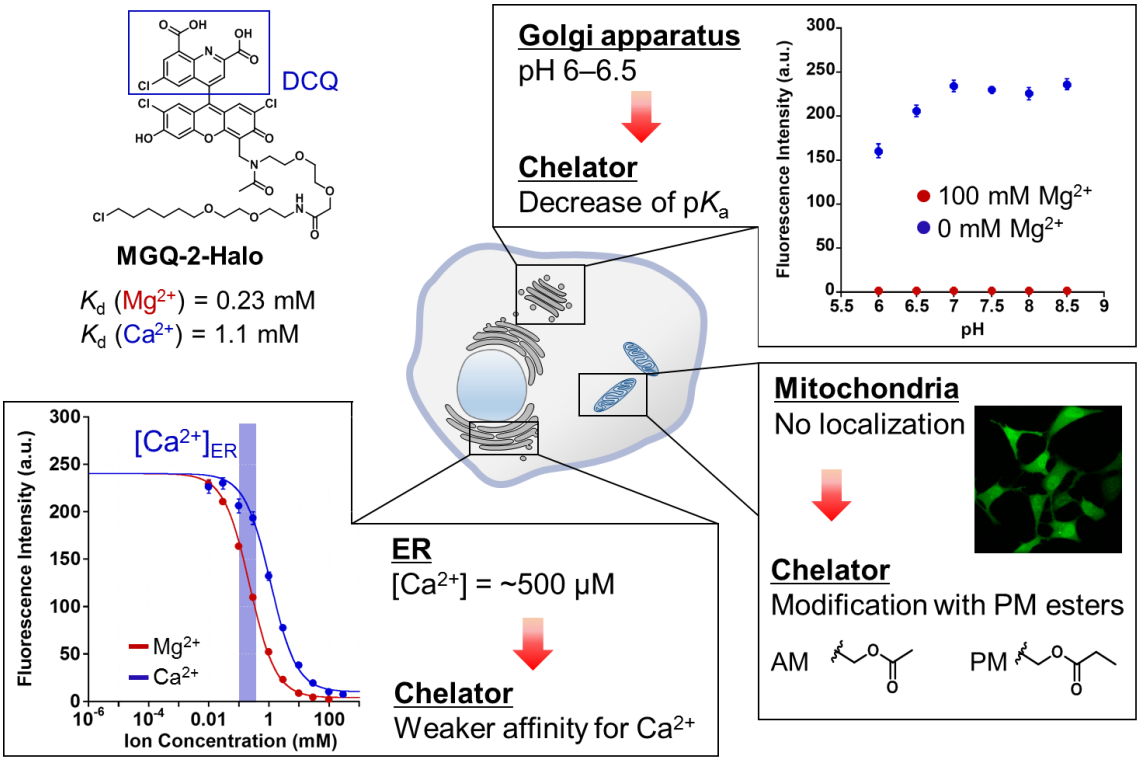

Figure 3-6. Improvement of chelator structure for visualizing Mg^{2+} dynamics in organelles.

Experimental Methods

Materials and instruments

General chemicals for organic synthesis were of the best grade available, supplied by Tokyo Chemical Industries, Wako Pure Chemical, or Sigma-Aldrich Chemical Co, and were used without further purification. Analytical thin-layer chromatography was performed on 60F254 silica plates (Merck & Co., Inc.). Silica gel column chromatography was performed using BW-300 (Fuji Silysia Chemical Ltd.). MGQ-2-Halo and MGQ-2-Halo(AM) were dissolved in DMSO (biochemical grade, Wako) before fluorescence measurements to facilitate solubilization in aqueous solution. Magnesium Green(AM) was purchased from Thermo Fisher Scientific. Ionomycin was purchased from Wako. CMV-R-GECO1.0 was purchased from Addgene.

GPC purifications were performed with a JAIGEL 1H-2H column (Japan Analytical Industry Co., Ltd.) using a GPC system that was comprised of a pump (LC-6AD, Shimadzu) and a detector (SPD-20A, Shimadzu). HPLC analyses were performed with an Inertsil ODS-3 (4.6 mm×250 mm) column (GL Sciences Inc.) using an HPLC system that was comprised of a pump (PU-2080, Jasco) and a detector (MD-2010, Jasco). Preparative HPLC was performed with an Inertsil ODS-3 (10.0 mm × 250 mm) column (GL Sciences Inc.) using an HPLC system that comprised a pump (PU-2087, JASCO) and a detector (UV-2075, JASCO). Buffer A was 0.1% TFA in H_2O (for MGQ-2-Halo(AM)) or 50 mM triethylammonium acetate in H_2O (for MGQ-2-Halo); Buffer B was 0.1% TFA in acetonitrile (for MGQ-2-Halo(AM)) or pure acetonitrile (for MGQ-2-Halo). NMR spectra were recorded on a Bruker Avance 500 instrument at 500 MHz for ^{1}H NMR and 125 MHz for ^{13}C NMR, using tetramethylsilane as an internal standard. Mass spectra were measured on a Waters LCT-Premier XE mass spectrometer or on a JMS-700 (JEOL).

Fluorescence spectra were measured using a Hitachi F7000 spectrometer. The slit widths were 2.5 nm for both excitation and emission, and the photomultiplier voltage was 700 V. UV-visible absorbance spectra were measured using a Jasco aV-650 spectrophotometer.

Fluorescence microscopic images were recorded using a confocal fluorescence microscopic imaging system including a fluorescence microscope (IX71, Olympus), an EMCCD (iXon3, Andor Technology), a confocal scanner unit (CSU-X1, Yokogawa Electric Corporation), and a multispectral LED light source (Spectra X light engine, Lumencor). The filter sets were BP377 ± 25/DM405/BA447 ± 30 (for Hoechst 33342), BP488 ± 3/DM488/BA520 ± 17.5 (for MGQ-2-Halo and Magnesium Green) and BP560 ± 13/DM561/BA624 ± 20 (for R-GECO1.0 and ER-Tracker™ Red). The whole system

was controlled using MetaMorph 7.6 software (Molecular Devices).

Fluorometric analysis

The relative fluorescence quantum yields of the compounds were obtained by comparing the area under the emission spectrum. The following equation was used to calculate quantum yield:

$$\Phi_x = \Phi_{st} (I_x/I_{st})(A_{st}/A_x)(n_x^2/n_{st}^2)$$

, where Φ_{st} is the reported quantum yield of the standard, I is the integrated emission spectrum, A is the absorbance at the excitation wavelength, and n is the refractive index of the solvent used. The subscripts x and st denote sample and standard, respectively. Fluorescein (Φ = 0.85 when excited at 492 nm in 100 mM NaOH aq.) was used as the standard.

Determination of dissociation constants

The apparent dissociation constants (K_d) of MGQ-2-Halo for metal ions in 100 mM HEPES buffer (pH 7.4) containing 115 mM KCl and 20 mM NaCl were calculated using the following equation,

$$[M^{n+}] = K_d (F - F_{min})/(F_{max} - F)$$

, where F is the fluorescence intensity at each metal ion concentration, F_{min} is the fluorescence intensity before addition of the metal ions, and F_{max} is the fluorescence intensity at the saturation point.

Cell culture

HEK293 cells were cultured in high-glucose Dulbecco's modified Eagle medium (DMEM) plus Gluta Max-I supplemented with 10% fetal bovine serum (FBS), 100 U/mL penicillin, and 100 μg/mL streptomycin. Cells were incubated at 37 °C in a humidified atmosphere with 5% CO_2. A subculture was performed every 2–3 days from subconfluent (<80%) cultures using a trypsin-ethylenediamine tetraacetic acid solution. Transfection of plasmids was carried out in a glass-bottomed dish using Lipofectamine 3000 according to the standard protocol.

Live-cell fluorescence imaging of MGQ-2-Halo(AM)

HEK293 or HEK293T cells maintained in 10% FBS in DMEM at 37 °C in 5% CO_2 were transfected with pcDNA-3.1-(+)-Halo-NLS, pcDNA-3.1-(+)-Lyn_{11}-Halo, pcDNA-3.1-(+)-HaloTag, or pCMV-Halo-ER plasmids using Lipofectamine 3000, and the cells were incubated at 37 °C for 24 h. Then, the cells were washed three times with HBSS and

incubated in FBS-free DMEM containing 1 μM MGQ-2-Halo(AM) for 45 min in a CO_2 incubator. After washing with HBSS, fluorescence images were captured in FBS-free DMEM using a confocal fluorescence microscope at 37 °C.

Mg^{2+} export experiment

HEK293 cells were transfected with pCMV-CNNM4-FLAG using Lipofectamine 3000, and the cells were incubated at 37 °C for 24 h. Then, the cells were incubated with Mg^{2+}-loading buffer (78.1 mM NaCl, 5.4 mM KCl, 1.8 mM $CaCl_2$, 40 mM $MgCl_2$, 5.5 mM glucose, 5.5 mM HEPES-KOH, pH 7.4), including 1 μM MGQ-2-Halo(AM) for 45 min at 37 °C. The cells were rinsed once with Mg^{2+}-loading buffer and the fluorescence images were captured every 20 s using a confocal fluorescence microscope. Then, the buffer was changed to a Mg^{2+}-free buffer ($MgCl_2$ in the loading buffer was replaced with 60 mM NaCl).

Responsivity of MGQ-2-Halo toward increase in $[Ca^{2+}]_i$

HEK293 cells were transfected with pCMV-R-GECO1.0 using Lipofectamine 3000, and the cells were incubated at 37 °C for 24 h. Then, the cells were incubated FBS-free DMEM containing 1 μM MGQ-2-Halo(AM) or 1 μM Magnesium Green(AM) for 45 min at 37 °C. The cells were rinsed twice with Mg^{2+}- and Ca^{2+}-free HEPES-buffered Hanks balanced salt solution (HHBSS), then 10 mM Ca^{2+} in Mg^{2+}-free HHBSS was added to the cells. Then, time lapse images were taken with 5 μM ionomycin added after 1 min. The fluorescence images were captured every 20 s using a confocal fluorescence microscope.

Chemical synthesis

Compounds **1** and **2** were prepared according to the previously described procedures.[9]

Synthesis of compound 1

Chromium trioxide (25.0 g, 162 mmol) was dissolved in 300 mL of 1.5 M H_2SO_4 aq., and the solution was cooled to 0 ºC. 2-[2-(chloroethoxy)ethoxy]ethanol (8.30 g, 49.2 mmol) in 150 mL of acetone was dropwisely added, and the reaction mixture was stirred at room temperature for 3 h. The solvent was removed under reduced pressure, and the aqueous layer was extracted with DCM. The combined organic layer was washed with brine and dried with Na_2SO_4 and evaporated. Compound **1** (4.89 g, 42%) was obtained as a colorless oil.

^{1}H NMR (500 MHz, $CDCl_3$) δ 10.21 (bs, 1H), 4.23 (s, 2H), 3.79 (t, J = 5.5 Hz, 4H), 3.73

(t, J = 5.5 Hz, 2H), 3.65 (t, J = 5.5 Hz, 2H); MS (ESI$^-$): Calcd for $[M–H]^-$ 181.0346, found 180.9873.

Synthesis of compound 2

Compound **1** (3.38 g, 18.5 mmol) and NaN_3 (4.81 g, 74.0 mmol) in 13 mL of H_2O were stirred with heating at 80 ºC for 32 h. After cooling to room temperature, the reaction mixture was acidified with 2 M HCl aq. and extracted with DCM. The combined organic layer was dried with Na_2SO_4 and evaporated. Compound **2** (2.39 g, 68%) was obtained as a colorless oil.

^{1}H NMR (500 MHz, $CDCl_3$) δ 9.40 (bs, 1H), 4.22 (s, 2H), 3.79-3.77 (m, 2H), 3.73-3.69 (m, 4H), 3.42 (t, J = 5.0 Hz, 2H); MS (ESI$^-$): Calcd for $[M–H]^-$ 188.0750, found 188.3099.

Synthesis of compound 3

Compound **2** (63.4 mg, 0.330 mmol) were dissolved in dry DMF (1 mL). PyBOP (229 mg, 0.44 mmol) and dry TEA (124 µL, 0.88 mmol) were added at room temperature under Ar. After stirring for 30 min, HaloTag® Amine (O2) Ligand (50.0 mg, 0.22 mmol) was added at room temperature. After stirring for 15 h, the solvent was removed under reduced pressure and ethyl acetate was added to the residue, and washed with 10% citric acid and water. The organic layer was washed with brine, dried with Na_2SO_4 and evaporated. The residue was purified by column chromatography on silica gel (DCM/MeOH = 98:2) and subsequently by GPC. Compound **3** (28.0 mg, 32%) was obtained as a colorless oil.

^{1}H NMR (500 MHz, $CDCl_3$) δ 7.28 (s, 1H), 4.01 (s, 2H), 3.70–3.41 (m, 20H), 1.79–1.76 (m, 2H), 1.62–1.59 (m, 2H), 1.46–1.44 (m, 2H), 1.39–1.37 (m, 2H); ^{13}C NMR (125 MHz, $CDCl_3$) δ 169.8, 71.3, 70.9, 70.6, 70.3, 70.1, 70.0, 69.8, 50.6, 45.1, 38.6, 32.5, 29.5, 26.7, 25.4; HRMS (FAB$^+$): Calcd for $[M+H]^+$ 395.1983, found 395.2067.

Synthesis of compound 4

Compound **3** (25.0 mg, 63.3 µmol) was dissolved in MeOH (2 ml). Pd/C (20%, 5.00 mg) was added and the reaction was stirred for 2 h under H_2. The solution was filtered through a layer celite and evaporated under reduced pressure. Compound **4** (23.4 mg, quant.) was obtained as a colorless oil.

^{1}H NMR (500 MHz, $CDCl_3$) δ 4.02 (s, 2H), 3.70-3.45 (m, 18H), 2.92 (t, J = 5.0 Hz, 2H), 1.81–1.75 (m, 2H), 1.63–1.57 (m, 2H), 1.49–1.43 (m, 2H), 1.40–1.35 (m, 2H); ^{13}C NMR (125 MHz, $CDCl_3$) δ 170.0, 72.9, 71.3, 71.0, 70.6, 70.3, 70.1, 70.0, 69.9, 45.1, 41.6, 38.7, 32.5, 29.5, 26.7, 25.4; HRMS (FAB$^+$): Calcd for $[M+H]^+$ 369.2078, found 369.2158.

Synthesis of compound 5

Compound **4** (23.4 mg, 63.0 μmol) was combined with paraformaldehyde (12.6 mg, 0.420 mmol) in 2 mL of acetonitrile under N_2 and heated to reflux for 1 h. Compound **7b** (29.3 mg, 52.5 μmol) suspended in 2 mL of MeCN and 2 mL of H_2O was added to the reaction solution, and the mixture was refluxed for 48 h. After cooling, the solvent was removed under reduced pressure and purified by flash column chromatography on silica gel (DCM/MeOH = 99:1→85:15). Compound **5** (14.8 mg) obtained as an orange solid was used in next synthesis without further purification.

MS (ESI^+): Calcd for $[M+H]^+$ 938.1914, found 938.1415

Synthesis of compound 6

Compound **5** (14.8 mg) and pyridine (5.10 μL) were stirred in dry DMF (4 mL) at room temperature for 30 min. Acetic anhydride (6.00 μL) was added to the reaction solution. After stirring for 4 h, the solvent was removed under reduced pressure. The residue was dissolved in ethyl acetate and washed with 10% citric acid. The organic layer was dried with Na_2SO_4 and evaporated under reduced pressure. The crude mixture of compound **6** was used in further synthesis without purification.

Synthesis of MGQ-2-Halo

To the crude residue obtained in the preparation of compound **6** was added MeOH/H_2O (3:1) (4 mL). 2 M NaOH aq. (1 mL) was dropwisely added at 0 ºC. The reaction mixture was warmed at room temperature. After stirring for 15 h, the solution was acidified with 2 M HCl aq. and then extracted with ethyl acetate. The combined organic extracts were dried with Na_2SO_4 and evaporated under reduced pressure. The residue was purified by reversed-phase HPLC under the following conditions: A/B = 25/75 (0 min), 45/55 (30 min) (solvent A: MeCN; solvent B: 50 mM TEAA). After lyophilization, MGQ-2-Halo·Et_3N (10.0 mg, 16%) was obtained as a purple powder.

^1H NMR (500 MHz, DMSO-d_6) δ 8.48 (s, 1H), 8.23 (s, 1H), 8.01 (s, 1H), 7.69–7.65 (m, 1H), 6.79 (ss, 2H), 6.37 (s, 1H), 4.88–4.64 (m, 2H), 3.88 (s, 2H), 3.60–3.12 (m, 20H), 3.10 (q, *J* = 7.0 Hz, 6H), 2.40 (s, 3H), 1.68–1.65 (m, 2H), 1.46–1.43 (m, 2H), 1.34–1.33 (m, 2H), 1.28–1.26 (m, 2H), 1.19 (t, *J* = 7.0 Hz, 9H); ^{13}C NMR (125 MHz, DMSO-d_6) δ 173.5, 170.4, 169.6, 169.6, 165.9, 164.8, 156.6, 154.9, 144.1, 143.3, 143.1, 134.7, 133.8, 129.0, 128.8, 128.2, 127.1, 126.8, 126.6, 124.2, 111.3, 111.2, 109.4, 109.1, 104.2, 104.1, 70.70, 70.64, 70.53, 70.44, 70.15, 69.97, 69.86, 69.76, 69.31, 67.98, 46.04, 45.81, 38.43, 32.47, 29.50, 26.57, 25.36, 22.55, 9.08; HRMS (FAB^+): Calcd for $[M+H]^+$ 952.1706,

found 952.1790.

Synthesis of MGQ-2-Halo(AM)

To a flame-dried three-necked flask placed under N_2 was added MGQ-2-Halo (8.53 mg, 8.94 μmol) and DMF (1.5 mL). DIEA (12.3 μL, 71.6 μmol) and bromomethyl acetate (7.00 μL, 7.16 μmol) were added at room temperature. After stirring for h, the solvent was removed under reduced pressure, and ethyl acetate was added to the residue and washed with water. The organic layer was washed with brine, dried with Na_2SO_4 and evaporated. The residue was purified by reversed-phase HPLC under the following conditions: A/B = 60/40 (0 min), 70/30 (30 min) (solvent A: 0.1% TFA in MeCN; solvent B: 0.1% TFA in H_2O). MGQ-2-Halo(AM) (1.56 mg, 15%) was obtained as an orange solid (MGQ-2-Halo(AM):MGQ-2-Halo(AM)' = 1:1 mixture).

^{1}H NMR (500 MHz, CD_3CN) δ 8.23 (d, 1H), 8.14 (t, *J* = 2.0 Hz, 1H), 7.86 (dd, *J* = 2.0 Hz, 1H), 7.53 (d, 1H), 7.21–7.14 (m, 2H), 7.05 (d, 1H), 6.08 (s, 2H), 6.05 (s, 2H), 5.98 (s, 2H), 4.95–4.85 (m, 2H), 3.93 (s, 2H), 3.74–3.36 (m, 20H), 2.21–2.20 (m, 6H), 2.16 (s, 3H) 2.13 (s, 3H), 1.77–1.71 (m, 2H), 1.54–1.49 (m, 2H), 1.44–1.38 (m, 2H), 1.36–1.29 (m, 2H); ^{13}C NMR (125 MHz, CD_3CN) δ 177.3, 170.3, 170.2, 170.1, 170.1, 165.2, 163.5, 157.5, 156.2, 153.3, 148.6, 144.2, 140.6, 140.6, 135.7, 135.7, 135.2, 132.7, 129.4, 129.2, 129.1, 128.0, 127.7, 124.4, 121.4, 120.7, 116.3, 104.1, 104.0, 85.87, 85.70, 81.13, 80.58, 71.31, 71.23, 70.83, 70.52, 70.43, 70.30, 69.80, 69.75, 45.83, 42.68, 38.88, 32.89, 29.84, 26.95, 25.72, 20.67, 20.59, 20.52; HRMS (FAB$^+$): Calcd for $[M+Na]^+$ 1190.2340, found 1190.2249.

References

1. R. P. Haugland, *Handbook of Fluorescent Probes and Research Products*. *9th ed.*, Molecular Probes Inc., Eugene, Oregon, **2002**.
2. F. Di Virgilio, T. H. Steinberg, J. A. Swanson and S. C. Silverstein, *J. Immunol*. **1988**, *140*, 915–920.
3. M. Mitsui, A. Abe, M. Tajimi and H. Karaki, *Jpn. J. Pharmacol*. **1993**, *61*, 165–170.
4. D. Yamazaki, Y. Funato, J. Miura, S. Sato, S. Toyosawa, K. Furutani, Y. Kurachi, Y. Omori, T. Furukawa, T. Tsuda, S. Kuwabata, S. Mizukami, K. Kikuchi and H. Miki, *PLoS Genet*. **2013**, *9*, e1003983.
5. Y. Zhao, S. Araki, J. Wu, T. Teramoto, Y.-F. Chang, M. Nakano, A. S. Abdelfattah, M. Fujiwara, T. Ishihara, T. Nagai and R. E. Campbell, *Science* **2011**, *333*, 1888–1891.
6. W. Li, C. Schultz, J. Llopis and R. Y. Tsien, *Tetrahedron*, **1997**, *53*, 12017–12040.

Chapter 4

Ratiometric Imaging of Intracellular Mg^{2+} Dynamics Using a Red Fluorescent Turn-off Probe and a Green Fluorescent Turn-on Probe

Chem. Lett. **2018**, *47*, 23–26.

Introduction

Most of the reported fluorescent Mg^{2+} probes are devoid of two essential properties for Mg^{2+} sensing in living cells: (1) long maximum excitation wavelength of over 500 nm, and (2) high Mg^{2+} selectivity.[1] When the excitation is performed with short wavelength light, it results in phototoxicity to the cells and also caused autofluorescence from intracellular biomolecules,[2] leading to interference in Mg^{2+} imaging. In particular, practical ratiometric Mg^{2+} probes that can be excited with visible light have not yet been developed.[1,3,4] Additionally, selective visualization of intracellular Mg^{2+} over Ca^{2+} has been a long-standing problem because of the slow progress in the development of Mg^{2+}-selective probes.

To date, only a few Mg^{2+}-selective probes such as the KMG series[5,6] have been developed to detect the changes in $[Mg^{2+}]_i$. Among them, KMG-301, composed of a rhodamine fluorophore and a Mg^{2+}-selective β-diketone chelator has been reported as a red fluorescent Mg^{2+}-selective probe.[6,7] Although KMG-301 was spontaneously localized to the mitochondria and allowed a study of Mg^{2+} dynamics in this organelle without interference from Ca^{2+} fluctuation, its localization hinders the detection of $[Mg^{2+}]_i$ changes in the entire cell. In addition, the bidentate β-diketone chelator is incapable of discriminating between free Mg^{2+} and Mg-ATP, which is the most abundant form of Mg^{2+} in cells.[8] Buccella et al. have also developed a red fluorescent Mg^{2+} probe, MagB2, based on a styryl-BODIPY.[9] This probe can visualize changes in cytosolic $[Mg^{2+}]_i$ with red emission in living cells. However, the Mg^{2+} chelator part of MagB2 is APTRA, which also responds to high-concentrations of Ca^{2+}, similar to other red fluorescent Mg^{2+} probes such as Mag-rhod-2 and Mag-fura-red.[10] Therefore, novel red fluorescent Mg^{2+} probes that can selectively detect cytosolic Mg^{2+} concentration changes have been eagerly anticipated for a detailed analysis of intracellular Mg^{2+} dynamics.

In chapter 2, the author developed a highly selective fluorescent Mg^{2+} probe, MGQ-2, with a novel tridentate Mg^{2+}-selective chelator, 2,8-dicarboxyquinoline (DCQ). MGQ-

2, which shows turn-off response of green fluorescence upon binding to Mg^{2+}, enables the detection of changes in $[Mg^{2+}]_i$ without the formation of a complex with Mg-ATP or any response to Ca^{2+} influx. Herein, the author developed a novel red fluorescent Mg^{2+}-selective probe with a DCQ chelator and a rhodol fluorophore. The new turn-off probe demonstrated no interference from Ca^{2+} fluctuations and ratiometric Mg^{2+} imaging could be performed when it was combined with another green fluorescent turn-on Mg^{2+} probe for improved sensitivity.

Design and synthesis of a novel red fluorescent Mg^{2+}-selective probe

Rhodols have a hybrid structure of fluorescein and rhodamine, and exhibit excellent photophysical properties such as large extinction coefficients, large quantum yields, and high photostability derived from both or either of these fluorophores.[11] By changing the substituents on the nitrogen atom, the absorption and emission maxima of the rhodol fluorophores can be controlled in the range from 490 to 550 nm and from 520 to 575 nm, respectively. In particular, rhodol **1** (Figure 4-1) shows emission at longer wavelengths (λ_{abs} = 548 nm, λ_{em} = 575 nm) and pH-insensitivity over a neutral pH range (pK_a = 5.1).[11] Moreover, it is likely that the rhodol fluorophores without positive charge do not localize in the mitochondria unlike the cationic rhodamine fluorophores. Therefore, the red fluorescent Mg^{2+}-selective probe, MGQR, based on rhodol **1** skeleton was synthesized to visualize the changes in $[Mg^{2+}]_i$ throughout the cells (Figure 4-1 and Scheme 4-1).

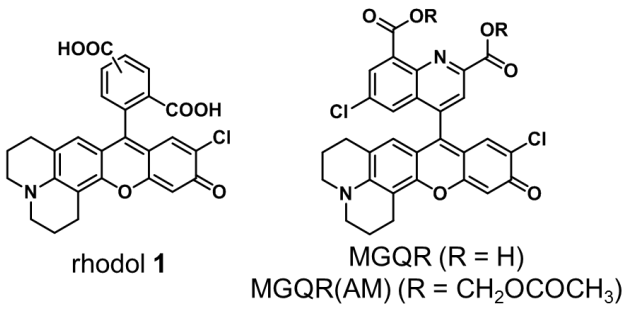

Figure 4-1. Chemical structures of the rhodol fluorophore and red fluorescent Mg^{2+} probes, MGQR and MGQR(AM).

Scheme 4-1

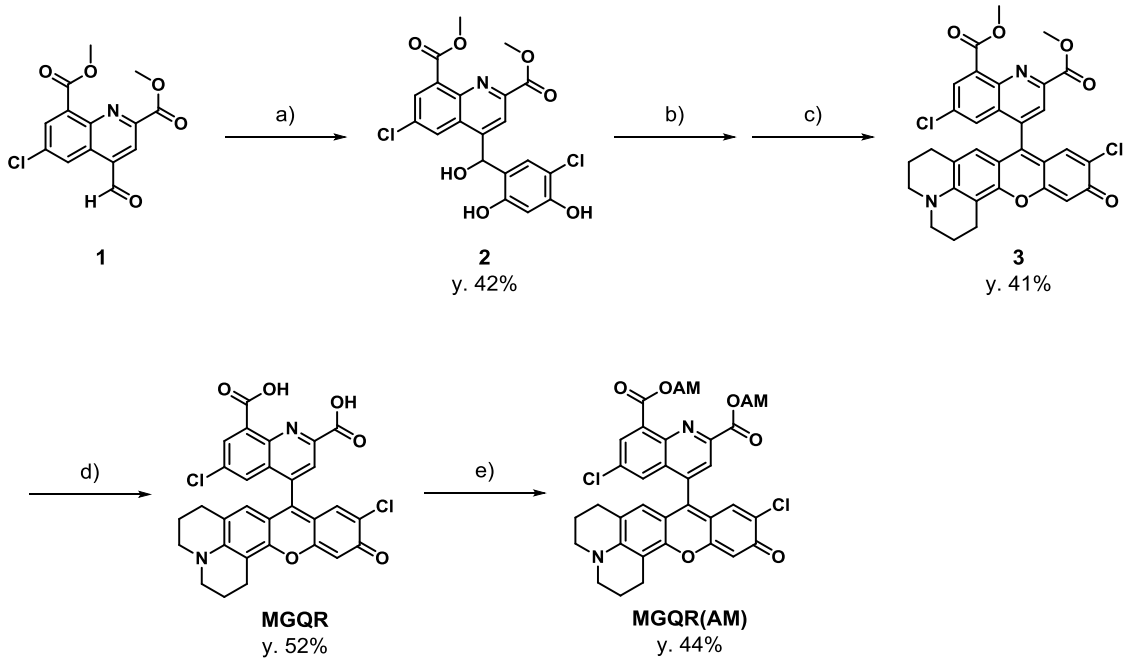

a) 4-chlororesorcinol, 8% (*v*/*v*) $MeSO_3H$, DCM/Et_2O (1:1), r.t.; b) 8-hydroxyjulolidine, *p*-TsOH·H_2O, TFA, 60 °C; c) AcOH, 60 °C; d) 2 M NaOH aq., MeOH/H_2O (3:1), r.t.; e) bromomethyl acetate, DIEA, DMF, r.t.

Optical properties of MGQR

The absorption spectrum of MGQR in the absence of Mg^{2+} showed a maximum at 561 nm. The addition of 100 mM Mg^{2+} led to a decrease in the intensity of the absorption maxima at 561 nm and a slight increase in the peak at 526 nm (Figure 4-2a). In the fluorescence emission spectra, MGQR showed a strong red fluorescence emission at 588 nm in the absence of Mg^{2+}, while the fluorescence intensity considerably decreased in the presence of Mg^{2+} (Φ_{free} = 0.29, Φ_{bound} < 0.01) (Figure 4-2a and Table 4-1). It is considered that this turn-off response corresponds to the suppression of fluorescence by the donor-excited photo-induced electron transfer (d-PeT)[12] as in the case of MGQ-2. From the emission titration curve, the dissociation constant (K_d) of MGQR for Mg^{2+} was estimated to be 0.29 mM (Figure 4-2b and Table 4-1). Since $[Mg^{2+}]_i$ typically lies in the range of 0.5–1 mM, this K_d value is suitable to visualize the intracellular Mg^{2+} dynamics. The affinity of MGQR with other biologically relevant metal ions was also assessed. The K_d in the case of Ca^{2+}, which is the most common competitor for Mg^{2+} in most of the widely used Mg^{2+} probes, was calculated to be 0.53 mM (Figure 4-2b and Table 4-1). The affinity of MGQR for Ca^{2+} was considerably weak when compared with that of the APTRA-based Mg^{2+} probes (K_d (Ca^{2+}) = 6–35 μM).[13] Considering an approximately 100 nM of Ca^{2+} in

the resting cells and a 10- to 100-fold increase of $[Ca^{2+}]_i$ in response to various stimuli,[14] it can be reasonably expected that MGQR does not respond to $[Ca^{2+}]_i$ changes in the living cells.

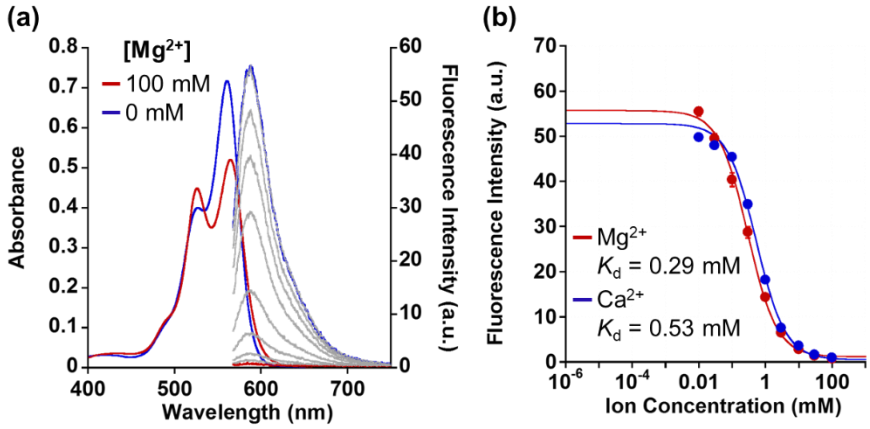

Figure 4-2. (a) Absorption and emission spectra of MGQR at different Mg^{2+} concentrations. Absorption spectra of 10 μM MGQR were measured in the presence and absence of 100 mM Mg^{2+} together with 100 mM HEPES buffer, 115 mM KCl, 20 mM NaCl, at pH 7.4 and 37 °C. Emission spectra of 1 μM MGQR were measured in a buffer solution comprised of 100 mM HEPES, 115 mM KCl, and 20 mM NaCl at pH 7.4 and 37 °C. $[Mg^{2+}]$ = 0, 0.01, 0.03, 0.1, 0.3, 1, 3, 10, 30, 100 mM. λ_{ex} = 561 nm. (b) Mg^{2+}- and Ca^{2+}-titration curves of MGQR emission at 588 nm (λ_{ex} = 561 nm). The error bars denote the standard deviation (SD) (n = 3).

Table 4-1. Spectroscopic properties of MGQR[a]

	λ_{abs}/nm	λ_{em}/nm	ε/cm^{-1} M^{-1}	Φ_{free}[b] (Φ_{bound})	K_d (Mg^{2+}) /mM	K_d (Ca^{2+}) /mM
MGQR	561	588	75,000	0.29 (<0.01)	0.29	0.53

[a] Measured at 37 °C in 100 mM HEPES buffer (pH 7.4) with 115 mM KCl and 20 mM NaCl.

[b] Relative fluorescence quantum yield determined by using rhodamine B (Φ = 0.97 in EtOH) as a standard. Φ_{free} and Φ_{bound} denote the relative fluorescent quantum yield in the absence and presence of 100 mM Mg^{2+}, respectively.

The value of K_d in the case of Zn^{2+} and MGQR was 670 nM (Figure 4-3a). However, given the stronger affinities of commercially available Mg^{2+} and Ca^{2+} probes such as Mag-fura-2 and Fura-2 for Zn^{2+} (K_d = 3–20 nM),[13] the affinity of MGQR was sufficiently weak. Although MGQR could also bind to some other metal ions such as Cu^{2+} and Co^{2+} (Figure 4-3b), the intracellular concentrations of these metal ions are at orders of magnitude lower than 1 µM.[15] Therefore, these ions are unlikely to interfere with the detection of Mg^{2+} by MGQR in typical live cell samples. In addition, the fluorescence intensity of MGQR was not affected by pH fluctuation in the neutral pH range (pH 7–8) (Figure 4-3c). The decreased fluorescence intensity of MGQR at acidic pH was attributed to the protonation of the rhodol fluorophore (Figure 4-3d and e) and d-PeT caused by protonation of the quinoline nitrogen in DCQ.

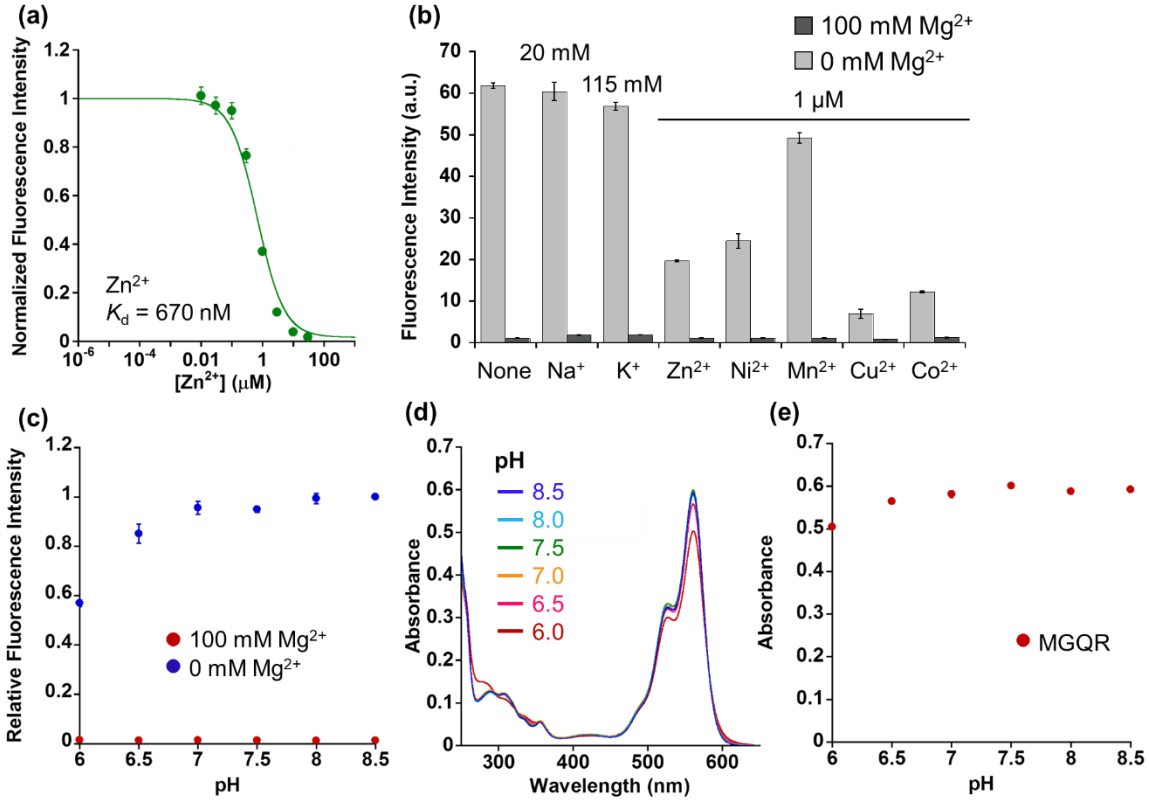

Figure 4-3. (a) Zn^{2+}-titration curve of MGQR measured from their emissions at 588 nm (100 mM HEPES buffer, 115 mM KCl, 20 mM NaCl, pH 7.4, 37 °C). [Zn^{2+}] = 0, 0.01, 0.03, 0.1, 0.3, 0.6, 1, 3, 10, 30 µM. λ_{ex} = 561 nm. (b) Metal ion selectivity of 1 µM MGQR in the presence and absence of 100 mM Mg^{2+}. [Na^+] = 20 mM and [K^+] = 115 mM (100 mM HEPES buffer, pH 7.4, 37 °C). The final concentration of Zn^{2+}, Ni^{2+}, Mn^{2+}, Cu^{2+}, or Co^{2+} was 1 µM (100 mM HEPES buffer, 115 mM KCl, 20 mM NaCl, pH 7.4, 37 °C). The error bars denote the standard deviation (SD) (n = 3). (c) Effect of the pH on the fluorescence intensity of MGQR in the pH range of 6.0–6.5 (in 100 mM MES buffer, 115 mM KCl, 20 mM NaCl) and 7.0–8.5 (in 100 mM HEPES buffer, 115 mM KCl, 20 mM NaCl), with or without 100 mM of Mg^{2+}. The error bars denote SD (n = 3). (d) Absorption spectra of 10 µM MGQR in the pH range of 6.0–6.5 (in 100 mM MES buffer, 115 mM KCl and 20 mM NaCl) and 7.0–8.5 (in 100 mM HEPES buffer, 115 mM KCl and 20 mM NaCl). (e) pH profile of the absorbance at 561 nm. The error bars denote SD (n = 3).

Responsivity of MGQ-2-Halo toward increase in $[Ca^{2+}]_i$

The author performed live-cell imaging experiments using the cell-permeable probe, MGQR(AM) (Figure 4-1 and scheme 4-1). The carboxylic acid groups of MGQR were derivatized to the acetoxymethyl (AM) ester groups to enhance its cell membrane permeability. Once inside the cells, the AM esters were hydrolyzed by endogenous esterases and converted to the Mg^{2+}-sensitive carboxylate form. HEK293 cells and HeLa cells were incubated with 1 μM MGQR(AM) and 0.01% Pluronic F-127, a surfactant polyol used for facilitating the solubilization of water-insoluble dyes, for 45 min. After washing, imaging with a spinning-disk confocal fluorescence microscope detected the fluorescence signals of MGQR throughout the cells (Figure 4-4), although it was mainly localized in the nuclei. The nuclear localization tendency was also observed in the MGQ-2-loaded cells. Compared with MGQ-2, MGQR, which has lower hydrophilicity, seemed to be more strongly localized in the nuclei. In another report, a boronate-modified probe based on a closed lactone form of the rhodol dye specifically accumulated in the nuclei while the open hydrophilic form distributed itself in the entire cell.[16] The low hydrophilicity of MGQR might be one of the reasons for the nuclear localization of MGQR. Further enhancement of its hydrophilicity is expected to improve the intracellular homogeneous distribution.

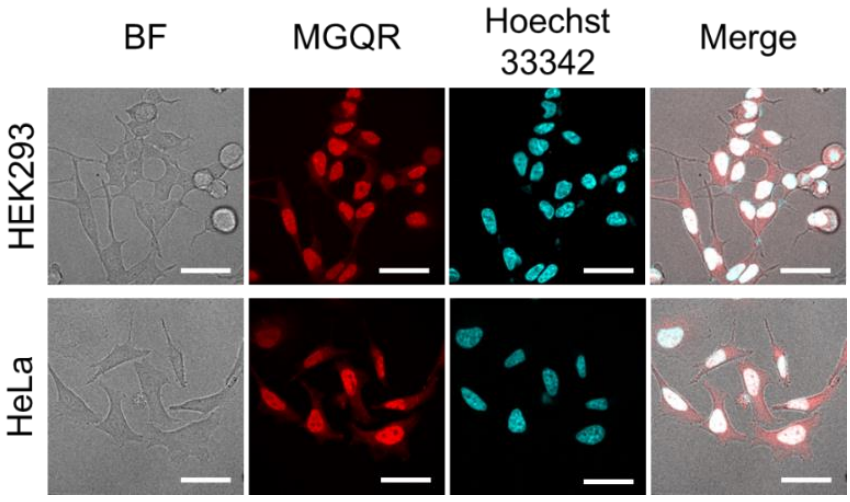

Figure 4-4. Intracellular distribution of MGQR in HEK293 or HeLa cells imaged using a confocal fluorescence microscope. HEK293 or HeLa cells were incubated with 1 μM MGQR(AM) and 200 ng/mL Hoechst 33342 for 45 min at 37 °C. Scale bar: 40 μm.

Next, the unresponsiveness of MGQR toward changes in $[Ca^{2+}]_i$ was examined in the living cells. HEK293 cells were incubated for 45 min with 1 µM MGQR(AM), 1 µM Fluo-4(AM) (a Ca^{2+}-specific small molecule-based indicator), and 0.01% Pluronic F-127. After washing the cells with Mg^{2+}- and Ca^{2+}-free HEPES-buffered Hanks' balanced salt solution (HHBSS), the buffer was replaced with Mg^{2+}-free HHBSS containing 10 mM Ca^{2+}. Then, 5 µM ionomycin, a Ca^{2+} ionophore, was added to prompt Ca^{2+} influx into the cells. For comparison, HEK293 cells expressing a genetically-encoded Ca^{2+}-specific fluorescent probe, R-GECO,[17] were prepared and the cells were loaded with 1 µM Magnesium Green(AM), a commercially available APTRA-based Mg^{2+} probe. After Ca^{2+} influx was induced by the addition of ionomycin, the fluorescence intensities of Fluo-4 and R-GECO were considerably increased, indicating an increase in $[Ca^{2+}]_i$ (Figure 4-5). A large increase in the fluorescence intensity of Magnesium Green was also observed. These results suggest that Magnesium Green responded to changes in both $[Mg^{2+}]_i$ and $[Ca^{2+}]_i$. On the other hand, MGQR did not respond to the Ca^{2+} influx. The results of these imaging studies demonstrate that the fluorescence intensity of MGQR does not experience interference as a result of intracellular Ca^{2+} fluctuations in contrast to standard APTRA-based Mg^{2+} probes.

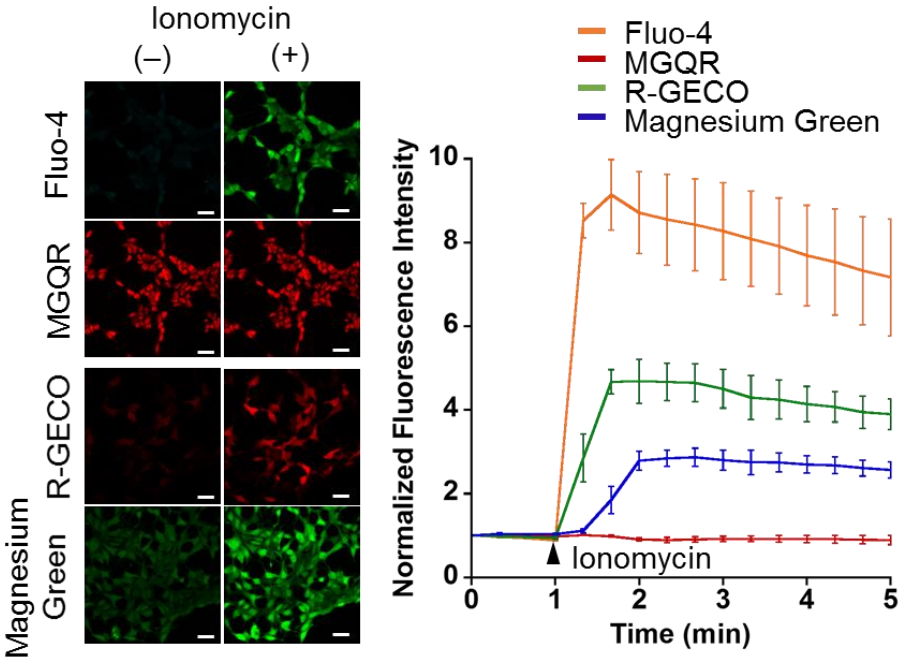

Figure 4-5. Ca^{2+} responsivity of MGQR in HEK293 cells, which were loaded with 1 µM MGQR(AM) and Fluo-4(AM) for 45 min at 37 °C. For comparison, HEK293 cells transiently expressing R-GECO were loaded with Magnesium Green(AM) for 45 min at 37 °C. After washing with Mg^{2+}- and Ca^{2+}-free HHBSS, 10 mM Ca^{2+} in Mg^{2+}-free HHBSS was added to the cells. Then, 5 µM ionomycin, a Ca^{2+} ionophore, was added at the indicated time point (arrow). Scale bar: 40 µm. The error bars denote SD (n = 5).

Ratiometric imaging of Mg^{2+} extrusion via CNNM4

Taking advantage of the red fluorescence turn-off response of MGQR, ratiometric imaging of changes in $[Mg^{2+}]_i$ was performed by combining MGQR with a green fluorescent turn-on Mg^{2+} probe, Magnesium Green (K_d (Mg^{2+}) = 1 mM). Ratiometric imaging by utilizing a ratio of green to red fluorescence from simultaneously loaded two fluorescent probes is often used to enhance sensitivity, especially in Ca^{2+} imaging using Fluo-3/Fura-red ratio.[18,19] This ratiometric imaging system requires a combination of turn-on and turn-off fluorescent probes with different excitation and/or emission wavelengths. With the exception of our DCQ-based Mg^{2+} probes, no practical turn-off Mg^{2+} probe has been developed to date. Therefore, a simultaneous loading of MGQR and Magnesium Green enables such ratiometric imaging in living cells. The emission spectra obtained for a mixture of MGQR and Magnesium Green supported the feasibility of this ratiometric Mg^{2+}-sensing system (Figure 4-6). In addition, the photostabilities of the fluorescent probes were examined because the different photobleaching populations between the two fluorophores induce changes in the ratio and hinder the precise evaluation of imaging data. The photostabilities of MGQR and Magnesium Green were measured under continuous 4.0 mW/cm^2 light irradiation at 550 and 490 nm, respectively. While the fluorescence intensity of Magnesium Green decreased slightly upon long-term irradiation, the fluorescence intensity of MGQR remained almost constant (Figure 4-7). Therefore, long-term irradiation might cause a change in the ratio of MGQR/Magnesium Green during live cell imaging.

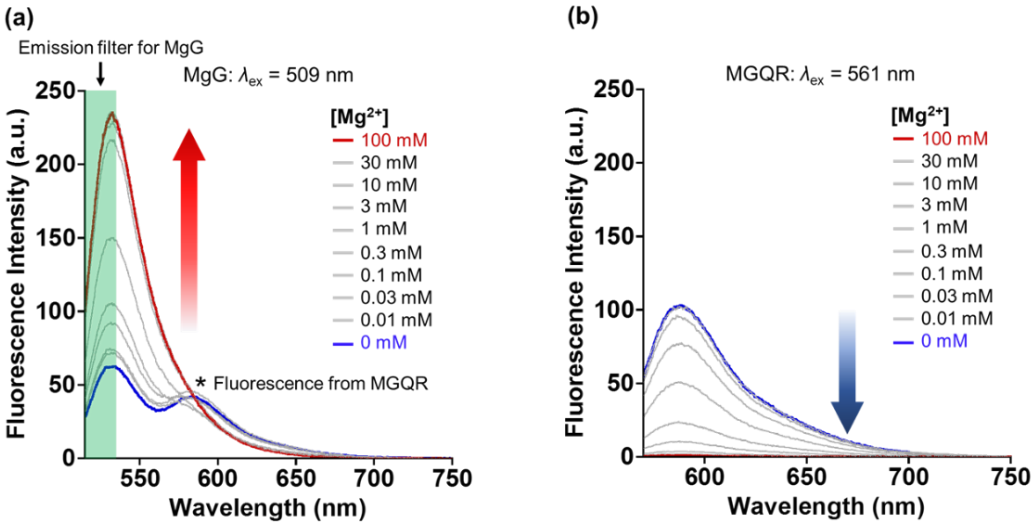

Figure 4-6. Emission spectra of a mixture of 2 μM MGQR and 1 μM Magnesium Green (MgG) excited at (a) 509 nm or (b) 561 nm in a buffer solution comprising 100 mM HEPES, 115 mM KCl, and 20 mM NaCl at pH 7.4, and containing Mg^{2+} at different concentrations at 37 °C. [Mg^{2+}] = 0, 0.01, 0.03, 0.1, 0.3, 1, 3, 10, 30 and 100 mM.

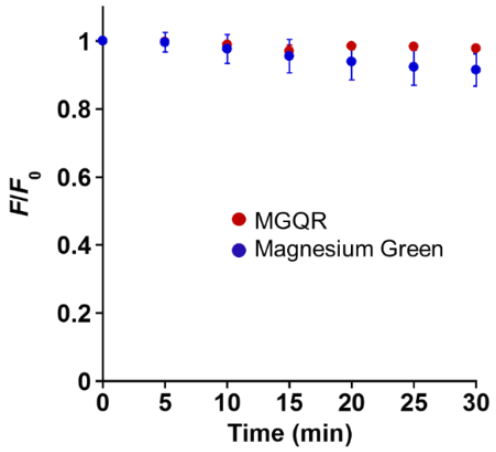

Figure 4-7. Photostabilities of MGQR and Magnesium Green under continuous light irradiation (4.0 mW/cm^2). Changes in the fluorescence intensity (F) were normalized by the initial fluorescence intensity (F_0). The error bars denote SD (n = 3).

To demonstrate the utility of the ratiometric imaging system, the change in $[Mg^{2+}]_i$ during Mg^{2+} extrusion was visualized by using a Mg^{2+} transporter, ancient conserved domain protein/cyclin M4 (CNNM4).[20] HEK293 cells transiently expressing CNNM4 were loaded with MGQR(AM) and Magnesium Green(AM) in a buffer containing 40 mM Mg^{2+}. After incubation for 45 min, the extracellular solution was exchanged with a Mg^{2+}-free buffer to artificially release the intracellular Mg^{2+} via CNNM4. The fluorescence intensity of MGQR quickly increased after Mg^{2+} extrusion, demonstrating the responsivity of MGQR to Mg^{2+} in living cells (Figures 4-8a and b). On the other hand, the fluorescence intensity of Magnesium Green decreased after the release of Mg^{2+} (Figures 4-8a and b). These inverse responses of the two Mg^{2+} probes enabled ratiometric imaging of the changes in $[Mg^{2+}]_i$ by calculating the fluorescence intensity ratio of MGQR to Magnesium Green (Figures 4-8a and c). The MGQR/Magnesium Green ratio increased by approximately 2.1 times after Mg^{2+} release through CNNM4 (Figure 4-8c and Table 4-2). This magnitude of Mg^{2+} response was considerably greater than that of either of the component probes and a widely used ratiometric Mg^{2+} probe, Mag-fura-2, which is excited by UV light (Figures 4-8a, c and Table 4-2). These results indicate that the ratiometric imaging system combining the red-fluorescent turn-off probe MGQR and a green-fluorescent turn-on Mg^{2+} probe effectively enhanced the detection sensitivity in comparison with conventional Mg^{2+} imaging systems. Because of the small range in which $[Mg^{2+}]_i$ changes occurred, this sensitivity improvement is valuable for a more precise evaluation of changes in $[Mg^{2+}]_i$. To evaluate changes in $[Mg^{2+}]_i$ more precisely, similar intracellular distribution of the two probes is important. However, MGQR tends to mainly localize in the nuclei, unlike Magnesium Green, probably due to its hydrophobicity. Further enhancement of MGQR hydrophilicity will enable homogeneous distribution in cells and confirm the validity of this imaging system. Moreover, this

imaging system has difficulty in controlling the amounts of both probes loaded in cells at a similar level (Figure 4-9). Therefore, changes in $[Mg^{2+}]_i$ in different cells should be carefully compared.

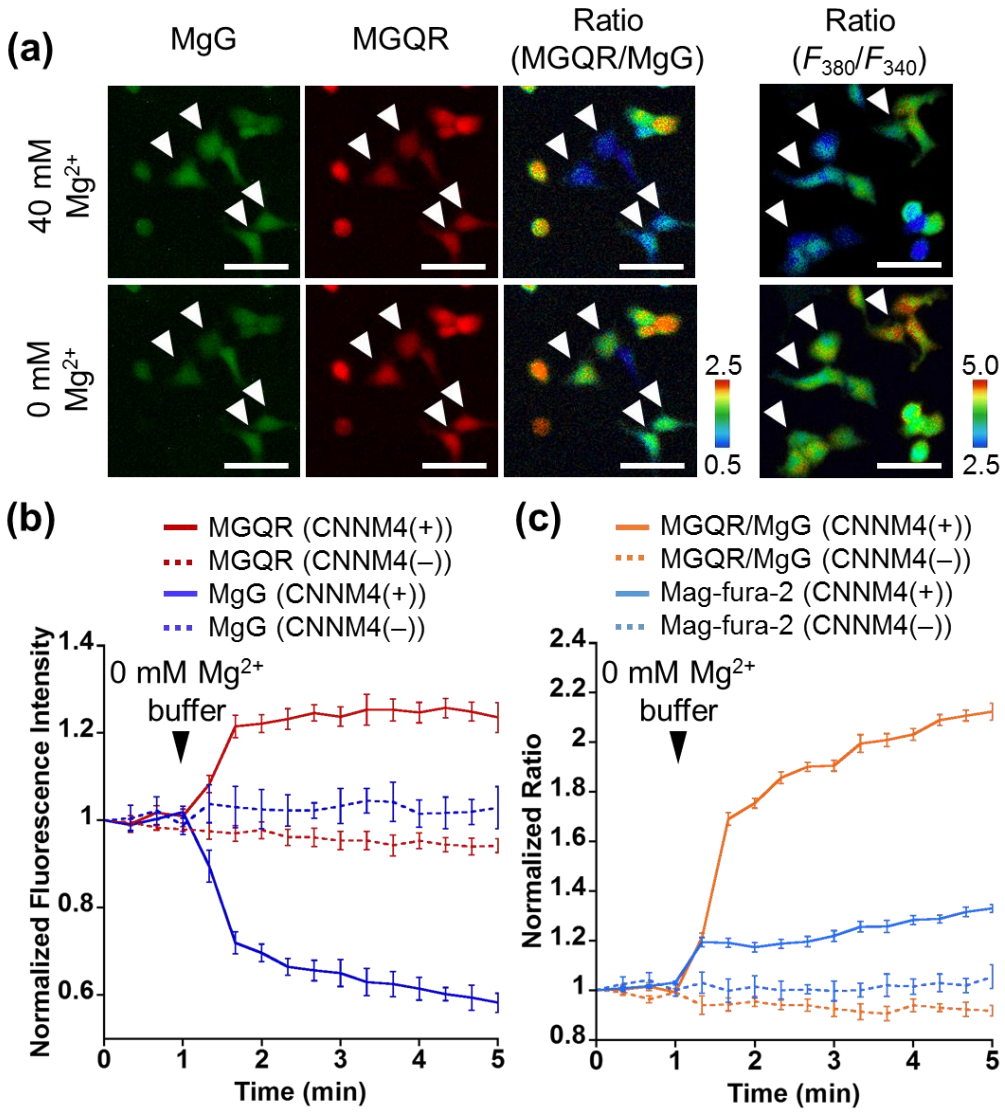

Figure 4-8. (a) Ratiometric fluorescence microscopic images of MGQR/Magnesium Green (MgG) or Mag-fura-2 in Mg^{2+} extrusion experiments. HEK293 cells transfected with CNNM4-FLAG were incubated for 45 min at 37 ºC with Mg^{2+}-loading buffer (78.1 mM NMDG-Cl, 5.4 mM KCl, 1.8 mM $CaCl_2$, 40 mM $MgCl_2$, 5.5 mM glucose, 5.5 mM HEPES-KOH, pH 7.4), including a mixture of 1 µM MGQR(AM) and 1 µM Magnesium Green(AM) or 1 µM Mag-fura-2(AM). These cells were subject to Mg^{2+} depletion 1 min after the imaging started. Scale bar: 40 µm. (b) The normalized fluorescence intensity of MGQR and MgG was presented as a line plots. The error bars denote SD (n = 4). (c) The normalized ratios of MGQR/MgG or Mag-fura-2 were presented as a line plots. The error bars denote SD (n = 4). Ratio (Mag-fura-2) = fluorescence intensity at 380 nm excitation/fluorescence intensity at 340 nm excitation.

Table 4-2. Magnitude of Mg^{2+} response in Mg^{2+} extrusion experiment (Mean ± SD)

	MGQR/MgG	MGQR	MgG	Mag-fura-2
Fold change after Mg^{2+} export	2.12 ± 0.05	1.24 ± 0.03	1.72 ± 0.07	1.33 ± 0.08

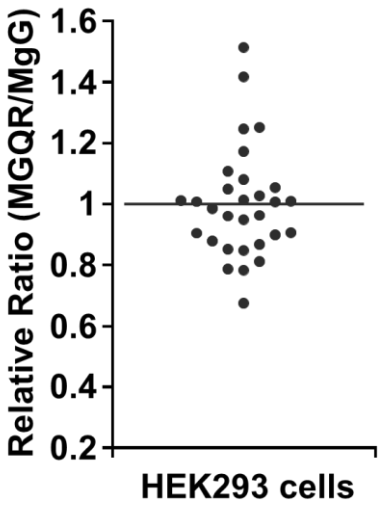

Figure 4-9. Distribution of fluorescence ratio (MGQR/Magnesium Green (MgG)) in HEK293 cells treated with 1 μM MGQR(AM) and MgG(AM) for 45 min at 37 °C. After washing the cells, the fluorescence ratio (MGQR/MgG) was calculated in individual cells (n = 30).

Experimental Methods

Materials and instruments

All chemicals used for organic synthesis were of the best grade available, supplied by Tokyo Chemical Industries, Wako Pure Chemical, or Sigma-Aldrich Chemical Co., and were used as received without further purification. Analytical thin-layer chromatography was performed on 60F254 silica plates (Merck & Co., Inc.). Silica gel column chromatography was performed using BW-300 (Fuji Silysia Chemical Ltd.). MGQR and MGQR(AM) were dissolved in DMSO (biochemical grade, Wako) before fluorescence measurements to facilitate their solubilization in aqueous solution. Magnesium Green(AM) and Mag-fura-2(AM) were purchased from Thermo Fisher Scientific. Fluo-4(AM), ionomycin, CMV-R-GECO1.0 were purchased from Dojindo, Wako, and Addgene, respectively.

HPLC analyses were performed with an Inertsil ODS-3 (4.6 mm×250 mm) column (GL Sciences Inc.) by using an HPLC system that was comprised of a pump (PU-2080, Jasco) and a detector (MD-2010, Jasco). Preparative HPLC was performed with an Inertsil ODS-3 (10.0 mm × 250 mm) column (GL Sciences Inc.) using an HPLC system that comprised a pump (PU-2087, JASCO) and a detector (UV-2075, JASCO). The buffers for MGQR(AM) were 0.1% trifluoroacetic acid (TFA) in H_2O (Buffer A) and 0.1% TFA in acetonitrile (Buffer B). NMR spectra were recorded on a Bruker Avance 500 spectrometer at 500 MHz for ^{1}H NMR and 125 MHz for ^{13}C NMR, using tetramethylsilane as an internal standard. Mass spectra were measured either on a Waters LCT-Premier XE or on a JMS-700 (JEOL) mass spectrometer.

Fluorescence spectra were measured by using a Hitachi F7000 spectrometer. The slit widths were 2.5 nm for both excitation and emission, and the photomultiplier voltage was 700 V. UV-visible absorbance spectra were measured on a Jasco aV-650 spectrophotometer. For photostability analysis, a Xe light source (MAX-303; Asahi Spectra) equipped with a band pass filter (490/5 nm for Magnesium Green and 550/5 for MGQR) was used for irradiation.

Fluorescence microscopy images were recorded using a confocal fluorescence microscopy imaging system including a fluorescence microscope (IX71, Olympus), an EMCCD (iXon3, Andor Technology), a confocal scanner unit (CSU-X1, Yokogawa Electric Corporation), and a multispectral LED light source (Spectra X light engine, Lumencor). The filter sets were BP377 ± 25/DM405/BA447 ± 30 (for Hoechst 33342), BP488 ± 3/DM488/BA520 ± 17.5 (for Magnesium Green and Fluo-4) and BP560 ± 13/DM561/BA624 ± 20 (for MGQR and R-GECO1.0). The entire system was controlled by using the MetaMorph 7.6 software (Molecular Devices). For Mg^{2+} extrusion

experiments, epifluorescence microscopy images were captured by using a microscope (IX71, Olympus) equipped with a CMOS camera (ORCA-Flash 4.0, Hamamatsu Photonics), and a mercury lamp (USH-1030L, Olympus). The fluorescence microscopy images were measured after every 20 s (MGQR: excitation at 556 ± 10 nm and emission at 617 ± 36.5 nm; Magnesium Green: excitation at 470 ± 11 nm and emission at 514 ± 15 nm; Mag-fura-2: excitation at 340 ± 10/380 ± 10 nm, and emission at 525 ± 20 nm).

Fluorometric analysis

The relative fluorescence quantum yield of MGQR was obtained by comparing the area under the emission spectrum. The following equation was used to calculate the quantum yield:

$$\Phi_x = \Phi_{st} (I_x/I_{st})(A_{st}/A_x)(n_x^2/n_{st}^2)$$

, where Φ_{st} is the reported quantum yield of the standard, I is the integrated emission spectrum, A is the absorbance at the excitation wavelength, and n is the refractive index of the solvent. The subscripts x and st denote the sample and the standard, respectively. Rhodamine B (Φ = 0.97 when excited at 535 nm in EtOH) was used as the standard.

The photostabilities of MGQR and Magnesium Green (1 μM, 2 mL) were examined in 100 mM HEPES buffer (pH 7.4) with 115 mM KCl and 20 mM NaCl at 25 °C under continuous light irradiation through a band pass filter (490 ± 2.5 nm for Magnesium Green, 550 ± 2.5 nm for MGQR, 4.0 mW/cm^2) using a Xe light source. The fluorescence intensities of MGQR (λ_{ex} = 561 nm, λ_{em} = 588 nm) and Magnesium Green (λ_{ex} = 509 nm, λ_{em} = 534 nm) were measured after every 5 min for 30 min.

Determination of dissociation constants

The apparent dissociation constant (K_d) of MGQR for the metal ions in 100 mM HEPES buffer (pH 7.4) containing 115 mM KCl and 20 mM NaCl was calculated using the following equation,

$$[M^{n+}] = K_d (F - F_{min})/(F_{max} - F)$$

, where F is the fluorescence intensity at each metal ion concentration, F_{min} is the fluorescence intensity before addition of the metal ions, and F_{max} is the fluorescence intensity at the saturation point.

Metal ion selectivity study

Metal ion selectivity was measured by adding either $MgCl_2$, NaCl, KCl, $ZnCl_2$, $CoCl_2$, $MnCl_2$, $NiCl_2$ or $CuCl_2$ to 1 μM MGQR solution. The fluorescence intensity of MGQR with 20 mM Na^+ or 115 mM K^+ was measured in 100 mM HEPES buffer (pH

7.4). The fluorescence intensity with 1 μM of Zn^{2+}, Co^{2+}, Mn^{2+}, Ni^{2+}, or Cu^{2+} was measured in 100 mM HEPES buffer (pH 7.4) with 115 mM KCl and 20 mM NaCl.

Cell culture

HEK293 and HeLa cells were cultured in high-glucose Dulbecco's modified Eagle medium (DMEM) plus Gluta Max-I supplemented with 10% fetal bovine serum (FBS), 100 U/mL penicillin, and 100 μg/mL streptomycin. The cells were incubated at 37 °C in a humidified atmosphere with 5% CO_2. A subculture was performed every 2–3 days from the subconfluent (<80%) cultures using a trypsin-ethylenediamine tetraacetic acid solution. Transfection of plasmids was carried out in a glass-bottomed dish using Lipofectamine 3000 according to the standard protocol.

Live-cell fluorescence imaging of MGQR(AM)

HEK293 or HeLa cells maintained in 10% FBS in DMEM at 37 °C in 5% CO_2 were washed three times with Hanks' balanced salt solution (HBSS) and incubated in FBS-free DMEM containing 1 μM MGQR(AM) and 0.01% Pluronic F-127 for 45 min in a CO_2 incubator. After washing with HBSS, the medium was replaced with DMEM and the fluorescence images were captured using a confocal fluorescence microscope.

Responsivity of MGQR toward increase in $[Ca^{2+}]_i$

HEK293 cells were incubated in FBS-free DMEM containing 1 μM MGQR(AM), 1 μM Fluo-4(AM), and 0.01% Pluronic F-127 for 45 min at 37 °C. For the control experiment using Magnesium Green, HEK293 cells were transfected with pCMV-R-GECO1.0 using Lipofectamine 3000 and the cells were incubated at 37 °C for 24 h. The cells were rinsed twice with Mg^{2+}- and Ca^{2+}-free HEPES-buffered HBSS (HHBSS), and 10 mM Ca^{2+} in Mg^{2+}-free HHBSS was added to the cells. Subsequently, time lapse images were taken with 5 μM of ionomycin added after 1 min. The fluorescence images were captured after every 20 s using a confocal fluorescence microscope.

Ratiometric imaging of Mg^{2+} extrusion

HEK293 cells were transfected with pCMV-CNNM4-FLAG using Lipofectamine 3000, and the cells were incubated at 37 °C for 24 h. Then, the cells were incubated with a Mg^{2+}-loading buffer (78.1 mM *N*-methyl-$_D$-glucamine hydrochloride (NMDG-Cl), 5.4 mM KCl, 1.8 mM $CaCl_2$, 40 mM $MgCl_2$, 5.5 mM glucose, and 5.5 mM HEPES-KOH at pH 7.4), including a mixture of 1 μM MGQR(AM), 1 μM Magnesium Green(AM), and 0.01% Pluronic F-127 or 1 μM Mag-fura-2(AM) for 45 min at 37 °C. The cells were

rinsed once with the loading buffer and the fluorescence images were captured every 20 s using an epifluorescence microscope. The buffer was then replaced with a Mg^{2+}-free buffer (138.1 mM NaCl, 5.4 mM KCl, 1.8 mM $CaCl_2$, 5.5 mM glucose, and 5.5 mM HEPES-KOH at pH 7.4).

Chemical synthesis

Synthesis of compound 2

Compound **1** (140 mg, 0.455 mmol) and 4-chlororesorcinol (65.8 mg, 0.455 mmol) were added to a flame-dried three-necked flask under N_2. A mixture of DCM/Et_2O (1:1) (12 mL) was added to the flask, followed by the dropwise addition of $MeSO_3H$ (960 µL) at room temperature. The reaction mixture was stirred for 3 h and subsequently, diluted with Et_2O, poured into saturated aqueous $NaHCO_3$, and acidified with 2 M HCl aq. to pH 5–6. The solution was extracted with ethyl acetate, and the combined organic extracts were dried with Na_2SO_4 and evaporated under reduced pressure. The residue was purified by flash column chromatography on silica gel (DCM/MeOH). Compound **2** (85.2 mg, 42%) was obtained as a colorless solid.

^{1}H NMR (500 MHz, Acetone-d_6) δ 8.55 (s, 1H), 8.45 (d, J = 2.5 Hz, 1H), 7.93 (d, J = 2.5 Hz, 1H), 7.08 (s, 1H), 6.81 (s, 1H), 6.67 (s, 1H), 4.00 (s, 3H), 3.99 (s, 3H); ^{13}C NMR (125 MHz, Acetone-d_6) δ 166.7, 166.3, 153.6, 153.4, 151.9, 149.0, 143.0, 136.6, 132.8, 129.3, 129.0, 127.7, 125.5, 121.9, 119.1, 111.2, 103.8, 64.88, 52.30, 52.12; HRMS (FAB^+): Calcd for $[M+H]^+$ 452.0226, found 452.0297.

Synthesis of compound 3

Compound **2** (78.3 mg, 0.173 mmol), 8-hydroxyjulolidine (49.2 mg, 0.260 mmol), and *p*-TsOH·H_2O (3.29 mg, 17.3 µmol) were dissolved in TFA (2 mL) and stirred at 60 °C for 6 h. After confirming the completion of the reaction, AcOH (2 mL) was added to the solution. The solution was then stirred for 4 h. After cooling to room temperature, the solution was evaporated under reduced pressure and purified by flash column chromatography on silica gel (DCM/MeOH). Compound **3** (43.3 mg, 41%) was obtained as a purple solid.

^{1}H NMR (500 MHz, $CDCl_3$) δ 8.19 (s, 1H), 8.10 (d, J = 2.5 Hz, 1H), 7.55 (d, J = 2.5 Hz, 1H), 6.70 (s, 1H), 6.66 (s, 1H), 6.12 (s, 1H), 4.15 (s, 3H), 4.09 (s, 3H), 3.42–3.35 (m, 4H), 3.04–2.98 (m, 2H), 2.52–2.46 (m, 2H), 2.08–1.88 (m, 4H); ^{13}C NMR (125 MHz, $CDCl_3$) δ 176.8, 166.1, 165.0, 157.4, 150.5, 149.1, 148.5, 143.5, 143.4, 141.4, 135.4, 135.0, 133.1, 132.9, 128.5, 126.8, 126.3, 124.8, 123.0, 121.3, 113.6, 109.9, 105.8, 105.4, 53.49, 53.23, 50.49, 50.09, 27.40, 20.76, 20.05, 19.98; HRMS (FAB^+): Calcd for $[M+H]^+$ 603.1011,

found 603.1097.

Synthesis of MGQR

Compound **3** (40.0 mg, 66.2 μmol) was dissolved in 16 mL of MeOH/H_2O (3:1) and 1 mL of 2 M NaOH aqueous solution was added dropwise at 0 °C. The reaction mixture was then warmed to room temperature. After stirring for 17 h, the solution was acidified with 2 M HCl aq. and then evaporated under reduced pressure. The residue was purified by reversed-phase column chromatography (50 mM trimethylamine acetate/MeCN). After lyophilization, MGQR·3.3Et_3N·0.4AcOH (32.0 mg, 52%) was obtained as a purple powder.

^{1}H NMR (500 MHz, MeOD) δ 8.43 (s, 1H), 8.25 (s, 1H), 7.68 (s, 1H), 6.92 (s, 1H), 6.68 (s, 1H), 6.52 (s, 1H), 3.53–3.44 (m, 4H), 3.23–3.19 (q, *J* = 7.0 Hz, 19H), 3.11–2.98 (m, 2H), 2.60–2.50 (m, 2H), 2.07–2.03 (m, 2H), 1.95 (s, 1.3H), 1.88–1.85 (m, 2H), 1.34–1.31 (t, *J* = 7.0 Hz, 30H) ; ^{13}C NMR (125 MHz, MeOD) δ 175.8, 168.7, 157.7, 154.2, 151.6, 151.0, 147.1, 142.6, 141.6, 135.3, 134.4, 129.8, 128.0, 127.0, 125.3, 123.9, 111.9, 111.5, 105.4, 104.0, 50.47, 50.02, 46.36, 26.87, 20.25, 19.50, 19.40, 7.80; HRMS (FAB^+): Calcd for $[M+H]^+$ 575.0698, found 575.0793.

Synthesis of MGQR(AM)

MGQR (17.8 mg, 29.4 μmol) and dry DMF (3 mL) were added to a flame-dried three-necked flask under N_2, followed by the addition of *N*,*N*-diisopropylethylamine (DIEA) (25.3 μL, 147 μmol) and bromomethyl acetate (14.4 μL, 147 μmol) at room temperature. After stirring for 5 h, the solvent was removed under reduced pressure. Ethyl acetate was added to the residue and then it was washed with water. The organic layer was washed with brine, dried with Na_2SO_4 and evaporated. The residue was purified by HPLC under the following conditions: A/B = 40/60 (0 min), 60/40 (30 min) (solvent A: 0.1% TFA in MeCN; solvent B: 0.1% TFA in H_2O). After lyophilization, MGQR(AM) (9.4 mg, 44%) was obtained as a purple solid.

^{1}H NMR (500 MHz, CD_3Cl) δ 8.19 (s, 1H), 8.12 (s, 1H), 7.44 (s, 1H), 7.39 (s, 1H), 6.83 (s, 1H), 6.37 (s, 1H), 6.16 (s, 2H), 6.05 (s, 2H), 3.70–3.54 (m, 4H), 3.24–3.02 (m, 2H), 2.71–2.57 (m, 2H), 2.13–1.98 (m, 10H); ^{13}C NMR (125 MHz, CD_3Cl) δ 169.9, 169.6, 167.2, 164.4, 162.7, 154.9, 153.6, 152.1, 147.6, 146.5, 143.6, 139.8, 136.2, 134.2, 133.5, 128.1, 127.5, 127.3, 126.8, 125.7, 125.5, 123.0, 115.1, 112.8, 106.5, 104.4, 80.49, 80.27, 51.85, 51.40, 27.30, 20.79, 20.69, 19.98, 19.62, 19.25; HRMS (FAB^+): Calcd for $[M+Na]^+$ 741.1121, found 741.1008.

References

1. V. Trapani, G. Farruggia, C. Marraccini, S. Iotti, A. Cittadini and F. I. Wolf, *Analyst* **2010**, *135*, 1855–1866.
2. M. Monici, *Biotechnol. Annu. Rev.* **2005**, *11*, 227–256.
3. M. S. Afzal, J.-P. Pitteloud and D. Buccella, *Chem. Commun*. **2014**, *50*, 11358–11361.
4. T. Shoda, K. Kikuchi, H. Kojima, Y. Urano, H. Komatsu, K. Suzuki and T. Nagano, *Analyst* **2003**, *128*, 719–723.
5. H. Komatsu, N. Iwasawa, D. Citterio, Y. Suzuki, T. Kubota, K. Tokuno, Y. Kitamura, K. Oka and K. Suzuki, *J. Am. Chem. Soc*. **2004**, *126*, 16353–16360.
6. Y. Shindo, T. Fujii, H. Komatsu, D. Citterio, K. Hotta, K. Suzuki and K. Oka, *PLoS One* **2011**, *6*, e23684.
7. P. A. Otten, R. E. London and L. A. Levy, *Bioconjugate Chem*. **2001**, *12*, 203–212.
8. S. C. Schwartz, B. Pinto-Pacheco, J.-P. Pitteloud and D. Buccella, *Inorg. Chem*. **2014**, *53*, 3204–3209.
9. Q. Lin, J. J. Gruskos and D. Buccella, *Org. Biomol. Chem*. **2016**, *14*, 11381–11388.
10. G. R. Monteith, *Immunol. Cell Biol*. **2000**, *78*, 403–407.
11. J. E. Whitaker, R. P. Haugland, D. Ryan, P. C. Hewitt, R. P. Haugland and F. G. Prendergast, *Anal. Biochem*. **1992**, *207*, 267–279.
12. T. Ueno, Y. Urano, K. Setsukinai, H. Takakusa, H. Kojima, K. Kikuchi, K. Ohkubo, S. Fukuzumi and T. Nagano, *J. Am. Chem. Soc*. **2004**, *126*, 14079–14085.
13. R. P. Haugland, *Handbook of Fluorescent Probes and Research Products. 9th ed.*, Molecular Probes Inc., Eugene, Oregon, **2002**.
14. D. E. Clapham, *Cell* **2007**, *131*, 1047–1058.
15. K. P. Carter, A. M. Young and A. E. Palmer, *Chem. Rev*. **2014**, *114*, 4564–4601.
16. B. C. Dickinson, Y. Tang, Z. Chang and C. J. Chang, *Chem. Biol*. **2011**, *18*, 943–948.
17. Y. Zhao, S. Araki, J. Wu, T. Teramoto, Y.-F. Chang, M. Nakano, A. S. Abdelfattah, M. Fujiwara, T. Ishihara, T. Nagai and R. E. Campbell, *Science* **2011**, *333*, 1888–1891.
18. F.-Y. Li, B. Chaigne-Delalande, C. Kanellopoulou, J. C. Davis, H. F. Matthews, D. C. Douek, J. I. Cohen, G. Uzel, H. C. Su and M. J. Lenardo, *Nature* **2011**, *475*, 471–476.
19. E. J. Novak, P. S. Rabinovitch, *Cytometry* **1994**, *17*, 135–141.
20. D. Yamazaki, Y. Funato, J. Miura, S. Sato, S. Toyosawa, K. Furutani, Y. Kurachi, Y. Omori, T. Furukawa, T. Tsuda, S. Kuwabata, S. Mizukami, K. Kikuchi and H. Miki, *PLoS Genet.* **2013**, *9*, e1003983.

Conclusions and Perspective

Mg^{2+} contributes to various physiological processes in living cells. However, detailed Mg^{2+} dynamics not only in cytosol but also in organelles still remain unclear due to non-selective organelle targetability, rapid extracellular leakage, low Mg^{2+} selectivity, and excitation with short wavelength of conventional Mg^{2+} probes. Therefore, to elucidate unknown physiological Mg^{2+} dynamics, the author developed novel fluorescent Mg^{2+} probes which enabled various applications beyond the limits of conventional Mg^{2+} probes, such as subcellular targeting, long-term imaging, selective detection of Mg^{2+}, and sensitive ratiometric imaging with visible excitation light.

In chapter 1, the author developed a novel Mg^{2+} probe, MGH, which covalently binds to HaloTag protein expressed in various cellular compartments. The conjugation of MGH to HaloTag dramatically suppressed extracellular leakage of MGH, and the Mg^{2+} sensing ability of MGH was retained for 24 h. These noteworthy properties were successfully applied to long-term visualization of intracellular Mg^{2+} dynamics during apoptosis. The results demonstrated an increase in Mg^{2+} concentration after apoptotic cell shrinkage. Subsequent experiments utilizing an FRET-based ATP sensor showed that dissociation of Mg^{2+} from ATP in apoptotic cells was the source of increase of Mg^{2+} concentration. Thus, long-term imaging with a HaloTag-coupled Mg^{2+} probe provided precise information regarding intracellular Mg^{2+} dynamics during apoptosis. This study includes the molecular design of a cell-functional probe that involves a synthetic organic molecule and a genetically encoded protein. In addition, the findings in this study should contribute to understanding of Mg^{2+}-related biology, which includes very wide areas in biology and medicine, and thus the results strongly suggest that this new methodology will be a robust tool for studying Mg^{2+} dynamics in living systems and diseases.

In chapter 2, the author developed highly specific fluorescent Mg^{2+} probes, MGQ-1 and MGQ-2, with a novel tridentate chelator, DCQ. MGQ-2, which is pH-insensitive over a neutral pH range, showed a suitable dissociation constant for detecting $[Mg^{2+}]_i$ changes and very weak affinity for Ca^{2+}. The rigid tridentate ligand had several distinct advantages such as high selectivity towards Mg^{2+} over Ca^{2+} and discriminative sensing of free Mg^{2+}. These remarkable properties enabled MGQ-2 to selectively visualize $[Mg^{2+}]_i$ change in living cells without fluorescence response to Ca^{2+} influx from a 10 mM Ca^{2+} medium. MGQ probes are the first quenching type Mg^{2+}-selective probe to be based on the d-PeT mechanism upon metal ion coordination. The turn-off property of the MGQ series may be useful for visualizing Mg^{2+} export via the Na^+/Mg^{2+} exchangers and Mg^{2+} transporters elicited by cyclic AMP-dependent or -independent processes. Considering the long-

standing under-development of Mg^{2+}-selective probes, our new probes will undoubtedly trigger both the development of more practical Mg^{2+} probes and the elucidation of intracellular Mg^{2+} dynamics.

In chapter 3, the author developed a Mg^{2+}-selective probe with HaloTag ligand, MGQ-2-Halo. Conjugation of MGQ-2-Halo to HaloTag suppressed extracellular leakage of the probe and enabled long-term imaging of Mg^{2+} over 24 h. Moreover, MGQ-2-Halo could be precisely localized to specific sites in living cells. In particular, in some organelles such as the ER, mitochondria, and Golgi apparatus, with high concentrations of Ca^{2+} (hundreds μM levels), Mg^{2+} dynamics still remain unsolved. MGQ-2-Halo and its more Mg^{2+}-selective and pH-insensitive derivatives will be powerful chemical tools to clarify unknown physiological Mg^{2+} roles, such as mechanisms of Mg^{2+} influx through Mg^{2+} channels and Mg^{2+}-related diseases, hidden behind the high-concentration of Ca^{2+} in these organelles.

In chapter 4, the author developed a red fluorescent turn-off Mg^{2+} probe, MGQR, based on a Mg^{2+}-selective DCQ chelator and a rhodol fluorophore. MGQR showed very low affinity for Ca^{2+} and did not respond to intracellular Ca^{2+} fluctuations introduced by ionomycin. MGQR showed a large decrease in the fluorescence intensity in response to Mg^{2+} with a suitable dissociation constant for detecting $[Mg^{2+}]_i$ changes. This fluorescence quenching response of MGQR upon binding to Mg^{2+} was applied to the ratiometric imaging of Mg^{2+} dynamics with a green fluorescent turn-on Mg^{2+} probe. This ratiometric imaging system enabled a highly sensitive detection of changes in the $[Mg^{2+}]_i$ compared to other common ratiometric Mg^{2+} imaging systems. Considering the lack of practical ratiometric Mg^{2+} probes excited by visible light and the small range of $[Mg^{2+}]_i$ fluctuations in the living cells, this ratiometric Mg^{2+} sensing system is very useful for visualizing small changes in $[Mg^{2+}]_i$ with low phototoxicity. Furthermore, multicolor imaging of Mg^{2+} and another biomolecule can reveal unknown correlations between these molecules when MGQR is used together with another probe that shows fluorescence at green or shorter wavelengths. Thus, the novel Mg^{2+} probe MGQR is expected to lead to various applications beyond the limits of existing Mg^{2+} probes and encourage studies to elucidate unknown biological roles of Mg^{2+}.

List of Publications

1. Highly Selective Tridentate Fluorescent Probes for Visualizing Intracellular Mg^{2+} Dynamics without Interference from Ca^{2+} Fluctuation
   Y. Matsui, K. K. Sadhu, S. Mizukami, and K. Kikuchi
   Chem. Commun. **2017**, *53*, 10644–10647.

2. Visualization of Long-term Mg^{2+} Dynamics in Apoptotic Cells with a Novel Targetable Fluorescent Probe
   Y. Matsui, Y. Funato, H. Imamura, H. Miki, S. Mizukami, and K. Kikuchi
   Chem. Sci. **2017**, *8*, 8255–8264.

3. Ratiometric Imaging of Intracellular Mg^{2+} Dynamics Using a Red Fluorescent Turn-off Probe and a Green Fluorescent Turn-on Probe
   Y. Matsui, S. Mizukami, and K. Kikuchi
   Chem. Lett. **2018**, *47*, 23–26.

4. HaloTag-conjugated Mg^{2+}-selective Fluorescent Probe for Visualizing Mg^{2+} Dynamics in Specific Organelles over a Long Time Period
   Y. Matsui, S. Mizukami, and K. Kikuchi
   In preparation

Presentation at International Conference

1. **Y. Matsui**, S. Mizukami, Y. Funato, H. Miki, K. Kikuchi, "Development of Fluorescent Probe for Visualizing Local Mg^{2+} Dynamics in Living Cells" Pacifichem 2015, HLTH 656, Honolulu, Hawaii, USA, December 2015.

Award

1. *Poster Award*, 10th Symposium on Biorelevant Chemistry, CSJ, September 2016.

Acknowledgments

The author is most grateful to Professor Kazuya Kikuchi for his continuous guidance, support, and encouragement throughout this study. The author expresses his sincere thanks to Professor Shin Mizukami for his valuable guidance and discussion. The author also expresses his cordial thanks to Dr. Yuichiro Hori, Dr. Masafumi Minoshima, Dr. Toshiyuki Kowada, and Dr. Yuko Kamikawa for their kind help and valuable discussions.

The author is deeply grateful to Professor Hiroaki Miki and Dr. Yosuke Funato at Research Institute for Microbial Diseases in Osaka University for the helpful discussions and for providing the *CNNM4* gene. The author would like to thank Dr. Hiromi Imamura at Graduate School of Biostudies in Kyoto University for valuable advice regarding apoptosis imaging experiments and providing the *ATeam* gene.

The author acknowledges all of the members of the Kikuchi laboratory and Mizukami laboratory for their kind help, teaching, and friendship.

The author acknowledges financial support from the Interdisciplinary Program for Biomedical Sciences (IPBS). Finally, the author appreciates the tremendous support and continuous encouragement from his family and friends.

Osaka, Japan
January, 2018

Yusuke Matsui

Division of Advanced Science and Biotechnology
Department of Materials and Life Science
Graduate School of Engineering, Osaka University